Investigation of Endogenous Chemical Exchange Saturation Transfer Effects with Magnetic Resonance Imaging in Various Animal Models of Neurological Disorders.

Marilena Rega

Department of Brain Repair and Rehabilitation

UCL, Institute of Neurology

Ph.D Thesis

Submitted for the Degree of Doctor of Philosophy

University College London

September 2014

I, Marilena Rega confirm that the work presented in this thesis is my own. Where information has been derived from other sources, I confirm that this has been indicated in the thesis.

Abstract

Chemical Exchange Saturation Transfer (CEST), is an emerging Magnetic Resonance Imaging (MRI) technique. CEST indirectly measures exchangeable protons contained in either endogenous or exogenous compounds by measuring the water signal reduction due to magnetisation exchange between these compounds and the surrounding water. CEST offers sensitivity enhancement compared to any method which directly measures these compounds. The complexity of the CEST signal in-vivo limits direct quantitative interpretation. However, the technique is inherently sensitive to a range of physiological parameters, such as temperature, pH and metabolite concentration.

In order to investigate the relative importance of these different contributing factors, the work described in this thesis used the Bloch-McConnell equation system to model the CEST effect, for CEST sequence optimisation and data interpretation. Bovine Serum Albumin (BSA) phantoms were scanned with a CEST sequence and the results were compared to standard contrast methods (T_1, T_2). The CEST effects were correlated with changes in environmental pH, temperature and metabolite concentration.

Next, a spectroscopic CEST sequence was implemented for spinal cord CEST and two models of neurodegenerative diseases were investigated. First, a model of Amyotrophic Lateral Sclerosis (ALS), revealed no changes in the CEST signal over the time course of the disease; the finding matched post-mortem soluble protein concentration analysis. Second, a model of Spinal and Bulbar Muscular Atrophy (SBMA), revealed no changes in the CEST signal of affected mice scanned at 10 and 12 months of age. However, changes in the CEST signal were observed in control mice and this again agreed with post-mortem protein concentration analysis.

Finally, the potential for CEST to measure regional pH changes in a piglet model of Hypoxic Ischemia (HI) was investigated. CEST data were compared and found to agree with ^{31}P MRS, measuring intracellular pH (pH_i) and ^{1}H MRS, measuring cerebral lactate levels.

Table of Contents

List of Figures

List of Tables

List of Abbreviations

The following list summarizes all the abbreviations and acronyms used throughout the thesis given in alphabetic order.

Acknowledgments

For the past four years I have been lucky to work close to and learn a lot from so many amazing people. First I would like to thank my primary supervisor Prof Xavier Golay, for being extremely supportive, always available for advice and when I could not see this project working always managing to uplift my enthusiasm on the Monday meetings! I would like to thank my secondary supervisor Dr David Thomas, for always being there when I needed help and for sharing his knowledge and skills with me. Also, Dr Simon Walker-Samuel, my third supervisor, whose work inspired and motivated further my research.

This work would not have been possible the way it turned out to be, if it was not for the support and input from our research collaborators. Therefore a special thank you to Prof Linda Greensmith and her group. Especially Mr James Dick for taking care and providing me with animals even with no notice at all, Dr Phillip Smethurst for his post-mortem work on the ALS study, Miss Anna Gray, for day in and day out animal treatment during our SBMA study, for conducting the post-mortem work and for the supportive tea breaks!

In addition I would like to thank Prof Nicola Robertson and her group. Especially I thank Dr Alan Bainbridge for the time he spent in teaching me how to use AMARES, his knowledge on MRI, for acquiring data and providing me with analysed spectroscopy. Dr David Price for acquiring data and Miss Magdalena Sokolska also for acquiring data but most importantly for the many 'duck talks' throughout this time! Chapter 6 would have not been possible without the surgical skills and animal intensive care provided by Dr Kevin Broad, Dr Go Kawano, Dr Igor Fiernes and Dr Mojgan Ezatti.

I would also like to thank Dr Mohamed Tachrount for sharing his MRI knowledge at any time, Dr Fatima Ali Nashrallah for the very useful tips in animal handling and great inspiration all the way from Singapore and Miss Maria Spyrou for reading my work on the very last moment.

Finally I am gratefully to Patxi, whom I cannot probably thank enough for his endless patience and support, for (literally) always being there throughout this process, for reading and criticizing my work, for challenging me to always be a better scientist, for making every day an adventure!

Chapter 1. Introduction

1.1. A brief overview on Chemical Exchange Saturation Transfer applications

Proton exchange was first introduced by Wolff and Balaban in 1989 [1] as an MR imaging technique capable to study chemical interactions between labile protons[1] and water through chemical exchange. With those experiments as well as the work published a few years later, in 1998 by Guivel-Scharen et al [2], the exchange principle was validated as a method providing indirect information on labile protons, but with a strong dependency on the concentration and pH of the labile protons. Eventually in 2000, the technique was named Chemical Exchange Saturation Transfer (CEST) by Ward et al [3]. Since then, there have been numerous papers published on different applications. Generally CEST is classified into three categories: diamagnetic CEST (diaCEST), paramagnetic CEST (paraCEST) and hyperpolarized CEST (hyperCEST), due to the different exchangeable sites (also referred to as CEST agents) involved in each category. This section intends to provide a short summary of current applications of CEST from each different category.

diaCEST agents

Diamagnetic particles are commonly used as both endogenous as well as exogenous CEST agents. A few examples of their main usage so far are presented below.

A major area of focus is the study of the CEST signal originating from the amide protons (figure 10) found in cellular proteins or peptides. This technique widely known as Amide Proton Transfer (APT) can benefit from the pH dependence of the proton exchange rate to measure pH changes in tissue. First published by Ward and Balaban in 2000 [4] and later by other groups, the APT signal was found to decrease

[1] Protons prone to chemical exchange either with their solvent or between them within the molecule

with pH reduction [5, 6, 7]. Additionally, studies in rats with induced ischemia[2] revealed decreased APT signal in ischemic regions compared to healthy brain regions [8, 9]. This is somewhat expected since lack of oxygen supply induces excessive production of lactate and therefore reduction of tissue pH. In particular Sun et al in 2006 [10] reported that APT can give information prior to any visible change from structural scans.

The APT technique is also found to give contrast between healthy and cancerous tissue as revealed by the studies of Zhou et al [11] and Salhotra et al [12]. The work published in 2010 by Zhou et al deserves special mention in this context, where the authors demonstrate differentiation between cancerous tissues and radiation necrosis where conventional MR methods failed [13].

Hydroxyl groups (-OH) have also been explored as potential CEST contrast agents. In 2007 Van Zijl et al demonstrated the use of infused glucagon to image glycogen production in mouse liver and named the method glycoCEST [14]. The same year Ling et al used CEST to image the hydroxyl groups on Glycosaminoglycans (GAGs) found in cartilage, as a diagnostic tool for osteoarthritis with the name gagCEST [15]. Lastly, a final method was developed that used native glucose to image high-metabolic tissues, such as brain and neoplasms, a technique called glucoCEST. The technique was demonstrated independently by Chan et al in 2012 in two breast cancer cell lines [16] and also by our own group, Walker-Samuel et al 2013 in two colorectal tumour cell lines [17]. Both studies showed an elevated glucoCEST signal in the tumours as expected due to the Warburg effect, linked to an increase in glucose consumption by neoplastic tissues. In our study, glucoCEST was also correlated with ^{18}F-FDG (fluorodeoxyglucose) autoradiography[3], a proof that the technique can give similar information to ^{18}F-FDG PET[4] (Positron Emission Tomography). The GlucoCEST method was also investigated by Nasrallah et al (2013), using a glucose analogue, 2-Deoxy-D-glucose (2DG) as a tracer in healthy rat brain [18] and Rivlin et

[2] Blood supply restriction which results in insufficient oxygen delivery to tissue

[3] ^{18}F-FDG is a glucose analogue used in PET as a radiotracer for the study of glucose metabolism

[4] ^{18}F-FDG PET is currently the gold standard in tumour detection

al 2014, using a different glucose analogue, 3-O-Methyl-D-Glucose (3OMG), in imaging tumours [19].

Moreover, molecules containing amine groups (figure 10) have been considered for their ability to exchange and therefore produce CEST contrast. For example Cai et al, 2012 have proposed the use of CEST to directly detect the amine groups of glutamate in the brain, and named the method gluCEST. The technique was applied in rat brain undergoing ischemia and an increased gluCEST signal was found in the ischemic region compared to the contralateral one. Cai et al in the same paper also presented the application of gluCEST in a rat brain tumour model, claiming an increased signal in areas of tumour compared to the healthy tissue [20]. This study and its results remain controversial in the field, due to the multiple possible sources of amine protons in the brain. Another example of native CEST contrast attributed to a single metabolite is the possible detection of creatine, first proposed by Kogan et al (2014), who applied creatine CEST (crCEST) to investigate metabolic changes in muscle after exercise [21]. CrCEST was also found by Haris et al (2014) to distinguish between healthy and myocardial infarction[5] in-vivo [22].

paraCEST agents

A parallel field of CEST research focuses on the use of paramagnetic particles as exogenous CEST contrast agents, a technique given the name paraCEST. Since 1998 when Aime et al [23] reported the detectability of the paramagnetic particle $EuDTMA^{3+}$ through water exchange with ^{1}H Magnetic Resonance Spectroscopy (MRS), a whole new class of CEST agents has been considered. With such a method, exogenous contrast agents can be manufactured to be sensitive to different parameters such as pH or temperature, with the potential to be used in-vivo as biomarkers [24, 25]. An example of such agents is given in the work of Zhang et al (2005), in which they presented the use of $EU(2)^{-}$ as a temperature probe with the paraCEST technique [26].

[5] Lack of blood flow (and therefore oxygen supply) due to blockage resulting in the heart muscle damage (Commonly known as heart attack)

hyperCEST agents

Hyperpolarized molecules have also been explored with the potential to become CEST agents. In 2006 Schroder et al demonstrated significant signal enhancement with the use of hyperpolarized Xenon, up to a factor of $>10^4$; much larger than any other CEST agent [27]. HyperCEST has been mainly investigated as a temperature sensor by Schroder et al [28] and also Schilling et al [29], but remain a laboratory tool so far, with a potential long road to translation.

1.2. What makes CEST so attractive

From the few examples outlined in section 1.1 we see how CEST has gained an increasing interest throughout the last two decades with enthusiastic researchers from all over the world wanting to explore more applications and possibilities within this field. What makes it so attractive is the ability to detect substances at very low concentrations by exploiting the proton exchange properties with water, resulting in amplification of the signal by orders of magnitude and overcoming the low sensitivity of MRS [30]. Thus, the possibility of molecular imaging with MRI becomes possible.

The fact that CEST agents depend on many physiological parameters is in some ways the greatest advantage but also disadvantage of the technique. CEST can serve as a pH probe, a mechanism that will be more explored in section 2.3, Chapter 4 and Chapter 6. It is also able to inform on the concentration of different metabolites and can be used for MR thermometry. Thus it can be advantageous in different applications and become a biomarker for various diseases. However, its dependency on so many parameters renders it rather difficult to quantify for its detractors. Both sides of this coin will be explored in this thesis, as explained below.

1.3. The aims of this work

Enthusiastic about the advantages of the CEST technique, we decided to investigate the endogenous signal and explore possibilities in which the CEST technique can be useful in-vivo.

This PhD project aimed first to implement and optimise CEST sequences for in-vitro use and compare the findings to the expected theoretical outcomes from a model based on the Bloch-McConnell equations. This would allow the study of basic CEST principles and further link the results to potential applications in-vivo.

Another aim was the implementation of CEST sequences for in-vivo use in mouse models of neurodegenerative diseases and investigation of the signal compared to control mice. The main aim was to see if the method was capable of detecting a subtle intracellular accumulation of proteins in the spinal cord of mice, a phenomenon at the basis of almost all neurodegenerative conditions. This project was therefore focused on the spinal cord, with the challenge to overcome the difficulties of performing an advanced MR technique in such a region.

Furthermore, inspired by the work of other researchers on the pH sensitivity of the CEST effect (section 1.1, diaCEST agents) we applied our methodology to with the aim to map the pH changes in the piglet brain following Hypoxia Ischemia, as a potential new biomarker of disease progression and response to therapy for neonates. Hence we had to develop another complete set of techniques and optimise our methods for brain applications as well.

Chapter 2. Background theory

This chapter aims to familiarise the reader with the CEST concept by underlining the fundamental Nuclear Magnetic Resonance (NMR) principles involved. Furthermore, the mathematical model which describes the exchange processes is also introduced, as well as the different exchange mechanisms.

2.1. Introductory Nuclear Magnetic Resonance theory

The principle of NMR was first introduced in 1946 by Bloch et al (Stanford University, [31]) who demonstrated the effect of signal detection from a water sample. Simultaneously in the same year Purcell et al (Harvard University, [32]) published their work when they managed to measure a contrast proportional to the amount of protons contained in a small paraffin sample. Bloch and Purcell shared the Physics Nobel Prize in 1952 for demonstrating, in different ways the principle of NMR. Over the last six decades NMR has been a major tool for the study of solid structures, organic compounds and other physical phenomena such as conductivity, exchange rates, etc., in chemistry, biology and physics. Furthermore, the demonstration of image formation with the same principle in 1973 by Lauterbur [33] was a milestone in modern medicine. Since then, NMR has been used in medical imaging for obtaining both structural and functional information from the human body [34].

Section 2.1 starts with some essential quantum mechanical principles (2.1.1) and then moves to the concept of net magnetisation evolution in time (2.1.2). The phenomenon of relaxation and the physical principles that govern it are also introduced (2.1.4). Finally, the theory of chemical shift in NMR is discussed as it is very important in a saturation experiment (CEST, sections 2.2 and 3.1).

2.1.1. Essential Quantum Mechanical Principles-Spin Behaviour

The behaviour of atomic nuclei is characterised by their intrinsic quantum mechanical properties. In NMR we are mostly interested in the spin quantum number S, (or usually referred to as just spin), a fixed quantity which can be either integer or half-integer and is characterised by the ground state[6] of the nucleus. The spin state of each nucleus is given by the spin angular momentum number (m_s) as follows

$$m_S = -S, -S+1, -S+2, \dots, S-2, S-1, S \quad (1)$$

On average the human body consists of approximately 60-80 percent of water [35], which makes hydrogen is the most abundant nucleus in our body. The variability of water content in different tissues [36], makes hydrogen an excellent candidate for imaging with NMR. Therefore, unless otherwise stated, hydrogens will be our main focus of interest. In a system of hydrogen atoms, each nucleus can have a spin angular momentum number of either ½ or -½, due to the spin number of the nucleus being ½. The same system under the influenced of a magnetic field B_0 along the z axis, comprises two energy states, with an energy difference as shown in equation 2 (see also illustration of the energy level splitting in figure 1).

$$\Delta E = \gamma \hbar B_0 \quad (2)$$

where γ is the gyromagnetic ratio, defined as the ratio between the magnetic dipole moment and the angular momentum of the specific nucleus and $\hbar$ the reduced Planck's constant (1.055×10^{-34} Js).

[6] The ground state is the state at which a quantum mechanical system is at its lowest energy possible

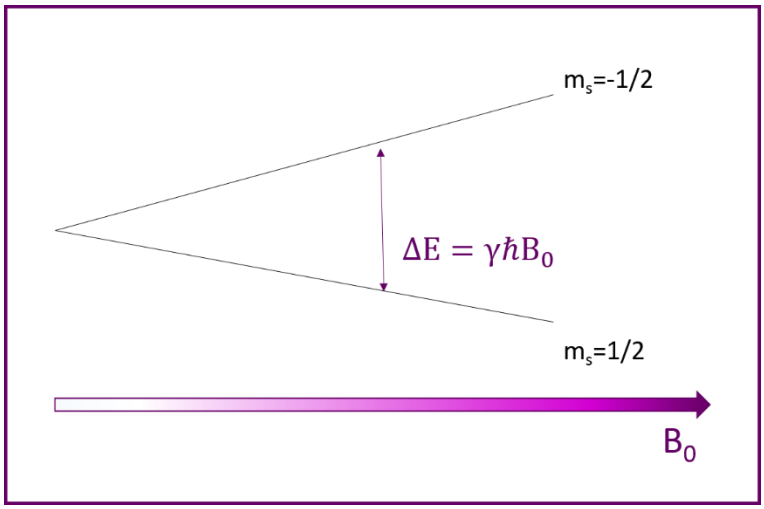

Figure 1: shows how, proportional to the static magnetic field B_0, the energy gap between the two spin states is increased. Spin number of ½ is also referred to as 'spin up' while spin number of - ½ as 'spin down'.

Each spin will precess about the z-axis with an angular frequency (ω_0) given by equation 3, also known as the Larmor equation named after Sir Joseph Larmor [37]. The equation describes in detail the influence of a magnetic field on a single spin in isolation.

$$\omega_0 = \gamma B_0 \qquad (3)$$

Depending on the z component of the angular momentum number, the two quantised spin populations are usually referred to in NMR as 'spin up' or 'spin down' populations, 'parallel' or 'antiparallel' to the applied magnetic field B_0 respectively. As spins tend to be in equilibrium at the lowest energy state, and the net spin population is align parallel to the applied magnetic field. This spin behaviour is described by the Boltzmann distribution where a system with two possible energy states favours the lowest energy state, and in thermal equilibrium distribute, as shown in equation 4.

$$\frac{N_+}{N_-} \propto e^{-\Delta E/kT} \qquad (4)$$

Where N_+ , N_- is the number of spins at high and low energy states respectively, k the Boltzmann's constant (8.62×10^{-23} J/K), T the system's temperature (in Kelvin) and ΔE is the energy difference between the two states as given by equation 2

Although each nucleus acts independently with discrete processes, it appears as a *continuous* single process at the macroscopic level due to the large number of nuclei involved in NMR. The nuclei *group* behaviour can be characterised by a single quantity, the average magnetic dipole moment density, known as nuclear net magnetisation M. Therefore for simplicity we can describe the system with a phenomenological approach through the Bloch equation (see below section 2.1.2)

2.1.2. Magnetisation evolution

The evolution of magnetization M in time under the influence of a magnetic field B can be described by equation (5).

$$\frac{dM}{dt} = \gamma M \times B \qquad (5)$$

Note that this equation is valid under the assumption that the spin system accounting for the net magnetisation, consists of identical spins with no interaction occurring between them. However this is not valid as interactions do occur within the spin system but also with other external spins as well; resulting in energy dissipation. This process, known as relaxation of the magnetisation, takes place when a system of spins is driven out of equilibrium by absorption of RF energy. Relaxation is typically categorised in longitudinal (along the z axis) and transverse (within the x-y plane); a more detailed description is given in section 2.1.4. The combined effect of magnetisation evolution taking into account for relaxation processes is described by the Bloch equations (given in section 2.1.3 by equations 6a-c).

2.1.3. Setting the reference frame

For convenience, the Bloch equations (given by 6(a-c) below) are analysed in terms of the Cartesian coordinate system where a static magnetic field B_0 exists along the z-axis and the application of any external RF energy B_1 is always perpendicular to B_0 with a precession frequency ω_{RF}. To minimise complications a rotating frame of reference is typically preferred over the static laboratory frame (figure 2a). The equations described in this section (equations 6 a to c) and moreover the equations used to define the CEST model (equation 17) are set in the RF frame (figure 2b). In

this case the coordinate system is rotating at frequency ω_{RF} and the applied B_1 field is static along the x or y axis in the transverse plane.

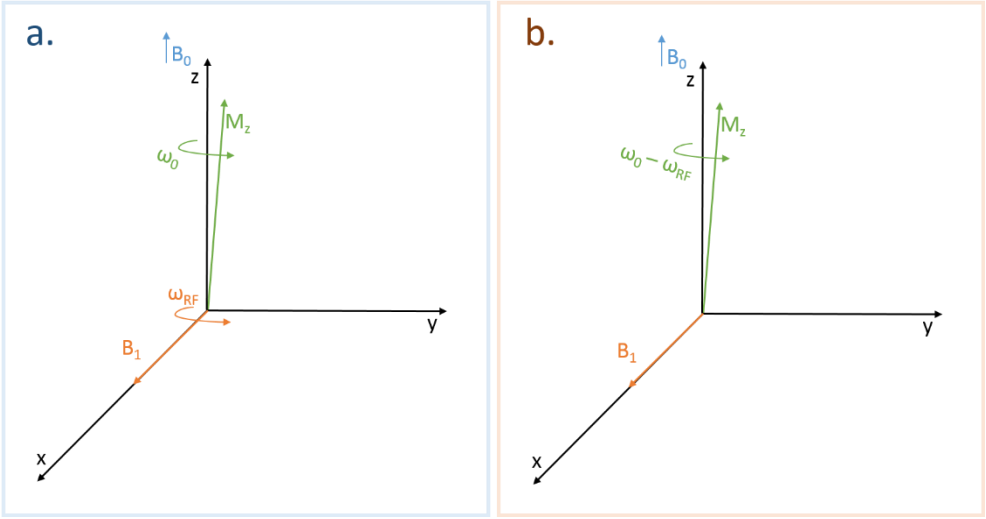

*Figure 2: Illustration of the laboratory (**a**) and RF (**b**) frames. The static magnetic field B_0 lies along the Z axis while the additional B_1 field is always perpendicular to the B_0 The laboratory frame is stationary with the net magnetisation M_z and B_1 precessing at angular frequencies of ω_0 and ω_{RF} respectively. However, in the RF frame, the B_1 is static while the net magnetisation M_z precesses at an angular frequency of ω_0–ω_{RF}. (When ω_0=ω_{RF} the external RF pulse is on resonance with the net magnetisation M_z, while at any other frequency the pulse is considered as off resonance).*

In section 2.1.2, equation 5 was introduced as an alternative to the quantum mechanical descriptions for a spin system. Here the x, y and z components of the same equation are modified to account for the relaxation processes (section 2.1.4) and also the application of an external RF pulse B_1 [37, 38]. The Bloch equations are given in 6 (a-c) below.

$$\frac{\partial M_x}{\partial t} = (\omega_0 - \omega_{RF})M_y - \frac{M_x}{T_2} \quad (6\text{ a})$$

$$\frac{\partial M_y}{\partial t} = -(\omega_0 - \omega_{RF})M_x - \frac{M_y}{T_2} + 2\pi\gamma B_1 M_z \quad (6\text{ b})$$

$$\frac{\partial M_z}{\partial t} = -2\pi\gamma B_1 M_y - \frac{M_z - M_0}{T_1} \quad (6\text{ c})$$

where in this case the RF pulse B_1 (in T) is applied along the x axis and the magnetisation M_z is tilted from z towards the y axis and γ is given in units of Hz T^{-1}. T_1 and T_2 are given in seconds.

2.1.4. Relaxation processes

The following section is focused on the different processes in NMR which lead to magnetisation relaxation.

2.1.4.1. Longitudinal relaxation

Consider the application of an RF pulse with enough energy to tilt the net magnetisation into the x-y plane (no net magnetisation left along the z axis); this system is no longer in equilibrium. The longitudinal relaxation is the process by which the net magnetisation returns to the system's thermal equilibrium (see Boltzmann's distribution, equation 4). In classical mechanics the evolution of the net magnetisation can be described by

$$M_z(t) = M_z^{eq} - [M_z^{eq} - M_z^0]e^{-t/T_1} \quad (7)$$

where M^{eq}_z is the net magnetisation along the z axis when the system is at thermal equilibrium, M^0_z the initial net magnetisation at time t=0 and T_1 the longitudinal relaxation time constant. Figure 3 is an illustration of the longitudinal relaxation process (equation 7) with different relaxation time constants T_1.

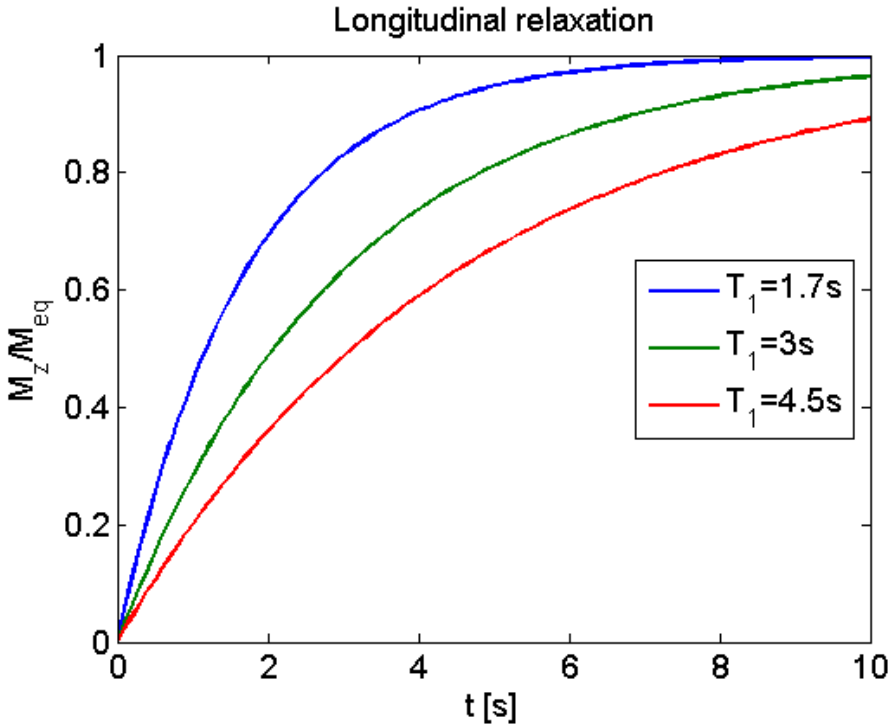

Figure 3: Net magnetisation recovery along the z axis. Illustration of the longitudinal relaxation process following an exponential trend with three different relaxation constants T_1.

Relaxation mechanisms

For nuclei of spin ½ the most effective relaxation processes occur due to the interaction of magnetic dipoles between the nuclear spin and other nuclei through space; a process called dipolar interaction. Random molecular (rotational and translational) motions alter locally the magnetic field at frequencies which energy exchange is allowed between spins and other molecules in the existing environment. These dipole interactions are strongly dependent on the gyromagnetic ratios (γ) and the proximity (r) of the nuclei involved (Dipolar factor β is proportional to $\left(\frac{\gamma_1\gamma_2}{r^3}\right)^2$). Due to the gyromagnetic ratio dependence, hydrogens experience a stronger coupling (γ_H=42.576 [MHz/T]) compared to other nuclei such as carbon (γ_C=10.705 [MHz/T]) or phosphorous (γ_P=17.235 [MHz/T]), [39].

In addition to dipolar interactions, unpaired electrons (from paramagnetic ions) can also cause magnetic fluctuations due to the electron movement in the magnetic field generating large magnetic moments. Such fluctuations can improve the relaxation efficiency dramatically. In fact, electrons are capable of promoting relaxation with a factor of half a million more compared to protons at the same distance from the

relaxing nuclei. This is the fundamental basis of paramagnetic contrast agents in NMR. Lastly, chemical shift anisotropy (CSA) is an important contribution to relaxation for non-symmetric molecules. The induced relaxation through CSA is proportional to the square of the field strength and also the chemical shift range exhibited by the nucleus. Nuclei with large chemical shift ranges are expected to be more prone to such a relaxation mechanism [40]. Hence CSA is of particular importance for sodium, phosphorous and fluorine but less for hydrogen [39].

Spectral Density function

The effectiveness of longitudinal relaxation is strongly dependent on the frequency of the molecular tumbling, which is described by the Spectral Density function (see equation 9 below) defined as the Fourier transform of the Correlation function for a given system. In short explanation, the Correlation function describes the temporal dynamics of a system driven by random processes at thermal equilibrium. As a first approximation the Correlation function is given by a mono-exponential decay, described by equation 8, [39]

$$G(\tau) = G_0 e^{-|\tau|/\tau_c} \quad (8)$$

where τ_c is the correlation time decay factor (short τ_c indicates fast molecular tumbling, liquids, while longer τ_c refers to slower motions, bound structures). Equation 9 below corresponds to the Spectral Density function of such a Correlation Function (equation 8).

$$J(\omega, \tau_c) = \frac{2\tau_c}{1+\omega^2\tau_c^2} \quad (9)$$

where $\omega=1/\tau$. Illustration of equation 9 is given in figures 4 and 5, where the Spectral density function is shown against the correlation time (τ_c) and the molecular tumbling frequency (ω) respectively (ω_0 is 400MHz, resonant frequency of hydrogen at 9.4T). For longitudinal relaxation, the closer the molecular tumbling is to the Larmor frequency, the more efficient the relaxation becomes. This implies an optimum correlation time of $\tau_c=1/\omega_0$ where correlation times that are shorter (free molecules) or longer (bound structures) than $\tau_c=1/\omega_0$ result in less efficient relaxation (longer T_1).

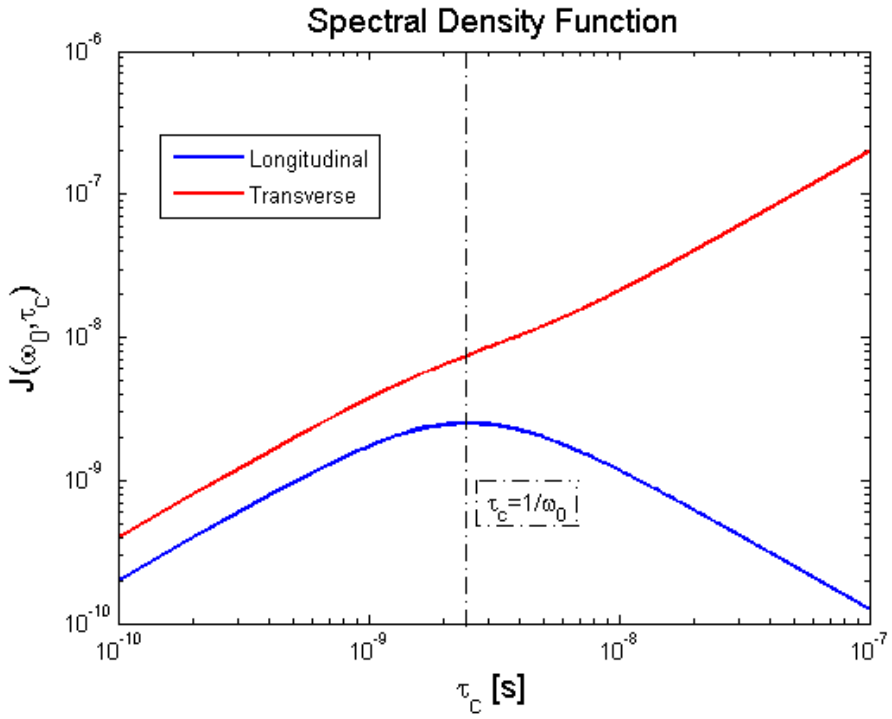

Figure 4: Spectral Density function with respect to the correlation time (τ_c). As the function is inversely proportional to the relaxation time, the graphs can give us an indication of the relaxation 'trends'. Longitudinal relaxation (in blue), is most efficient (therefore shortest T_1 time) when $\tau_c=1/\omega_0$, due to the molecular motions oscillating at the resonance frequency. For shorter ('free' structures) or longer ('bound' structures) τ_c the longitudinal relaxation becomes less effective (thus T_1 become longer). Transverse relaxation (in red) follows similar pattern to longitudinal relaxation for $\tau_c=<1/\omega_0$ (therefore for free structures the T_2 values are similar to T_1). For longer τ_c the transverse relaxations become more effective and as a result bound structures have very short T_2. This is due to the secular part of relaxation (see section 2.1.4.2)

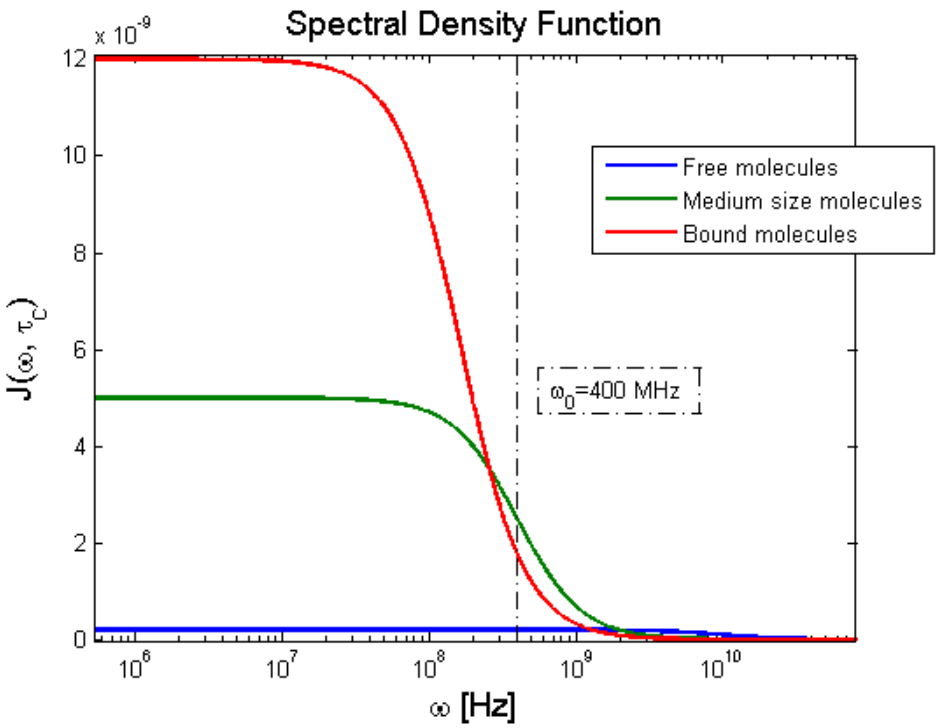

Figure 5: Spectral Density function with respect to the molecular oscillation frequency (ω) at three different correlation times (τ_c). This figure illustrates another way of looking at the relaxation effectiveness, as also seen from figure 4. Longitudinal relaxation, as mentioned before (see section 2.1.4.1), is most effective at the resonance frequency (ω_0), where in the same way, free (in blue) and bound (in red) molecules have longer relaxation times than medium sized molecules (in green). Also, close to ω=0, bound structures are the most effective in terms of transverse relaxation, due to dephasing.

2.1.4.2. Transverse relaxation

The longitudinal relaxation section described the general evolution of the net magnetisation along the z axis following the application of an RF pulse, which brings a proportion of net magnetisation into the x-y plane. Within the x-y plane, the net magnetisation decreases exponentially following the equation below

$$M_{xy}(t) = M_{xy}^{0} e^{-t/T_2} \quad (10)$$

Where M^0_{xy} is the transverse magnetisation at time zero and T_2 the transverse relaxation time constant. Figure 6 illustrates the transverse relaxation process (of equation 10) with three different relaxation time constants T_2.

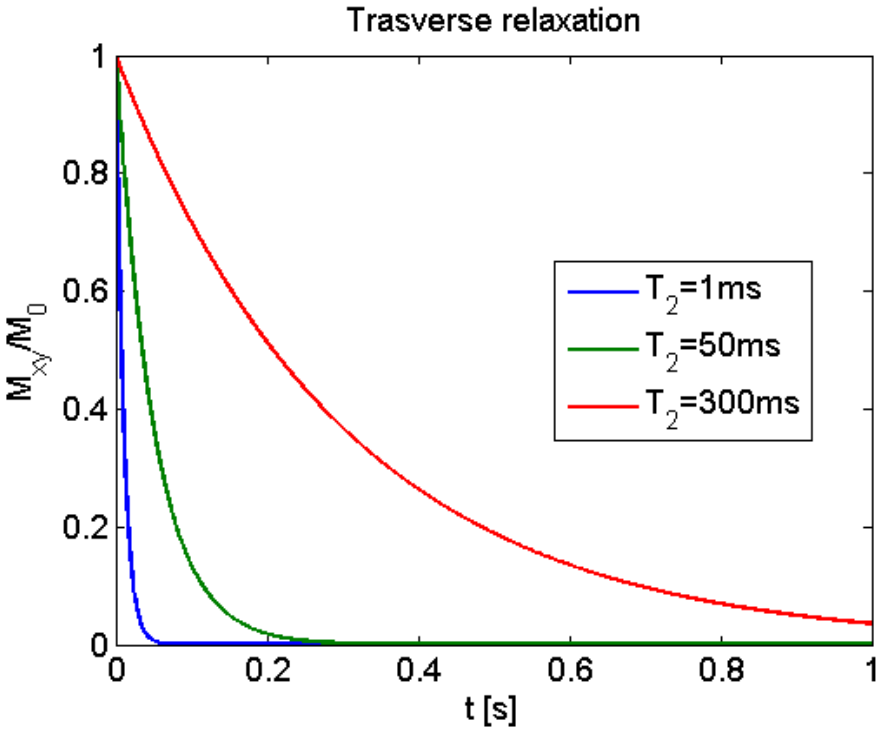

Figure 6: Magnetisation evolution within the x-y plane. Illustration of the transverse relaxation process following an exponential trend with three different relaxation constants T_2.

Additional transverse relaxation mechanisms

All processes which result in longitudinal relaxation, also contribute to transverse relaxation. Those processes are distinguished as the non-secular part of relaxation and they refer to any transitions occurring at or close to $\omega=\omega_0$. However across the transverse plane (x-y), an additional factor contributes towards the effectiveness of transverse relaxation, which does not dissipate energy to the surroundings but redistributes it within the system through an adiabatic route. This factor, referred to as the secular part of relaxation, occurs when the molecular tumbling is most restricted (with long correlation times τ_c and at $\omega=0$). When molecular motion is constrained (less tumbling) nuclear spins experience slightly different magnetic fields [41]. Local field inhomogeneities cause spins to precess at different Larmor frequencies, thus causing a net magnetisation dephasing across the x-y plane. The Spectral Density function is now altered to account for the secular part of relaxation, as shown in equation 11 (also refer to figures 4 & 5).

$$J(\omega,\tau_c) = 2\tau_c + \frac{2\tau_c}{1+\omega^2\tau_c^2} \qquad (11)$$

2.1.5. Chemical shifts

Chemical shifts in NMR are of fundamental importance as they distinguish magnetically non-equivalent atoms that are otherwise identical. In H-NMR spectroscopy, hydrogen atoms belonging to different molecules, or even hydrogen atoms within the same molecule but at different locations with respect to other nuclei, resonate at slightly different frequencies due to the fact that they experience a slightly different effective magnetic field B_{eff}. The principle of chemical shifts is the basis of NMR spectroscopy, and is equally important to CEST, as discussed in the following sections (see sections 2.2 and 3.1).

Spectroscopic frame Versus CEST frame

In conventional NMR spectroscopy the reference is usually set to the resonance frequency of the Tetramethylsilane (TMS) molecule. All other NMR signals are presented relative to TMS in parts per million (ppm). This was chosen mainly because all hydrogen atoms of the molecule are located in such a way that they all experience the same net magnetic field; hence only one peak is produced (magnetically indistinguishable hydrogen nuclei). Also due to the location of the hydrogen atoms relative to the carbon atoms, the shielding is extremely strong (see section 2.1.5.1) which means that the majority of the peaks in NMR will appear on the left side of the TMS peak (corresponding to a higher resonant frequency). In CEST experiments however, water is favoured over TMS as the reference (the water peak is at 4.7ppm from TMS, as shown in figure 7). To avoid confusion, the ppm range will always be given in reference to water unless otherwise stated.

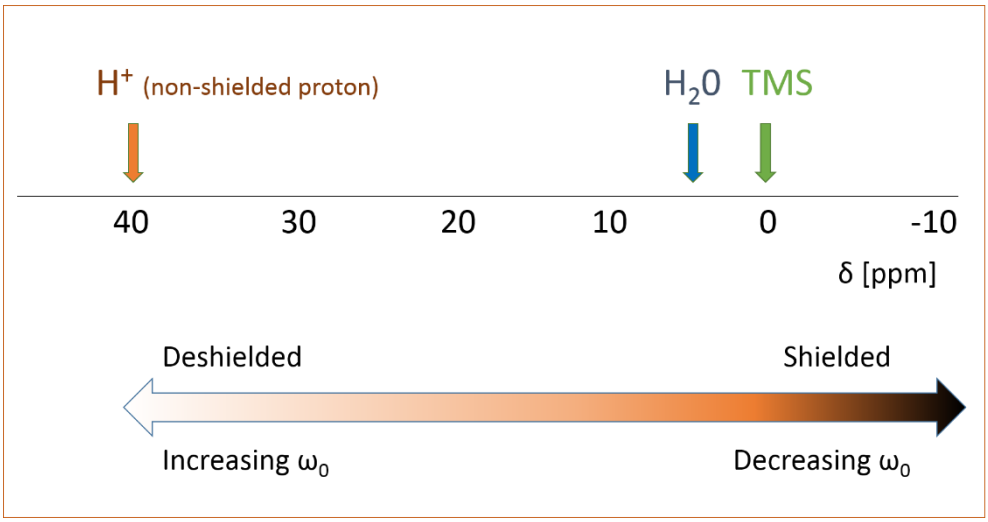

Figure 7: Illustration of the NMR scale for hydrogen. In NMR TMS is typically taken as the reference frequency, while water on this scale resonates 4.7ppm away from TMS. In the case of CEST experiments, the water peak is used as the reference. Furthermore the figure shows where a proton with no surrounding electrons (non-shielded) would resonate in reference to TMS. This is a completely deshielded proton which experiences the magnetic field $B_{eff}=B_0$ with no alterations. Any proton with electrons around it will experience a form of shielding which will lead to a decrease in the net magnetic field $B_{eff}<B_0$ that it experiences (for more see sections 2.1.5.1-2.1.5.3). In H-NMR most of the proton resonances lie within the 0-10 ppm range with water being at 4.7ppm.

Causes of chemical shifts include: *the Diamagnetic and the Paramagnetic factors* as well as *the Neighbouring Group Anisotropy* and *Electronegativity*. The following sections are intended as a brief description of the mentioned factors and their importance especially for hydrogen interactions.

2.1.5.1. The Diamagnetic factor

The diamagnetic effect causes *shielding* of a nucleus. Electron circulation in the s-orbitals[7] induces a magnetic field opposing the static B_0. Thus, the nuclei surrounded by these electrons will experience an effective magnetic field $B_{eff}<B_0$; this nucleus is *shielded* and has a resonance frequency ω shifted towards the TMS resonance frequency (refer to figure 7). Proton chemical shifts are highly dependent on the diamagnetic effect, also referred to as the *shielding factor and the effect is proportional to the density of the electron cloud.*

[7] The s-orbitals are spherical and symmetrical. One orbital can exist within each s-subshell and can hold up to two electrons (subject to the Pauli Exclusion Principle).

2.1.5.2. The Paramagnetic factor

The paramagnetic effect can cause larger shifts in the NMR scale compared to the diamagnetic factor. Any atom with asymmetric distribution of electrons in the p-orbital[8] can contribute to the paramagnetic factor when by circulation it transits between the ground and excited states. The induced currents unlike with the diamagnetic effect are in the same direction as the static magnetic field B_0 resulting in a $B_{eff} > B_0$. Since protons do not have electrons in any p-orbitals, they do not experience the paramagnetic effect in a direct way, although they are indirectly affected by neighbouring atoms, as described in the next section (2.1.5.3). Note that electron orbitals of higher complexity (such as d & f) are not discussed as they do not play an important role in organic compounds.

2.1.5.3. Neighbouring Group Anisotropy and Electronegativity

Magnetically anisotropic atoms or groups, caused either by paramagnetic or diamagnetic effects (see sections 2.1.5.1 and 2.1.5.2 above), will also affect the neighbouring nuclei through dipolar interaction. The net magnetic dipole due to anisotropy will perturb the dipole of nearby nuclei causing alterations of the effective magnetic field experienced by them, causing therefore shifts in the resonance frequencies.

Additionally, the *electronegativity* of adjacent nuclei can create chemical shifts. Electronegative atoms have the tendency to attract the sharing electrons within a bond towards them. As a result hydrogens attached to electronegative atoms (such as oxygen, nitrogen or carbon), get *deshielded* with chemical shifts away from the TMS resonance frequency and towards the 'naked' proton resonance (figure 7 for the NMR scale and figure 8 for a periodic table illustrating the most electronegative atoms).

[8] The p-orbitals are two lobed. Three orbitals can exist within each p-subshell (as it can hold up to 6 electrons). Therefore in a Cartesian coordinate system each p-orbital holds different dimension (x, y and z)

Note that both Neighbouring Group Anisotropy and Electronegativity effects are only dependent on the geometry of the molecules and therefore are constant regardless of the static magnetic field B_0.

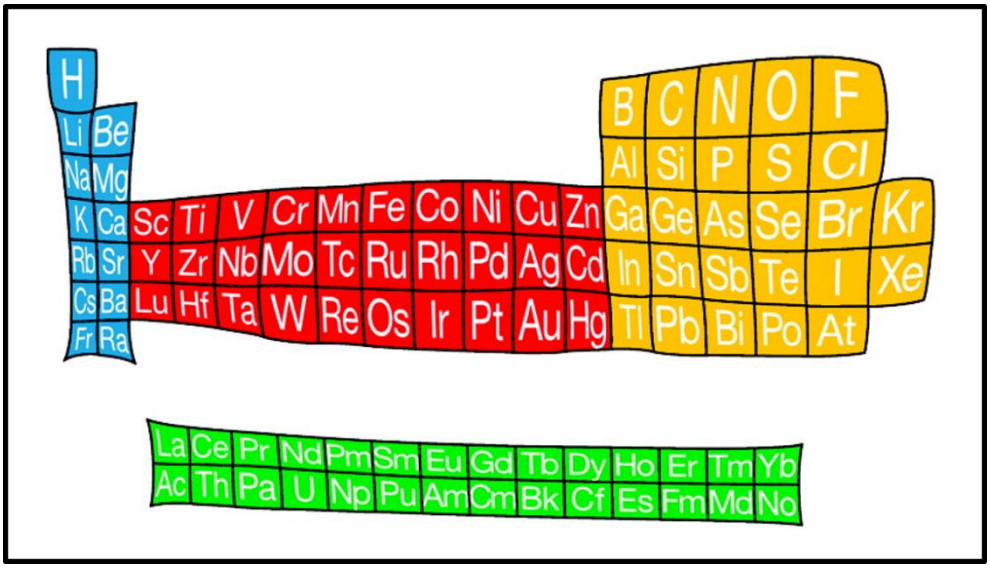

Figure 8: Illustration of electronegativity of atoms with a diffusion cartogram. Atoms corresponding to largest surface correspond to the most electronegative ones and vice versa. Top right corner elements of the table are the most electronegative. Atoms like oxygen, nitrogen, carbon and phosphorous which are found in-vivo, fall in the very electronegative range. In blue: Alkali and Alkaline earth metals, in red: transition metals, in green: lanthanide and actinide metals and in yellow: non-metals and metalloids. (Figure reproduced with kind permission from Winter Mark J., 2011. Full reference: [42])

Another important contributor of chemical shifts in NMR spectroscopy is J coupling[9], otherwise known as *fine structure splitting* or *spin-spin splitting*. However, in CEST experiments due to the lack of spectroscopic resolution (CEST resolution~in the order of 5Hz, while these structures could be as small as ~0.1Hz, [chapter 3.15 in [43]) such fine structure chemical shifts are not important as they are not observable [38]. Therefore J coupling is only mentioned as a matter of completeness, and will not be discussed further.

[9] J-coupling is a *'through bond'* interaction caused between neighbouring nuclei. Spin A perturbs the electrons surrounding it which therefore perturbs the electron cloud of spin B. As a result the energy levels of spin B are slightly affected, leading to frequency splitting within only a few Hz.

2.2. Magnetisation exchange mechanisms

The distinctive resonance frequency of different nuclei or similar nuclei at different magnetic environments was explained by the phenomenon of chemical shifts (section 2.1.5). Consider now two nuclei (named **A** and **B**) of the same gyromagnetic ratio (for example two hydrogen protons) with a resonance frequency difference ($\Delta\omega$.) between them. Spin **A** has a frequency ω_A and in a similar manner spin **B** a frequency ω_B (where $\omega_A \neq \omega_B$). In the absence of any interaction between the two spins if one irradiates the system with an RF pulse at frequency ω_A, in principle spin **B** should remain unaffected. If however an interaction **K** exists between the two spins, the magnetisation state of spin **A** will affect the state of spin **B** and vice versa. This is otherwise referred to as magnetisation exchange between two set of spins. Figure 9, summarises the principle of magnetisation exchange for a system of 2 spins as described here (A and B).

The basis of any saturation experiment is based on the principles of magnetisation exchange; in particular (as the name suggests) through chemical exchange. Within the next few sections the main mechanisms contributing to the CEST signal[10] will be explained. Section 2.2.1 is dedicated to chemical exchange while section 2.2.2 describes dipolar cross relaxation, the mechanism which gives rise to Magnetisation Transfer (MT) and also to Nuclear Overhauser Effects (NOE).

[10] Not only due to chemical exchange, but dipolar cross relaxation too (including NOE, MT) and relaxation contributions from T_1 and T_2; the name remains **CEST** and refers to the outcome of a **saturation experiment**.

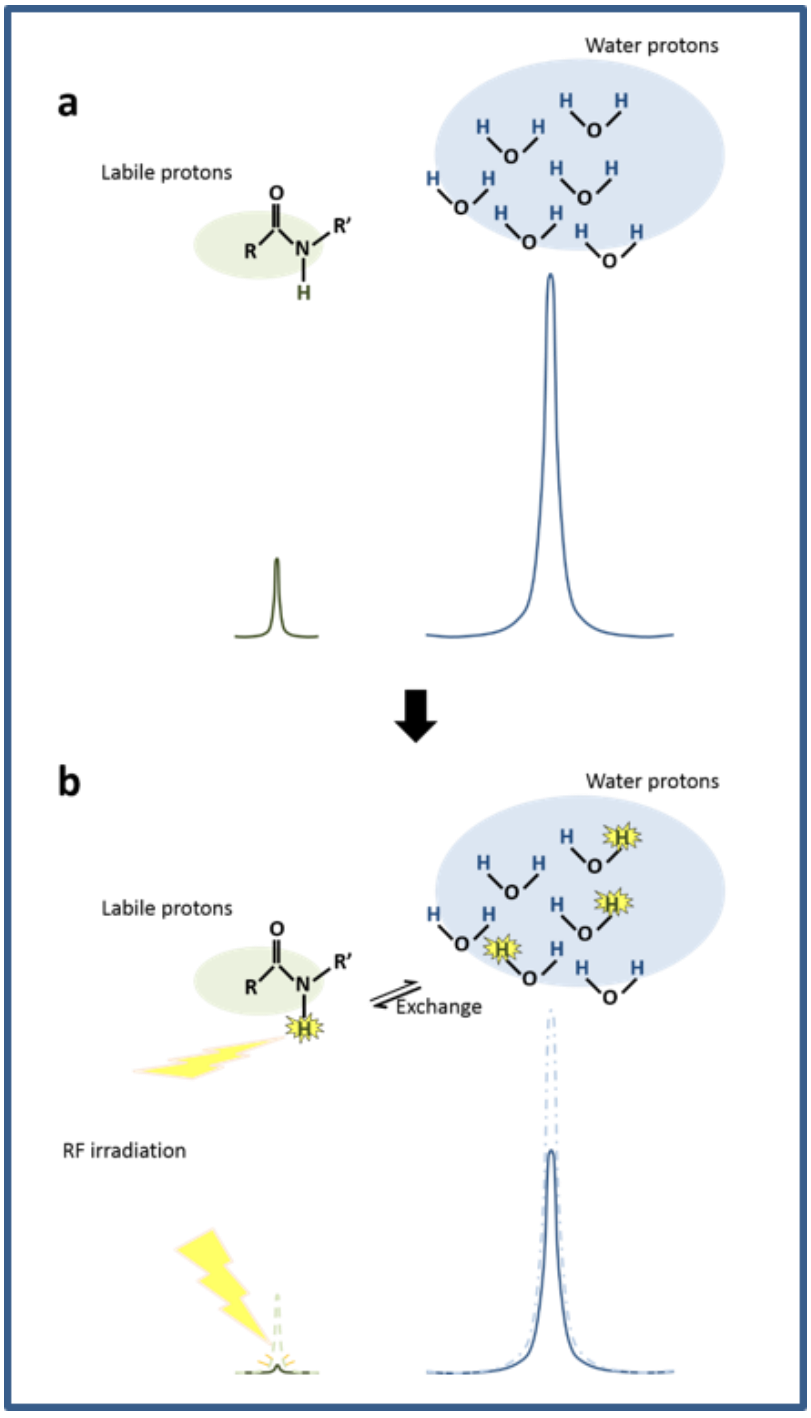

*Figure 9: Illustration of the chemical exchange process of protons. Part **a** shows the labile protons (small pool) and the bulk water (large pool) with their corresponding proton signal in NMR with no exchange linking the two pools. Part **b** however, demonstrates the two pools connected via a transfer rate. In a CEST experiment, labile protons are irradiated with an RF pulse at their resonance frequency; therefore their signal gets saturated. Due to the constant proton exchange between the two pools saturated protons from the small pool are transferred to the large water pool. If enough time[11] is allowed (in the order of seconds), this process leads to a detectable decrease in the water signal. The CEST contrast originates specifically from this signal decrease.*

[11] How much is *enough time* is discussed in section 2.3: '*Factors affecting the CEST signal*'.

2.2.1. Chemical exchange

The term *Chemical Exchange* in NMR is used to describe the phenomenon of nuclei exchanging between different chemical environments. Two types are distinguished, *intramolecular chemical exchan*ge when nuclei within the same molecule change position through internal motions and *intermolecular chemical exchange* where nuclei of one molecule interact with nuclei of another molecule through their shared environment [44].

The CEST technique in MRI usually refers to intermolecular chemical exchange of exchangeable protons of metabolites, peptides or proteins with the water protons surrounding them. A detailed description of the chemical exchange mechanism between protons of those group and free water is given in figure 9. CEST contrast is measured as the reduction in the water signal from part a to part b of the figure. An exception is found in paramagnetic CEST agents (paraCEST part in section 1.1), where the exchange can also be molecular [45]. However, for the purpose of this work, our main interest is the proton exchange. Functional groups prone to proton chemical exchange include Hydroxyl, Amine, Amide and Imino groups and are summarised below.

Exchangeable protons

Exchangeable protons which contribute to the in-vivo CEST signal are believed to originate mainly from proteins [45]. Figure 10 shows a peptide illustrating the type of protons that can be found in a protein: backbone Amide protons (in blue), and Amino acid side chain protons (Hydroxyl in orange, Amines in green and Amides in purple).

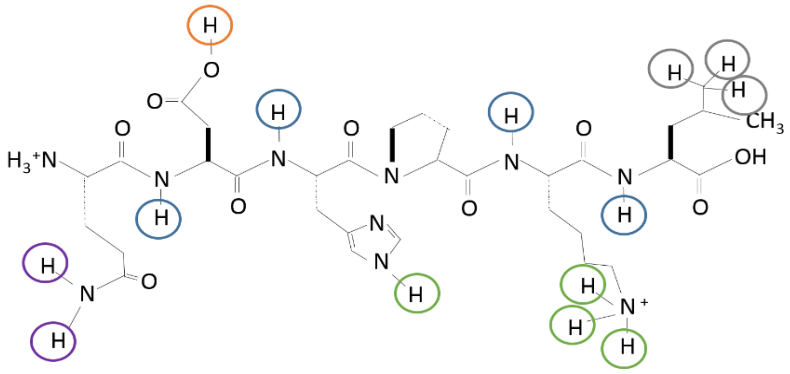

Figure 10: schematic of the peptide Glutamine-Aspartate-Histidine-Proline-Lysine-Leucine (Gln-Asp-His-Pro-Lys-Leu) to illustrate the different types of protons included on a protein. Non-exchangeable protons (in grey), backbone Amide protons (in blue), Hydroxyl protons (in orange), Amine protons (in green) and Amide protons (in purple).

Amide protons (figure 10, illustrated in blue) give a chemical shift ~3.5ppm (CEST frequency scale where water is the reference, see figure 7) and are usually found in the backbone of proteins. Amide proton exchange rate is in the slow to intermediate regime (also see section 2.3) with exchange rates < 30Hz [9] at physiological pH (~7).

Amine and Amide protons from side chain amino acids (figure 10 in green and purple respectively) resonate between 2-3 ppm from water and are in a faster exchange rate regime (150-1000 Hz), [46, 47]. Imine protons (-C=NH), a subgroup of Amine protons, also contribute to the CEST signal with a chemical shift between 5-6ppm and exchange rates ~3000-4000Hz (falling in the fast-intermediate regime), [48].

Hydroxyl protons (figure 10 in orange) can also contribute to the CEST signal. Like Amine protons, they are found on side chain amino acids, but also on smaller molecules like glucose, fructose as well as sugar polymers like cellulose, glycogen and glycosaminoglycan. Hydroxyl protons also fall in the fast-intermediate exchange rate regime (1000-10000Hz, [45]) and they resonate between 0.7 and 3ppm, [17]. Figure 11 is an illustrative graph of the exchange rate regime for the different hydrogen groups.

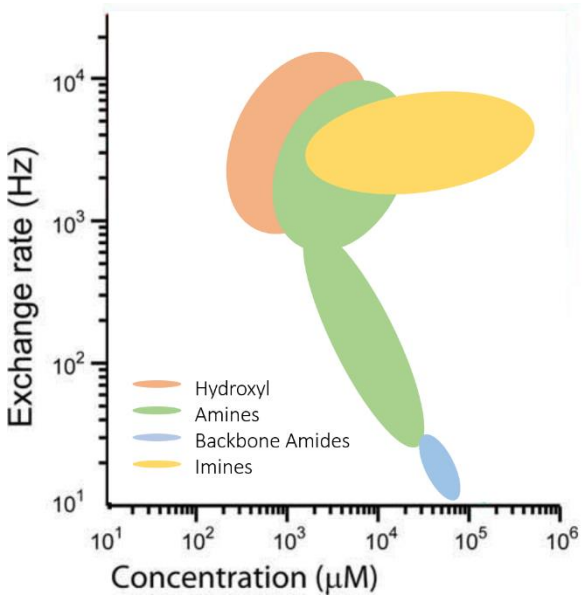

Figure 11: illustrative graph of the exchange rate regime vs concentration for different hydrogen groups: hydroxyl (in orange), backbone Amides (in blue), Amines (in green) and Imines (in yellow). Figure reproduced from Van Zijl et al 2011, [45].

2.2.2. Dipolar-cross relaxation

Chemical exchange is not the only way magnetisation is transferred between hydrogen species. Dipolar-cross relaxation is another transfer mechanism which contributes to the profile of the Z-Spectra during a saturation experiment. Unlike chemical exchange, dipolar-cross relaxation does not require proton transfer, yet the magnetisation exchange occurs through a system of coupled spins. This section briefly describes the Nuclear Overhauser Effects (**NOE**) and conventional Magnetisation Transfer (**MT**) **effect**, as they both arise from dipole-dipole coupling. Both effects can give valuable information [49, 50, 45], nevertheless when the purpose is to explore the chemical exchange effects, they might be referred to as 'CEST signal contaminations'

NOE can be generally categorised into homonuclear (interaction between equivalent atomic nuclei) or heteronuclear (interaction between different atoms). During proton-proton CEST experiments any observable NOEs are a result of homonuclear interactions. Medium size molecules (small proteins) can exhibit NOE effects through space (dipole-dipole coupling), hence the protons affected must be in very close

proximity (4-5 Å). Backbone -CH and –$COCH_3$ (Acetyl) hydrogen atoms once irradiated, perturb the magnetisation of water either directly (Direct NOE) or through perturbation of exchangeable protons (-NH, -NH_2, -0H) which can then interact with water (Exchange-relayed NOE). These effects take place within the same molecule, hence the NOEs are intramolecular. *Intramolecular* direct and exchange-relayed NOEs are believed to be a possible contributor[12] of CEST signal centred at -3.5ppm [51, 50, 52].

Intermolecular NOEs (between molecules) also exist however they only start to be significant in restricted mobility molecules, i.e. bigger protein chains surrounded by bound water (also known as the hydration layer, [53]). Here bound water molecules also undergo dipole-dipole interactions; these NOEs contribute to the **MT effect**. Interactions of this kind become faster as the size of macromolecules increases and structures become more 'semisolid' due to the stronger couplings and shorter relaxation times (see section 2.1.4). Hence, MT is not frequency specific but instead appears as a general lowering in signal throughout the entire Z-Spectrum (up to 80ppm away from water), [49] & [50]. Subsequently, the magnetisation is transferred from bound to free water molecules.

2.3. Factors affecting the CEST signal

As discussed in Chapter 4, the CEST signal is sensitive to a range of environmental factors; the exchangeable protons alone cannot guarantee a significant CEST contrast. Factors such as the concentration of metabolites, pH and temperature, field strength and T_1/T_2 relaxation times contribute to the CEST signal and are discussed in this section.

Simulations in this section demonstrating the CEST related parameters, are based on a three pool Bloch-McConnell system (see section 2.4). Unless otherwise stated, the parameters used for the simulations are given in table 1.

[12] See also section 3.1.1, *'The Z-Spectrum profile'*.

Pool No.	Frequency [ppm]	Pool size (ratio to water)	Exchange rate [Hz]*	T_1 [ms]	T_2 [ms]
1 (Water)	0	1	n/a	1700	37
2 (Amine)	2	0.0036	400	1000	10
3 (Amide)	3.5	0.0036	22	1000	10

**Exchange rates were estimated by the equations 15 and 16, as described by Desmond and Stanisz, 2012 [54].*

Table 1: parameters used for the simulations in this section

Concentration

The CEST signal is highly dependent on the concentration of exchangeable protons and has been reported by many groups as a method to determine the concentration of metabolites, [55, 15]; however the CEST detection threshold is considered to be limited to concentrations >5mM [56]. Figure 12 demonstrates the relationship of metabolite concentration to the MTR_{asym} calculated from the Z-spectra using equation 22.

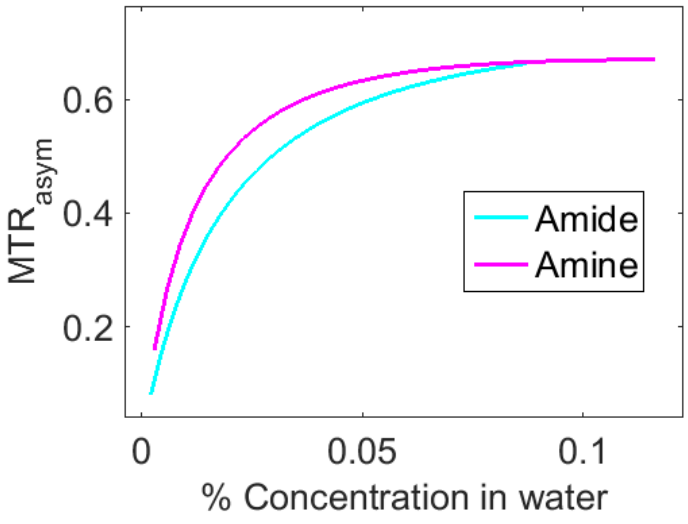

Figure 12: simulation of the MTRasym with different concentration of amide protons (in light blue) and amine protons (in pink). Concentration of metabolites is given in percentage fraction to the water concentration. MTRasym was calculated at 2ppm and 3.5ppm from water for amine and amide protons respectively.

Exchange rate

The exchange rate between metabolites also significantly affects the CEST signal. The exchange rate between the exchangeable site and water should be within the same order of magnitude as the chemical shift between them [45]. Ideally exchange rates should fall in the *intermediate exchange* rate regime, as figure 13 shows. Any exchange rate below or above the intermediate regime gives a reduced (and eventually no) CEST signal.

At the very slow exchange rate regime ($\Delta\omega >> K$), the CEST effect is limited as relaxation effects dominate. This means that the saturated protons do not have enough time to sufficiently exchange with water and transfer their magnetisation state before relaxation (mainly longitudinal) occurs in water. Similarly minimised CEST effects are found at the very fast exchange rate regime ($\Delta\omega << K$), where no distinction of frequencies is observed between the two individual species as they both appear at the same frequency [57].

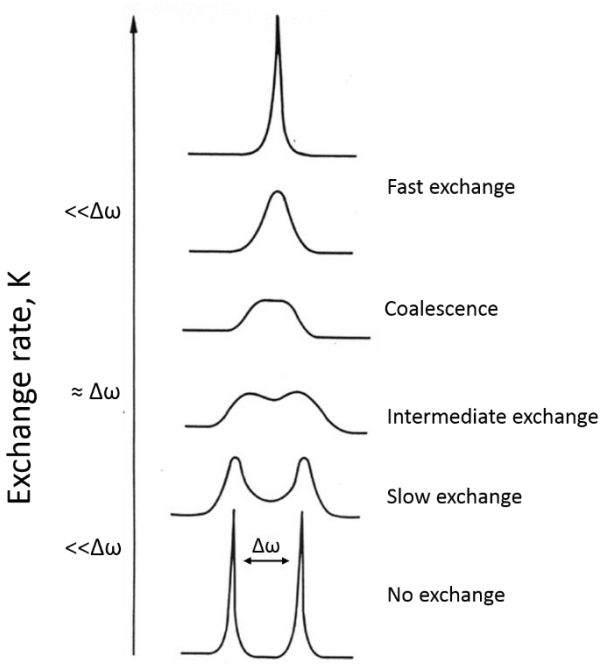

Figure 13: Illustration of symmetric (same concentration) two-side exchange where each population has a unique chemical shift on the NMR spectrum and a $\Delta\omega$ shift exists between them. In the no/very slow exchange limit ($\Delta\omega >> K$) there is no CEST effect observed, as no transfer of magnetisation can occur without exchange. Likewise in the very fast exchange limit ($\Delta\omega << K$) the two unique chemical shifts no longer exist, rather they merge into a single peak.

The hydrogen exchange rate (K) is governed by the **structure** of the molecules. For example protons belonging to folded proteins have exchange rates much slower due to the folding protection factor [58]. Also protons located in the interior of a molecule will have *reduced accessibility to the solvent* compared to protons on the surface, resulting in less contribution in the exchange process. Additionally, the exchange rate is greatly affected by environmental changes such as **pH** [59, 60, 61], **temperature** [14, 56] and other **exchange catalysts** [62] as shown in equation 12.

$$K = k_a \times 10^{-pH} + k_b \times 10^{pH-pK_w} + k_0 \quad (12)$$

where K_a and k_b are the *acid- and base-catalysed* rate constants respectively and k_0 a combined constant representing contributions from other *exchange catalysts*. pK_w is related to the water auto-dissociation (≈ 14 at 25° C). The three catalyst constants of equation 12 (K_a, K_b and K_0) are also dependent on the *temperature* of the solution as described by the Arrhenious equation (13) below

$$k_x = Ae^{-E_a/RT} \quad (13)$$

where R is the universal gas constant ($8.314X10^{-3}$kJ/mol/K), E_a is the activation energy (given in kJ/mol) and A is a reaction constant.

Depending on the acid- and base-catalysed proton transfer [63, 64], a pK_a value (logarithmic acid dissociation constant) is assigned for different protons which describes the equilibrium state of a solution for a given pH (equation 14).

$$\frac{[X-]}{[HX]} = 10^{pH-pK_a} \quad (14)$$

where [HX] and [X] are the relative concentration of ions in the solution.

Qualitatively and in simplistic terminology, equation 14 states that for a base-catalysed proton exchange the protonated form (HX) dominates, while in the case of an acid-based proton exchange the ionised form (X) dominates instead. Baring in mind equation 14, one can deduce the exchange rate versus pH for a variety of protons. For example, the exchange rates for Amide and Amine protons are given in equations 15 and 16 respectively, as reported by Desmond and Stanisz, 2012 [54].

$$k_{amide} = 5.57 \times 10^{pH-6.4} \quad (15)$$

where K_{amide} the exchange rate of Amide protons to water.

$$k_{amine} = 10^{pH-4.4} \quad (16)$$

where K_{amine} the exchange rate of Amine protons to water.

In a range of pH from 3 to 9 the exchange rates of both Amide and Amine protons are base-catalysed. Figure 14 shows the relationship of the proton exchange rate with pH as described by equation 15, [9].

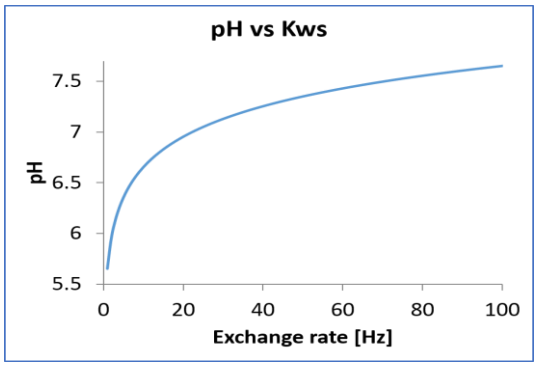

Figure 14: Proton exchange rate relationship to pH variation as described by equation 15.

Figure 15 illustrates simulated data of the MTR_{asym} calculated at the Amide and Amine frequency where the exchange rates were modulated by the above equations respectively.

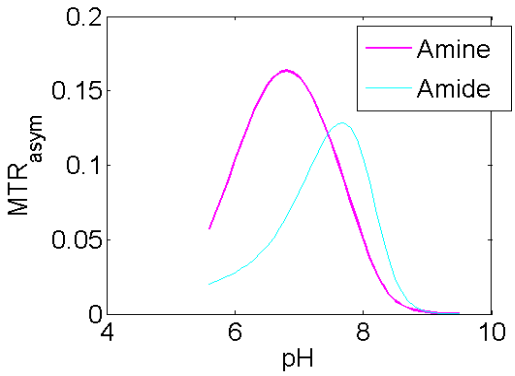

Figure 15: simulation of the MTRasym with different pH for amide protons (in light blue) and amine protons (in pink).

Relaxation times

Relaxation times also affect the CEST signal, as simulations reveal (figure 16), therefore one must be cautious when comparing CEST contrast in tissues with different T_1 and T_2 values.

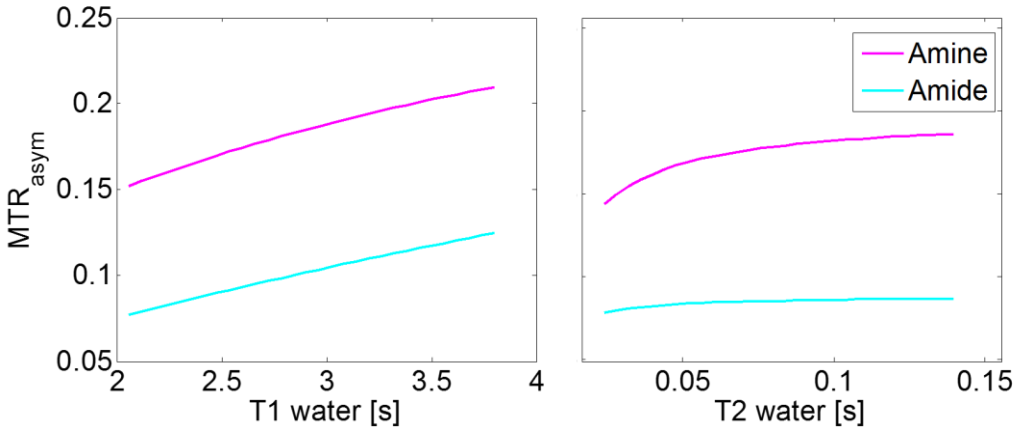

Figure 16: simulation of the MTRasym with different T1 (figure on left) and T2 (figure on right) of amide protons (in light blue) and amine protons (in pink)

Data in Chapter 4 also demonstrate the relaxation time dependence of the CEST signal.

Field strength

Field strength affects the CEST signal in an indirect way. For example, the fact that T_1 values increase with higher field strengths, affects the CEST values. In addition, high field strength results in greater chemical shifts between metabolites and water protons, [65], causing higher spectral resolution across the Z-Spectra and, therefore allowing for rapidly exchanging species at low field to become CEST-detectable at higher field.

2.4. Modelling the CEST signal

The coupled Bloch-McConnell equations were first introduced to explain MT effects [49, 50]. Recently the model was modified to accommodate rapid chemical exchange processes from multiple pools [66, 67, 68]. A theoretical model helps with the optimization process and the choice of pulse sequence parameters and is a great tool for researchers trying to understand the fundamentals of the exchange theory.

2.4.1. The coupled Bloch-McConnell equations

Consider a two pool model where pool A is the large water pool and pool B is much smaller and contains the exchangeable site protons, for example amide groups of protein molecules. Figure 17 shows the basis of a two pool model where the water protons (pool a) and the labile protons (pool b) are considered as individual pools with net magnetizations M_0^a and M_0^b respectively. k_{ab} is the exchange rate of protons transferred from pool a to pool b and k_{ba} vice versa. In the simplest model these two exchange rates are considered equal using a first order approximation [55] and therefore one term is used, K.

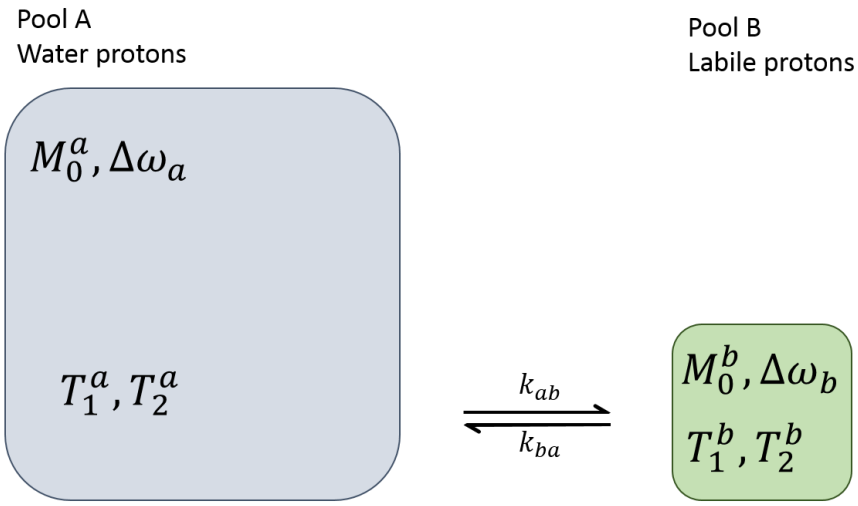

Figure 17: Illustration of the exchange process between two pools a and b. The exchange rates k_{ab}= k_{ba} = k in the simplistic form of the model. $\Delta\omega_a$ and $\Delta\omega_b$ are the chemical shifts of pool a and b respectively. If pool a represents water then $\omega_a = 0$

The model illustrated in figure 17, can be summarised in a matrix form as shown below in equation 17.

$$\begin{bmatrix} \partial M_x^A/\partial t \\ \partial M_y^A/\partial t \\ \partial M_z^A/\partial t \\ \partial M_x^B/\partial t \\ \partial M_y^B/\partial t \\ \partial M_z^B/\partial t \end{bmatrix} = \begin{bmatrix} -k_{ab} & \Delta\omega_a & 0 & k_{ba} & 0 & 0 \\ \Delta\omega_a & -k_{ab} & -\omega_1 & 0 & k_{ba} & 0 \\ 0 & -\omega_1 & -k_{ab} & 0 & 0 & k_{ba} \\ k_{ab} & 0 & 0 & -k_{ba} & \Delta\omega_b & 0 \\ 0 & k_{ab} & 0 & \Delta\omega_b & -k_{ba} & -\omega_1 \\ 0 & 0 & k_{ab} & 0 & -\omega_1 & -k_{ba} \end{bmatrix} \begin{bmatrix} M_x^a \\ M_y^a \\ M_z^a \\ M_x^b \\ M_y^b \\ M_z^b \end{bmatrix} - \begin{bmatrix} M_x^a/T_2^a \\ M_y^a/T_2^a \\ (M_0^a - M_z^a)/T_1^a \\ M_x^b/T_2^b \\ M_y^b/T_2^b \\ (M_0^b - M_z^b)/T_1^b \end{bmatrix} \quad (17)$$

where $M_x^{A,B}, M_y^{A,B}, M_z^{A,B}$ are the magnetisation components of pool **A** and **B** at time t along the x, y and z axis respectively. $\omega_1 = 2\pi\gamma B_1$ represents the angular speed of the magnetisation vector along the x axis due to the B_1 field (caused by the application of an RF pulse in the x direction). $\Delta\omega_{a,b} = \omega_{RF} - \omega_{a,b}$, represents the chemical shift between the applied RF pulse and the resonance frequency of the pools **A** and **B** respectively, where ω_{RF} is the frequency of the saturation pulse. Exchange rates correspond to $k_{ab} = k_{ba} = k$ (due to the first order approximation as mentioned above).

This set of differential equations describe the effect of magnetisation loss from pool A to pool B, given by $k_{ab}.M_z^a$ and as a result the gain of magnetisation of pool B, given by $k_{ba}.M_z^b$.

2.4.2. CEST simulator in Matlab

The set of equations described in section 2.4.1 (equation 17) were the basis for the CEST simulator built in Matlab by Francisco Torrealdea (PhD student, Institute of Neurology) and myself. Even though the equations here describe a two-pool model, it is straightforward to add extra pools and accommodate for additional exchangeable sites (see Appendix A). Two versions of the Model were built: a dynamical model, which solved the equations as a function of time in order to investigate the magnetisation evolution during the saturation process (simulations are also included in Walker-Samuel et al, [17]) and a steady state model (equation 18), which was used to investigate the Z-spectrum profile with different parameters.

$$\frac{dM_x}{dt} = \frac{dM_y}{dt} = \frac{dM_z}{dt} = 0 \quad (18)$$

Simulated data are used throughout the thesis as part of the discussion, with the specific parameters used always provided in an accompanying table. Description of the simulated models is included in Appendices B and C for steady state and dynamic solutions respectively.

Chapter 3. From theory to practice

The theory of magnetisation exchange mechanisms was described in section 2.2. The following chapter aims to give the reader a more practical perspective on how to acquire CEST data with MRI and how to calculate and interpret the resulting CEST contrast once the data have been acquired.

3.1. How to obtain Z-Spectra with MRI

A CEST experiment consists of two parts as described in the following two sections: off resonance saturation (section 3.1.2) and on resonance readout (section 3.1.3). The water frequency is considered to be on resonance. The Z- Spectrum (also referred to as the CEST spectrum) is the range of water signal intensities achieved as a function of repeated CEST experiments for multiple off resonance frequencies (more details on the shape of the Z-spectrum in section 3.1.1).

3.1.1. The Z-Spectrum profile

Let us consider a case where a water phantom is placed in the MRI scanner for a CEST experiment. Irradiation at any frequency offset away from water resonance frequency should not influence the water magnetisation and the outcome should still be of maximum signal. However, when an RF pulse is applied close to water frequency, it can perturb the magnetisation by causing direct saturation of water (also known as the spillover effect) [69]. Direct saturation is symmetrical around the water frequency and depends on the RF pulse bandwidth, frequency offset, length and power. It also depends on the relaxation time of water T_1 and T_2. The shape of the direct saturation can be deduced from the steady state solution (equation 18) of the Bloch equations (equations 6 a-c), given below in equation 19.

$$M_z = \frac{M_0}{1+\frac{(2\pi\omega_1)^2 T_1 T_2}{1+\Delta\omega_{rf}^2 T_2^2}} \qquad (19)$$

where ω_1 (Hz) is the applied RF power (γB_1) at offset ω_{rf} (Hz).

Figure 18 shows a simulated Z-Spectrum of a water only pool, deduced from equation 19. Parameters used for the simulation: M_0=1, T_2=300ms, T_1=3000ms, B_1=0.5μT.

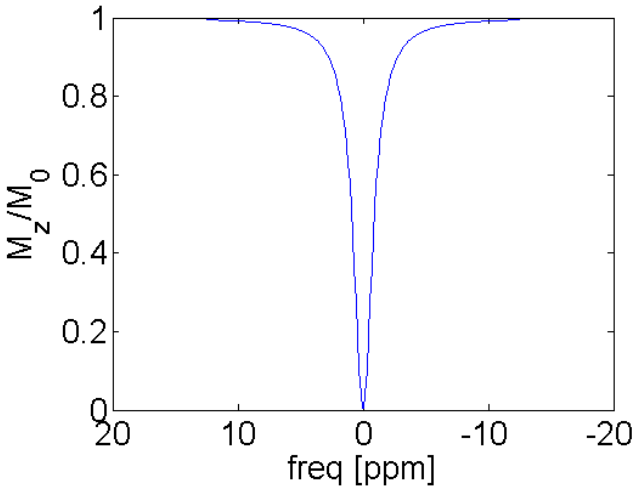

Figure 18: simulation of the direct saturation (Lorentzian shape) as derived from the steady state Bloch equations (6 a-c). Parameters used for the simulation: M_0=1, T_2=300ms, T_1=3000ms, B_1=0.5μT.

If now the water phantom also contains proteins and peptides containing exchangeable protons, a decreased signal will be observed at the corresponding chemical shifts of each proton. This is due to the magnetisation exchange principle (described in section 2.2) of proteins and peptides to the water surrounding them. The peaks observed will be related to the concentration of the solutes, the exchange rates, temperature and pH (as already explained in section 2.3). Figure 19 shows the difference between the water profile (dashed line) and to the profile of a solution containing exchangeable protons.

By looking at the Z-Spectrum, without any further analysis[13], there are a few characteristic features to comment on. The peaks resonating at 2 and 3.5 ppm from water correspond to Amine and Amide protons respectively as discussed in section 2.2.1 .

The source of the broad peak in the aliphatic region, centred between -3 and -3.5ppm is still a matter of debate [70] as aliphatic groups (-CH) in proteins, phospholipids and other fats[14] could all potentially be sources. Even though hydrogens from fat do not have the ability to chemically exchange with water, when an RF pulse is applied at -

[13] Data interpretation and further analysis is discussed in section 3.2.
[14] Like mobile lipid droplets, triglycerides, fatty acids, lipoproteins and cholesterol.

3.5ppm the fat signal is directly saturated, which therefore decreases the *total* signal at the corresponding frequencies of the Z-spectrum. It is also likely that the peak is partially attributed to NOE effects, as discussed in section 2.2.2 or other spin diffusion effects [71]. Moreover, the general lowering of the signal compared to the water profile is the result of MT (see section 2.2).

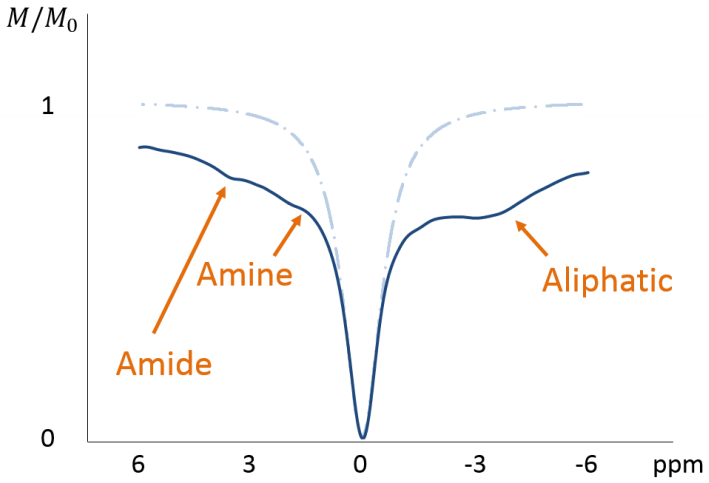

Figure 19: Sampled data borrowed from Chapter 5 acquired from the spinal cord of a healthy mouse. Z-Spectra for comparison of the water profile with (in solid line) and without (dashed line) the influence of other exchangeable protons (such as proteins and peptides).

3.1.2. The Saturation part of a CEST acquisition

A system is considered to be in a state of 'saturation' when it exists in a non-equilibrium state and with net magnetisation zero. Let us first consider again the two pool exchange system introduced in section 2.2.1, where pool A corresponds to the net magnetisation of water hydrogens (at resonance frequency $\omega_\alpha = 0$) and pool B the net magnetisation of a molecule with labile hydrogen protons (at resonance frequency ω_β). In order to achieve CEST contrast, pool B must remain in a saturation state for a period of time which is long enough for sufficient magnetisation exchange to occur between the two pools. The saturation scheme is on the order of seconds; typically a duration of 5 seconds is enough to reach steady state (see figure 20 for simulations

illustrating steady state of M_z, pool A). Therefore during a CEST experiment the application of saturation RF pulses is often the longest part of the overall acquisition.

Saturation can be achieved by either a continuous wave pulse (CW) or a train of pulses. CW-CEST, the traditional way to achieve saturation [5], it is more straightforward and it can be easily simulated by the Bloch-McConnell equations. The use of CW pulses is described in many studies with a variety of pulse durations. Cai et al 2012, use a 2 second CW pulse for the investigation of glutamate [20], while Van Zijl et al 2007, a 10 second CW pulse for imaging glycogen [14]. Somewhere midway, Salhotra et al 2008, use a 4 second CW pulse for the investigation of Amide protons in rodents bearing glioblastomas [12]. Despite the simplicity regarding quantification from the Bloch McConnell equations, the CW pulse saturation scheme is not suited for the hardware in clinical systems nor does it comply with the specific absorption rate (SAR) limitations if the pulses used are of long duration. To overcome this, pulsed CEST was considered as an alternative option, slightly more complicated in terms of quantification, but with feasibility in the clinic. Studies by Zu et al 2008 [5], Sun et al 2011 [6], Sun et al 2008 [5] and Dula et al 2013 [72], explore pulsed CEST for the use in the clinic, reporting its feasibility and comparable results with CW CEST. The duration of the saturation pulses is important in a CEST experiment as it affects the excitation frequency bandwidth. This could result in 'weighting' some frequencies more compare to other ones if not enough time is allowed between each saturation experiment. For example in the experiments to follow, a bandwidth of 52Hz was achieved with pulse duration of 50+5ms (excitation and interpulse delay respectively). The off resonance array was acquired in steps of 64Hz, allowing space between measurements without interference due to the saturation pulses.

Figure 20 shows the evolution of M_z (pool A) for pulsed (left) and CW (right) saturation schemes, with the effective CEST signal. Data were simulated using a two pool dynamic model (based on description in section 2.4, Appendix C) with parameters given in table 2 below. The equivalent B_1 calculations are shown in Appendix D.

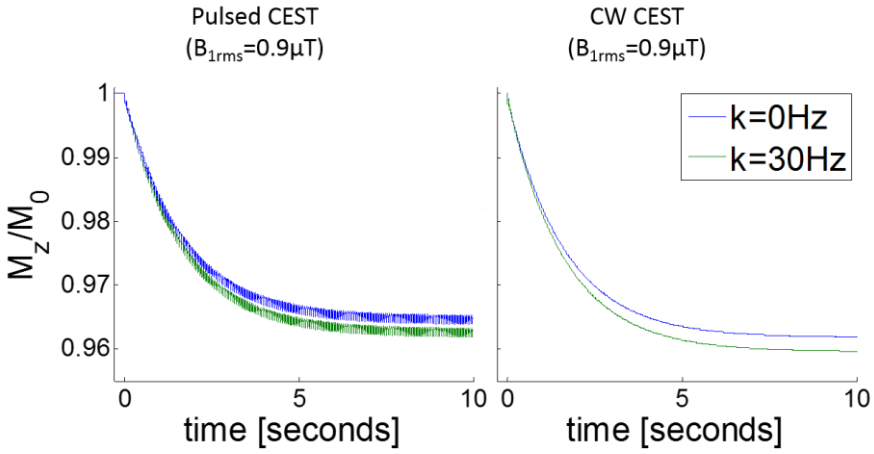

Figure 20: Simulations of the M_z (water, pool A), showing the CEST effect when connected to pool B via exchange rate K (in green) and when not connected to any pool (in blue). The difference of blue to green graph gives the net CEST effect in both figures. On the left saturation was achieved by a pulsed CEST acquisition (FA=540, 50 ms duration, 95% duty cycle (5ms inter-pulse delay), 200 pulses summing up to 10 s duration of B_{1rms}=0.9μT). On the right saturation was achieved by a CW CEST acquisition (CW pulse of 10s duration, and B_{1rms}=0.9μT). B_1 RF pulses were applied on resonance to the exchangeable pool frequency (3.5ppm).

Pool No.	Frequency [ppm]	Pool size (ratio to water)	T_1 [ms]	T2 [ms]
1 (Water)	0	1	1700	37
2 (Amide)	3.5	0.0036	1000	10

Table 2: list of the parameters used for the simulations in figure 20.

The saturation efficiency depends on the species to be labelled as reported by Snoussi et all 2003 [73], Van Zijl et al 2011 [45] and Zais 2013 [74]. Due to the variety of exchange rates for different groups (as discussed 2.2), the efficiency will vary with saturation power applied, as shown by the following equation (20) for mobile solutes (ignoring transverse relaxation).

$$\alpha \approx \frac{(\gamma B_1)^2}{(\gamma B_1)^2 + k^2} \qquad (20)$$

where α is the labelling efficiency, k the exchange rate between the sites, γ the gyromagnetic ratio of hydrogen (rad/s/T) and B_1 the RMS amplitude of the saturation pulse. The equation indicates that for fast exchangeable protons, higher power is required to efficiently saturate them which in the clinic might be a problem due to the SAR limitations [45]. Figure 21 is an illustration of equation 20 for a set of B_1 and k values.

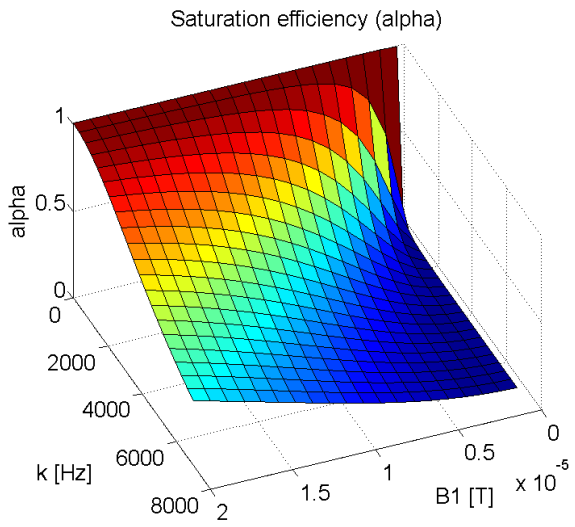

Figure 21: illustration of the saturation efficiency (α) for a set of exchange rates (k) and B_1 saturation amplitudes.

In theory, the faster the exchange between protons, the higher the power required to maintain a 'saturation state'. However, this relationship is only true for exchangeable protons with large chemical shifts; the closer the chemical shift is to the water resonance frequency, the more direct saturation of the water will also be present. Figure 22 demonstrates how the maximum CEST signal, calculated by the MTR_{asym} (see section 3.2, equation 22) at the frequency of the exchangeable site resonance varies with different B_1 amplitude (simulation of a four pool Bloch McConnell model, see section 2.4 with parameters given in table 3). The figure shows the difference between two, otherwise similar exchangeable protons, with different chemical shifts (close to water in solid lines and 50ppm off in dashed lines). Light blue solid line corresponds to an Amide group, with exchange rate of 30Hz and resonance frequency at 3.5ppm, as shown to resonate in vivo [69], while light blue dashed line indicates the same group now resonating at 50ppm from water, in order to avoid any direct saturation effects. Similarly, pink line corresponds to an Amine group with exchange rate of 400Hz resonating at 2ppm (solid line) and 50ppm (dashed line).

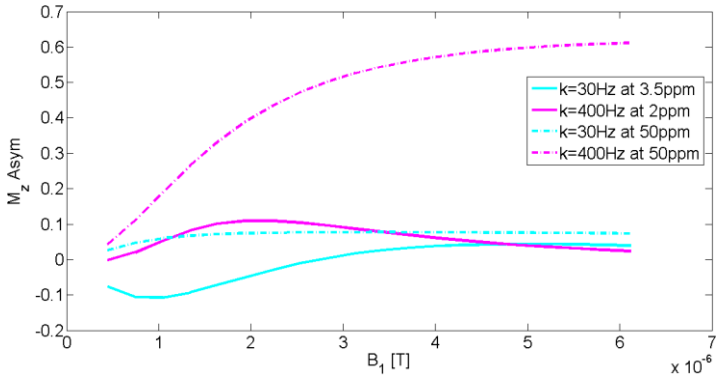

Figure 22: demonstration of the efficiency of the CEST effect when the exchangeable sites are either close to water compared to others further away, but with equal exchange rates and pool sizes. In light blue an Amide group with 30Hz exchange rate and resonance frequency at 3.5ppm (solid line) compared to the same at a resonance frequency of 50ppm (dashed line). Similarly, in pink, an Amine group with 400Hz exchange rate and resonance frequency at 2ppm (solid line) compared to the same at a resonance frequency of 50ppm.

Pool No.	Frequency [ppm]	Pool size (ratio to water)	T_1 [ms]	T2 [ms]
1 (Water)	0	1	1700	37
2 (Amine)	2 & 50	0.0036	1000	10
3 (Amide)	3.5 & 50	0.0036	1000	10
4 (Aliphatic)	-3.5	0.04	260	0.3

Table 3: Summary of the parameters for the four pool Bloch McConnell model used to produce figure 22.

For the Amide group (in light blue) while the maximum CEST effect is observed with the application of 0.9μT pulse at 3.5ppm, it shifts to 1.3μT at 50ppm. For the Amine group (in pink) the change is more significant; for maximum CEST effect at 2ppm the required amplitude is 2μT, while at 50ppm it shifts to more than 5μT. This is to highlight that one must be aware of analysis close to the water frequency. The 'optimum' saturation power due to the exchange for each site cannot be directly calculated from equation 20 in this case; qualitative analysis is more appropriate in determining the best saturation scheme.

The negative asymmetry of the Amide group is due to the Aliphatic peak resonating at -3.5pp from water. The model was chosen to be as realistic as possible to the in-vivo profiles, therefore the fourth pool was dedicated to the contributions in the

aliphatic side. Figure 23 shows the Z-Spectra from the four-pool model for different saturation powers.

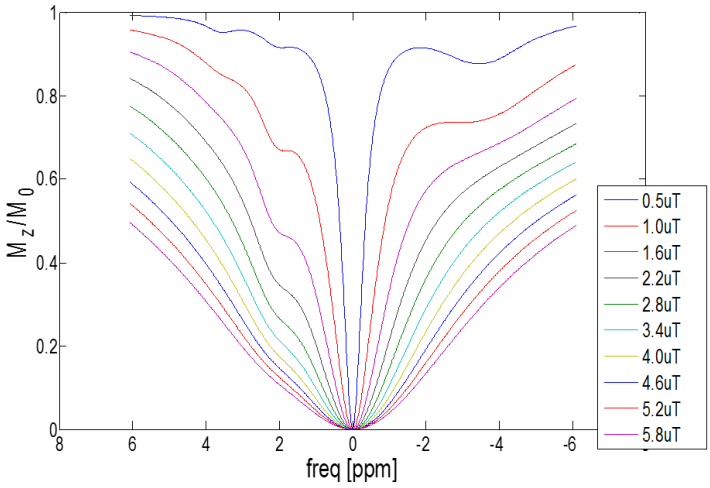

Figure 23: illustration of Z-spectra from the four-pool Bloch McConnell model with different saturation power (given in colours as seen in the figure).

In choosing the correct saturation scheme one must take into account the exchangeable protons to target in terms of their exchange rates and chemical shift from water. In addition, for clinical applications SAR limitations must be taken into account. There is a wide choice in achieving saturation and there are no current standardised ways to do so. This brings another factor into discussion, the comparison of data between sites. When the saturation schemes differ it is hard to compare data and deduce any physiological conclusions from them. It is crucial to understand that while this flexibility is favourable to research, data comparison from different groups is difficult and one must always take that into account.

Other than saturation, different readouts will also impact the CEST contrast. The next section focuses on signal readout and how to achieve maximum contrast.

3.1.3. The Readout part of a CEST acquisition

In principle, signal readout should immediately follow saturation to achieve the maximum CEST contrast possible. Ideally all k-space lines should be equally saturated prior readout; however, this approach would require a long acquisition. For example, if the matrix size was 64x64 and saturation/readout was 5s for 31 offset points, 2 hours 45 minutes would be required (64x5x31/60). Such acquisition time

would be non-practical in the clinic. Nonetheless, several groups have explored alternative imaging sequences, giving similar CEST contrast with accelerated temporal resolution.

The aim is to achieve maximum saturation by the time the centre of K-space[15] [65, 75] is acquired. This is because the centre of K-space contains the main information regarding signal and contrast, while the edges of K-space hold information about image details and resolution. Therefore if a compromise is to be made regarding the K-space data, this would be to achieve maximum saturation when reading the central phase encoding (PE) lines. Figure 24 demonstrates how reconstruction of the K-space edges (top left) gives information about the fine details (top right), while reconstruction of the K-space centre (bottom left) gives information about the contrast of the image (bottom right).

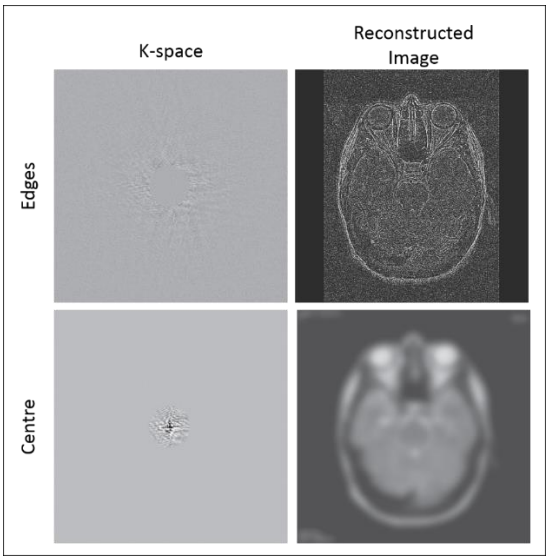

Figure 24: illustrating the image outcome when reconstructing only the edges of K-space (top images), compared to reconstruction of k-space centred only (bottom images). Image reproduced from McRobbie et al 2003 [65].

[15] The 'raw' data space before reconstruction. Data are stored in frequency domain.

Accordingly, two main ways are found to be useful to speed up the CEST acquisitions, as first reported by Liu et al 2009, [76].

(i) The *'pulse-acquire'* approach, uses saturation pulses prior to each PE step achieving therefore steady state by the centre of K-space [17]; ideally the data are acquired in inverse centric k-space order as shown in figure 25 (2nd figure).

(ii) The *'train of pulses-fast readout'* approach, where all saturation is applied prior to a fast readout, such as Echo Planar Imaging (EPI), [9, 11] or fast Gradient Echo (GE), [76, 30]. Ideally with this scheme the data are acquired in centric k-space order, as shown in figure 25 (3rd figure). With such ordering the signal acquired has strong CEST weighting during acquisition of the central k-space lines, which provide the main contrast in the MR images.

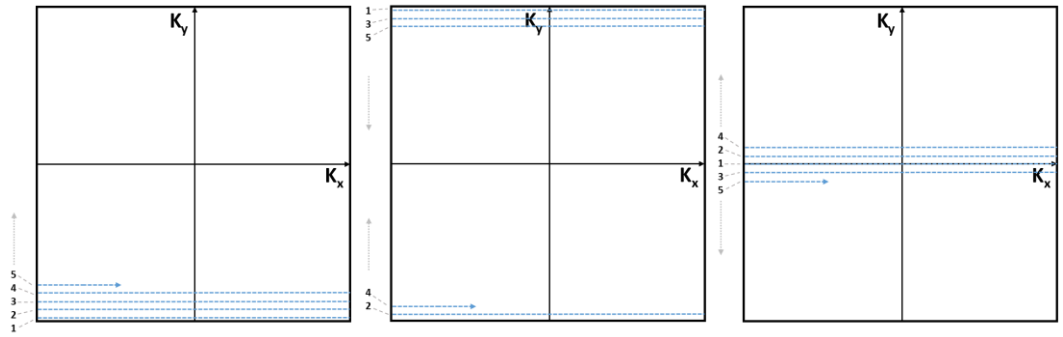

*Figure 25: Illustration of **linear** (image on the very left), **inverse central** (image in the centre) and **central** (image on the very right) k-space filling during MR data collection. Linear k-space ordering (the 'standard' in MRI, starts at one edge of k-space and fills all lines linearly until the opposite edge is reached. Reverse central ordering starts at one edge of the k-space and reaches the centre, alternating from one edge to the other. Central ordering starts at the centre of k-space and reaches the edges in an opposite manner to the inverse k-space ordering.*

3.2. CEST signal analysis

There is a lot of discussion among the community on how to interpret and provide quantitative assessment of the CEST data. As it is a relatively new technique there are no standardised protocols or post-processing methods that can be followed by everyone. Thus, it is not easy to keep consistency or compare results across sites. This section focuses on the ways to analyse the CEST data, including fitting, normalisation,

B_0 correction and signal interpretation. Processing tools such as Matlab or IDL are often used for the data processing. For the purpose of the work presented in this thesis, Matlab was used for all data processing. For the CEST images (Chapter 6) the analysis was performed pixel by pixel, while for the spectroscopic CEST (Chapter 5) the analysis was performed for single Z-spectra.

Data fitting

Ideally, CEST data should be fitted to a model (like the Bloch-McConnell model described in section 2.4), allowing the possibility of full quantification. Yet, due to the complexity of the in-vivo cases, using model-based analysis is still challenging. Typically, data are fitted to a smoothing spline (Matlab), which is often good enough to preserve the Z-spectrum shape (figure 26 for illustration).

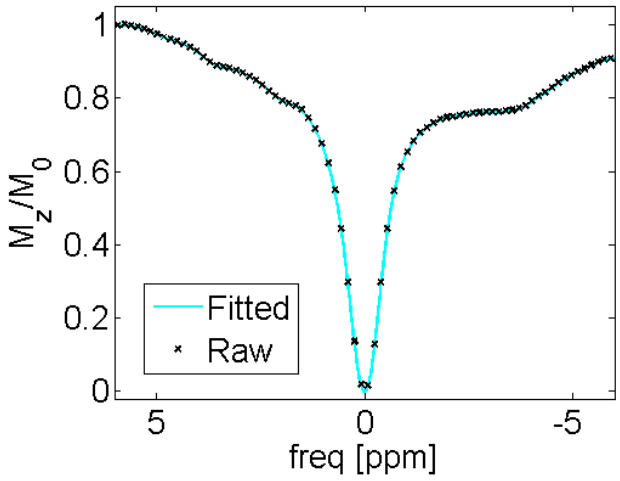

Figure 26: demonstration of CEST data set with raw data (in dotted black) fitted to a spline Matlab function (in light blue).

However if data are noisy due to physiological movements or low SNR other methods can be used to improve the shape. Such a method is described in section 5.1.2, developed for spinal cord data processing, based on weighted averaging of multiple acquisitions for physiological movement elimination.

B_0 correction

Once the data are fitted the next step is to correct for B_0 shifts, pixel by pixel. This is a crucial step of the analysis as the CEST experiments are frequency dependent; if the B_0 shifts are not corrected for, not all pixels in the image will correspond to the same

frequency offset. One way is to use the conventional B_0 maps produced by GE-phase maps [77], however they are acquired during a separate acquisition leading to slight variations of the absolute B_0 chemical shift. This is mainly because, especially during a clinical scan, power optimisation will occur between acquisitions, leading to slight variations of the Larmor frequency calculations. Additionally during the optimisation process, the RF is calibrated from the water signal corresponding to the entire field of view. Therefore, the calibration might not be centred in the field of interest (which is likely to be part of the field of view and not in the center). This will result in a correct map across the field of view but potentially centred with a small (few Hz) offset, still significantly large for a saturation experiment. Another way, proposed first by Kim et al 2009, is to use Water Saturation Shift Referencing (WASSR) maps. This method follows the same principle to a CEST acquisition but instead of a wide frequency range, offset pulses are applied close to water (±1ppm) with a weak saturation power (B_1=~0.1μT) and short length. This method assumes contrast is only attributed to the direct saturation effect of water, thus the water peak is used as reference per pixel. It also has the advantage of providing an absolute measure of the frequency shift, as opposed to GE-phase maps, which will be dependent on the scanner's determination of the water frequency. The WASSR method is mostly applied in low field MR scanners as the chemical shifts of exchangeable protons are closer to the water frequency (broader direct saturation profile) compared to higher field MR (>7T), [78]. Lastly, the Z-Spectrum itself can be used for B_0 correction if enough frequency offsets are acquired and the saturation power is low enough to give a sharp water peak (<2μT), [30]. In this way no additional sequences are required for correction and Z-spectra are effectively corrected to a B_0 map acquired at the same time as the rest of the CEST data.

Since the experiments in this thesis were conducted at a 9.4T MR scanner and at low powers (<2μT), the Z-Spectra were used for B_0 corrections pixel by pixel.

Normalisation

Normalisation of Z-Spectra is yet another non-standardised part of all CEST experiments. As discussed in the next section (Z-Spectra interpretation), a variety of normalisation factors has been used among research laboratories. In principle, normalisation does not change the shape of the Z-spectra, however the values deduced as 'CEST results' are heavily dependent on the normalisation factor used. Figure 27, demonstrates the same data set when normalised at 6ppm (in light blue) and normalised at 200ppm (in purple).

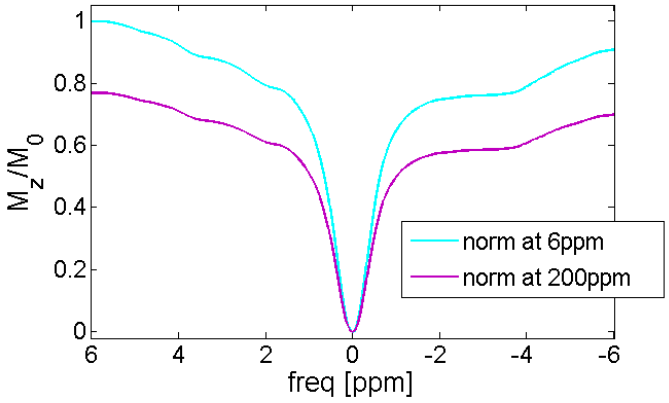

Figure 27: illustration of CEST data with two different normalisation factors. In light blue the Z-spectrum was normalised at +6ppm, while in purple the same Z-spectrum was normalised at +200ppm from water. Both spectra are only scaled differently and therefore present the same shape.

Z-Spectra interpretation

Numerous ways of analysing CEST data have been reported in the last decade across research sites depending on the application. An extensive review is published by Liu et al in 2013 [30] and also a summary is given below.

Earlier work in the field of MT used the magnetisation transfer ratio (MTR) for quantification purposes [79]; the equation defining this parameter is given below (21)

$$MTR = \frac{M_0 - M(+\Delta\omega)}{M_0} \qquad (21)$$

where M_0 is the signal of water when no saturation is applied and $M(+\Delta\omega)$ the signal of water when a saturation pulse of $\Delta\omega$ offset is applied.

The most common way to analysed CEST data is by MTR asymmetry (MTR_{asym}) given by equation 22, [67, 45].

$$MTR_{asym} = MTR(\Delta\omega) - MTR(-\Delta\omega) = \frac{M(-\Delta\omega)-M(+\Delta\omega)}{M_0} \qquad (22)$$

Another approach to CEST quantification is called CEST asymmetry ($CEST_{asym}$) and was reported by Cai et al [20]. Unlike to MTR_{asym} which uses M_0 for normalisation, $CEST_{asym}$ uses $M(-\Delta\omega)$. The mathematical description is given by equation 23 below

$$CEST_{asym} = \frac{M(-\Delta\omega)-M(+\Delta\omega)}{M(-\Delta\omega)} \qquad (23)$$

A third CEST quantification method, proposed by Zaiss et al, [69], uses the 'inverse metric spectrum', 1/Z. A new parameter was introduced, called Exchange-dependent Relaxation MT (MTR_{ex}), which was also demonstrated to correct for the direct saturation effects and any T_1 relaxation contribution. Equation 24 below gives a description of MTR_{ex}

$$MTR_{Rex} = \frac{1}{M(+\Delta\omega)} - \frac{1}{M(-\Delta\omega)} \qquad (24)$$

The three equations shown above (22, 23 and 24) all in principle eliminate direct saturation and MT effects, however they do not take into account the contributions from the aliphatic NOEs and fat resonating on the negative side of the Z-Spectra. Therefore, the values calculated will be affected by the aliphatic peak and fat.

Contaminations such as MT effects, contributions from the aliphatic peak as well as direct water saturation of the Z-Spectrum is a major issue in CEST quantification. Many ways have been developed by various research groups aiming to calculate the CEST signal with the least possible contribution from contaminated sources. A common way is the Lorentzian fitting approach [80], where a Lorentzian line shape is fitted to the Z-Spectrum and used as the reference. The CEST value is given by the difference between the Lorentzian fit and the Z-Spectrum at the specific frequency range of interest. This approach follows the idea in figure 19 where the Lorentzian shape gives the signal of water in the absence of any exchange processes. While there is no need for asymmetric analysis with this method, the calculated CEST value is still contaminated by the presence of MT.

Another method, named APTpeak (APTp), was implemented and used (see Chapter 6 for application of APTp) as part of this PhD thesis, [61]. However, the method was also reported by Zaiss et al 2013, [69] with the name APT*. As shown in figure 28, a straight or curved line is interpolated around the peak of interest; the case of Amides (3.5ppm) is illustrated in the figure, where the interpolation is applied between 3.0-3.1ppm and 3.9-4.0ppm. The APTp/APT* value is defined as the height of the peak (difference) between the interpolation line (in red) and the Z-Spectrum (in blue) at 3.5ppm.

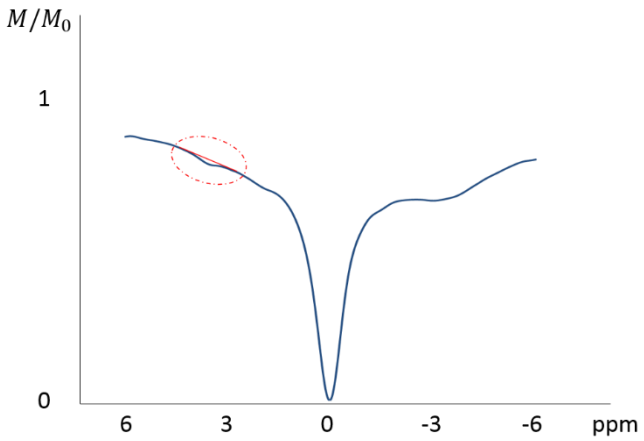

Figure 28: shows an example Z-Spectrum (in blue) with a fitted straight line (in red) around the Amide peak centred at 3.5ppm. The APTp or APT measure is calculated by the height from the red line to the Z-spectrum at 3.5ppm.*

Similarly to the Lorentzian fit method, the APTp/APT* does not require asymmetric analysis, meaning that no contributions from the negative side of the Z-spectrum (aliphatic) can alter the signal and furthermore is excludes any MT contaminations. However one of the weak points of the Lorentzian fit or the APT* methods, is the use of artificial line shape fitting which, if the data are noisy, will introduce additional variability to the quantification of the CEST effect.

Additionally, there is always the option to use the Z-spectra at the frequency range of interest, normalised to a far frequency offset. However, this method is only suitable for data comparison of the same scanning parameters and for the same group of subjects. The values calculated with this approach are the least suitable for further comparisons with other groups or other protocols compared to the rest of the interpretations described within this section. This is due to the fact that it offers no direct saturation or MT corrections, which results in the Z-Spectra having a higher

dependency on saturation power compared to other techniques (see equations 22, 23 and 24). Nonetheless, the signal is not contaminated by contributions which occur on the negative site of the Z-Spectrum, such as the aliphatic peak and fat.

Lastly, it is worth mentioning two other ways of analysing the Z-Spectra, quite similar in comparison. The first method, reported by Desmond et al [60] uses decomposition in the frequency domain (Z-Spectrum) to separate contributions from different exchangeable sites and also MT. The other method by Yadav et al [81], uses the deconvolution principle but in the time domain instead.

Both methods have successfully demonstrated the decomposition of the CEST signal, however they require inputs such as the frequency offsets which might not always be obvious from the Z-Spectra due to low concentrations or multiple sites with resonance frequencies in very close ranges.

Chapter 4. Phantom work

4.1. Introduction

It is known that CEST effects are directly linked to many factors, including the concentration of exchangeable sites, the sample pH, temperature, T_1 and T_2 relaxation times as well as the B_1 power used for the experiment. Therefore, investigation of the CEST effects where all the above parameters are controlled is crucial for our broader understanding of the effect. How does the Z-Spectrum shape change under different physiological conditions and how is that related to the 'quantitative' values that one can obtain by fitting the data to the theoretical model? By only looking at the theoretical results obtained from the Bloch- McConnell's model (see section 2.2), it would be easy to be misled by the simplicity of the model and ignore issues that appear when the complexity of the system is higher. Bovine Serum Albumin was therefore chosen as a model protein for this study as it is a long chained, complex protein which resembles in-vivo observations [82].

This chapter studies the known confounding CEST factors such as pH, temperature and concentration with the additional investigation of the saturation powers used. It breaks down each factor and explores the effects as individually as possible.

4.2. Experimental setup

4.2.1. Phantom Preparation

Phantoms with Bovine Serum Albumin (BSA) were prepared at four different concentrations (2.5, 5, 7.5 and 10 percentage of grams per volume of solution). For each concentration four phantoms where made with pH values ranging from to 7.3 in steps of 0.3 down to 6.4 (i.e: 7.3, 7.0, 6.7, 6.4). Phosphate buffered saline (PBS) was used at a concentration of 0.3 percent in distilled water for all the phantoms. The pH was measured using a micro pH probe (Mettler-Toledo International, Inc) and adjusted where necessary with the use of Sodium hydroxide (NaOH) and

Hydrochloric acid (HCl). All phantoms were prepared and scanned within the same day to avoid potential pH drifts. Phantoms did not go through a degasing process, but the solutions were carefully treated and phantom containers were filled avoiding air bubbles. Syringes of 1ml volume capacity were used as phantom containers, sealed with silicone glue. All phantoms were grouped in sets of four (same concentration, and four different pH values). Figure 29 illustrates the arrangement of a set of phantoms where all four have the same concentration but different pH values (7.3, 7.0, 6.7 and 6.4 clockwise starting from the top).

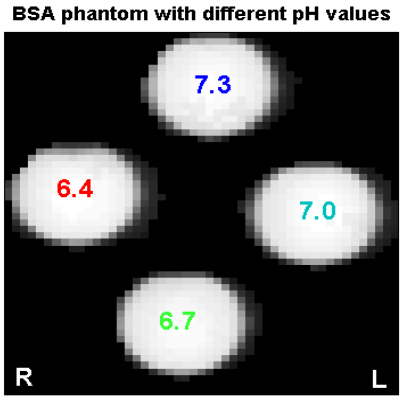

Figure 29: Image of a set of BSA phantoms with concentration of 5 percent (Radiological convention) indicating the location for different pH values. R and L, Right and Left respectively, show the real location of the phantom within the MRI scanner.

4.2.2. Experimental protocols

The phantoms were scanned in a horizontal 9.4T MR scanner (Agilent Technologies) with a volume receive/transmit RF coil of internal diameter 33mm (Rapid Biomedical). Temperature was maintained at 38.5^{o} C (experiments were complimentary of Chapter 6; piglets were maintained at 38.5^{o} C) with a hot air system (Small Animal Imaging Instruments - SAII). Prior to any scanning each phantom was allowed 30 minutes for temperature stabilisation. The phantom set with BSA concentrations of 10% was also scanned at temperature (T=35.5^{o} C) for investigation of the temperature dependence of the CEST effect.

All phantoms were manually shimmed achieving an overall linewidth of 15±3 Hz (0.038±0.008 ppm). T_1 and T_2 maps where acquired in addition to the CEST

acquisitions. Sequence description and parameters per acquisition are given in the following sections.

Reproducibility of the CEST results was checked by rescanning the same phantom set (concentration of 5%) at a different location within RF coil. This was achieved by rotating the phantom 90 degrees counter clockwise, relative to the original scan and re-shimming to the same standards as described above. See figure 30 (a) for the original location and figure 30(b) for the positions after rotation. This enabled us to investigate whether within different locations of the RF coil the CEST outcome could be reproduced. The CEST protocol was acquired twice in each position.

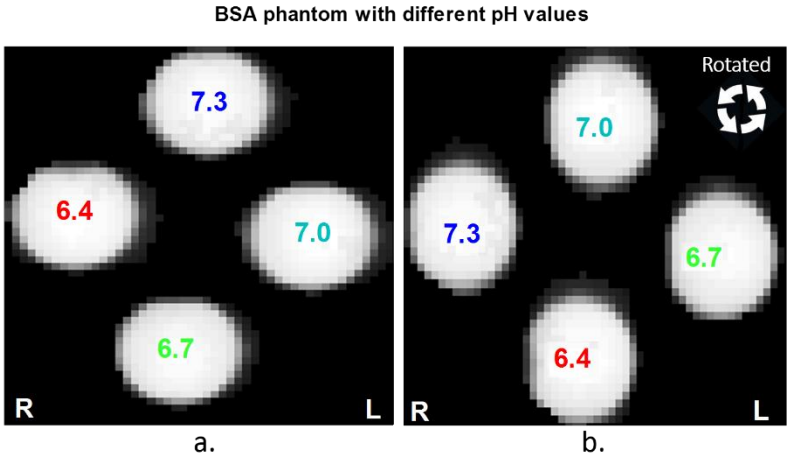

Figure 30: Anatomical image of a set of BSA phantoms with 5 percent concentration (Radiological convention) indicating the location for the different pH values when the phantom is rotated counter clockwise shown in (b). Comparison with the initial phantom locations in (a). R and L, Right and Left respectively, show the real location of the phantom within the MRI scanner.

4.2.2.1. T_1 map

Inversion Recovery Gradient Echo (GE) sequence was used to quantify the T_1 values of each phantom. A global adiabatic inversion pulse (flip angle 180°, duration 2ms) was applied at the frequency of water followed by an inversion time TI and a GE readout with echo time set at the minimum possible value (TE=1.09ms). Phase encoding during readout was chosen to be of centric order, i.e.: starting from the centre of k-space and continue filling lines outward in an alternative mode. With such ordering the signal acquired is heavily weighted to the central k-space lines, which gives the contrast in MR images. For illustration of centric k-space ordering refer to section 3.1.3 (Chapter 3 From theory to practice). The readout was succeded by a

crusher (2ms duration, 10G/cm) and a 15 seconds wait time to achieve full magnetization recovery before the next inversion pulse. Figure 31 shows the pulse sequence diagram which summarises the acquisition. The sequence was repeated 18 times with different TI values, exponentially spaced from 70 to 15000ms (denser spacing for the shorter TI values) . The entire set of values is summarized in table 4 below.

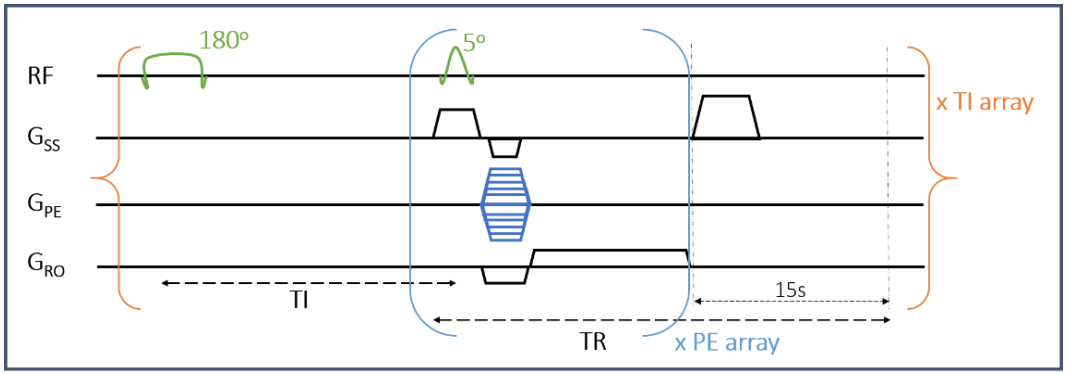

Figure 31: Illustration of the T1 map sequence. RF pulses are shown in green, slice select and frequency encoding gradients in black and phase encoding gradients in blue. The orange brackets indicate the array of 18 TI values. G_{SS}, G_{PE}, G_{RO} correspond to the slice selection, phase encoding and readout gradients respectively. TI corresponds to the wait time between the application of the inversion recovery and the readout pulses. All phase encoding lines were acquired following a single excitation pulse starting from the centre of k-space and continue in an interleave way to the edges. TE was set to 1.09ms (minimum possible) and TR_{RO}=2.03ms (referring to readout TR). Following the signal readout a 15 seconds delay was added which also included a spoiler gradient (duration = 1.3s and amplitude = 2G/cm).

Other parameters such as the field of view (FOV= 20x20mm^2), matrix size (64x64), number of slices (ns=1) and slice thickness (th=4mm), where kept the same during all the phantom work.

NUMBER	1	2	3	4	5	6	7	8	9
TI (ms)	70	97	134	185	257	355	491	680	940
NUMBER	10	11	12	13	14	15	16	17	18
TI (ms)	1300	1800	2500	3400	4800	6600	8000	11000	15000

Table 4: Summarises all the TI values used for the quantification of the T1 maps of all BSA phantoms. Values are given in ms.

Quantification of T_1 maps

Magnitude images were read into Matlab for the quantification of T_1 values for each phantom. Assuming mono-exponential decay for the longitudinal relaxation, equation 7 was used to fit the magnitude data with initial condition of $M^0_z = -M^{eq}_z$ and $M_z = |M_z|$.

$$M_z(TI) = M_z^{eq}\left|1 - 2e^{-TI/T_1}\right| \quad (25)$$

where, as already defined in section 2.1.4 (*Relaxation Processes*) M^{eq}_z is the net magnetisation along the z axis when the system is at thermal equilibrium, M^0_z the initial net magnetisation and T_1 the longitudinal relaxation time constant. As the magnitude data are always positive the relationship used for fitting, given by equation 25, displays only the absolute values of equation 7.

The analysis was performed pixel by pixel fitting equation 25 for M^{eq}_z and T_1 values. Assuming phantom homogeneity, all pixels were averaged to give a mean T_1 value and the standard error of the mean per phantom

4.2.2.2. T_2 map

For the quantification of T_2 maps the Carr Purcell Meiboom Gill (CPMG) sequence was used. It consisted of a 90 degree excitation pulse in the x axis (of sinc shape and duration = 1ms) followed by 40 refocusing pulses in the y axis (flip angle 180 degrees, Sinc shape and duration 1ms). Figure 32 is an illustration of the CPMG sequence used for T_2 mapping and also table 5 gives a complete summary of the echo time range used. FOV, matrix size, slice thickness and number of slices (ns=1) were kept the same as for T_1 mapping.

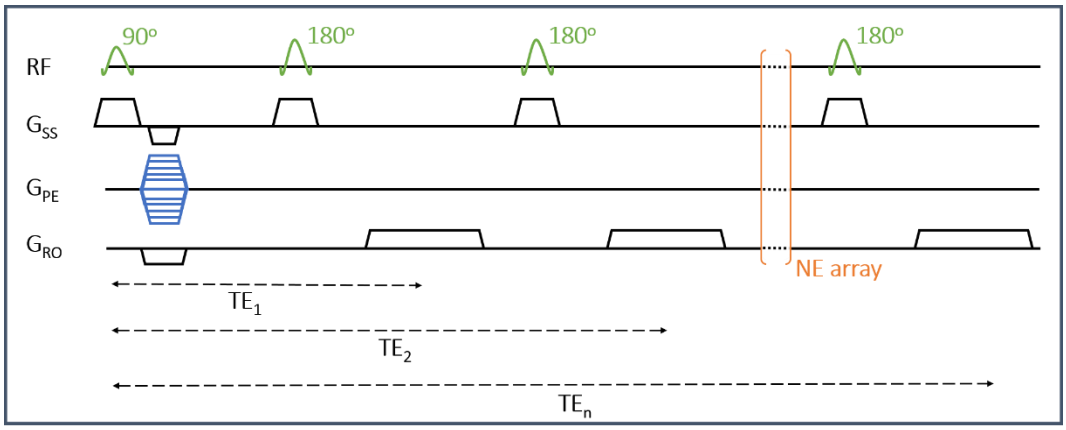

Figure 32: Illustration of the CPMG sequence used for the quantification of T_2 maps. As also in figure 31, the RF pulses are shown in green, the gradients in black and the phase encode table in blue. Orange colour represents the array of echo times (NE=40), where each echo corresponds to a different T2 weighted image. Slice refocusing crushers were applied for 2ms at amplitude 10G/cm.

Due to imperfections in the refocusing pulses, odd numbered echoes give signal at a slightly lower level compared to the even ones (for the even ones the imperfection artefact is cancelled out). Therefore out of 40 images collected (weighed with different TE), only the even ones were taken for the analysis [65]. See figure 33 for an example of the T_2 profile, taken from BSA phantom of 7.5% concentration at pH 7.3, which shows the odd numbered echoes in orange and the even ones in blue.

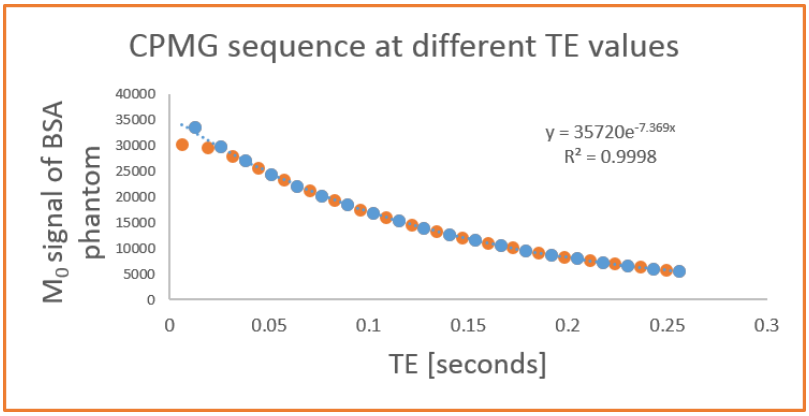

Figure 33: Shows the average M_0 value with different echo times of a BSA phantom (Concentration 7.5% and at pH 7.3), chosen for demonstration. In orange: The signal due to odd echoes. In blue: The signal due to even echoes. It is clear that the primary echo results in lower signal due to the slice profile.

NUMBER	1	2	3	4	5	6	7	8	9	10
TE (ms)	12.78	25.57	38.52	51.14	63.92	76.70	89.49	102.27	115.06	127.84
NUMBER	11	12	13	14	15	16	17	18	19	20
TE (ms)	140.62	153.41	166.19	178.98	191.76	204.5	217.3	230.1	242.9	255.7

Table 5: Shows a summary of all the echo times used for the quantification of the T2 maps of BSA phantoms. Values are given in ms.

Quantification of T_2 maps

Quantification of the T_2 data was also performed in Matlab. As already stated in section 4.2.2.2 (T_2 map section), the M_0 signal due to the even echoes was used and fitted to equation 10 assuming mono-exponential signal decay. The analysis was done pixel by pixel. Similar to the quantification of T_1 values, phantom homogeneity was assumed; thus all pixels were averaged to give a single mean value and a standard error of the mean per phantom.

4.2.2.3. Chemical Exchange Saturation Transfer

The CEST sequence consisted of two parts, pre-saturation at a frequency offset (f_{sat}) and readout at the frequency of water (on resonance). Saturation was achieved with a train of 100 Gaussian shaped pulses, each at 50ms duration and with an inter-pulse delay of 5ms (95% duty cycle). The flip angle of the saturation pulses was altered for the investigation of the CEST profile at different saturation powers. Table 6 summarises the experiments done per phantom group regarding the CEST acquisitions.

FA (μT_{EQ})	2.5%	5%	7.5%	10%
259° (0.4)	Yes	Yes	Yes	Yes
424° (0.7)	Yes	Yes	Yes	Yes
540° (0.9)	Yes	Yes	Yes	Yes
635° (1.0)	Yes	Yes	Yes	Yes
718° (1.1)	Yes	Yes	Yes	Yes
793° (1.3)	Yes	---	---	---
863° (1.4)	Yes	---	---	---
923° (1.5)	Yes	---	---	---
982° (1.6)	Yes	---	---	---

Table 6: Summarises the CEST acquisitions per phantom set. The table gives values for the flip angle used as well as the equivalent B_1 amplitude in micro TESLA (μT). The phantom groups correspond to concentrations of 2.5, 5, 7.5 and 10% and each consist of 4 different phantoms with pH values 6.4, 6.7, 7 and 7.3. Five data sets were acquired per phantom group, with different saturation powers as shown in this table. Additionally, the phantom group of 2.5% BSA concentration was also explored with four extra saturation powers. Line indicates that no data were acquired for the specific saturation power. Also Appendix D for the B_1 equivalence calculations.

Saturation was followed by a GE readout at minimum echo time (TE=1.1ms), similar to the readout of the T_1 map sequence (see sections 3.1.3, 3.1.3 and 4.2.2.1). Prior to the readout, no inter-pulse delay was added in order to maximise the CEST contrast achieved. The sequence was repeated for 77 frequency offsets ranging between ±6.08 ppm centred at water with steps of 0.16 ppm (64 Hz at 9.4T). Frequencies were alternated from positive to negative to compensate for any potential B_0 field drifts, starting from +6.08ppm all the way to 0 ppm. For the CEST data, 1 slice was acquired of 4m thickness. See figure 34 for a schematic of the CEST sequence used.

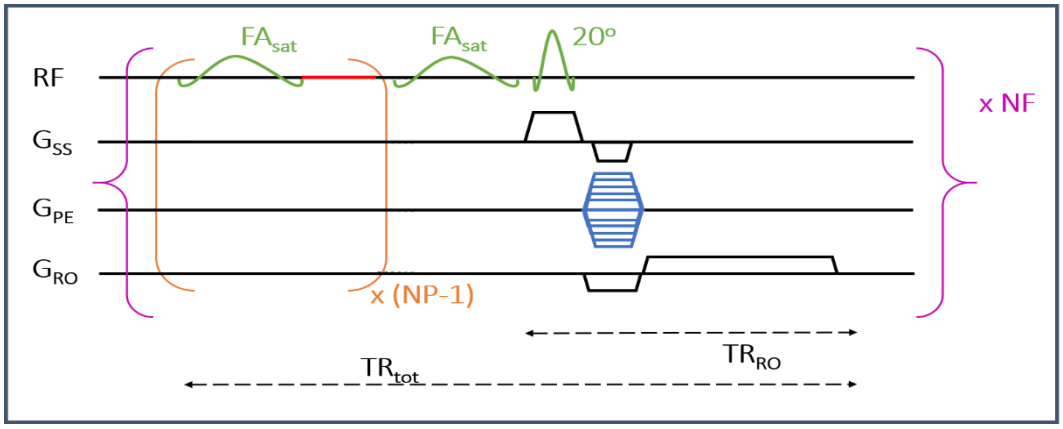

Figure 34: is an illustration of the CEST sequence used. All RF pulses are displayed in green. Slice select and frequency encoding gradients in black and phase encoding gradients in blue. Orange colour indicates the number of saturation pulses applied with an inter-pulse delay (in red) of 5ms. The saturation RF pulse prior to the excitation pulse is applied with no inter-pulse delay (total number of saturation pulses 100). FA_{sat} indicates the flip angle given in the table 6. TR_{RO} refers to the readout time alone, while TR_{tot} to the total time for the 1 frequency offset. Total number of frequency offsets (NF=77), displayed in purple.

CEST analysis

All analysis was done in Matlab. Each CEST acquisition consisted of 77 images (one for each frequency offset). All images were sorted from -6.08 ppm to 6.08 ppm and pixel by pixel fitting (smoothing spline function) was performed along the frequency direction. Data were interpolated to 1001 points which effectively increased the Z Spectra resolution from 0.16 to 0.012ppm. Following fitting, data were normalised to the average signal of all points between ± 5.5 and 6 ppm as no CEST contrast is expected across those frequency offsets. Figure 35 is a set of Z-Spectra showing the normalisation frequency points.

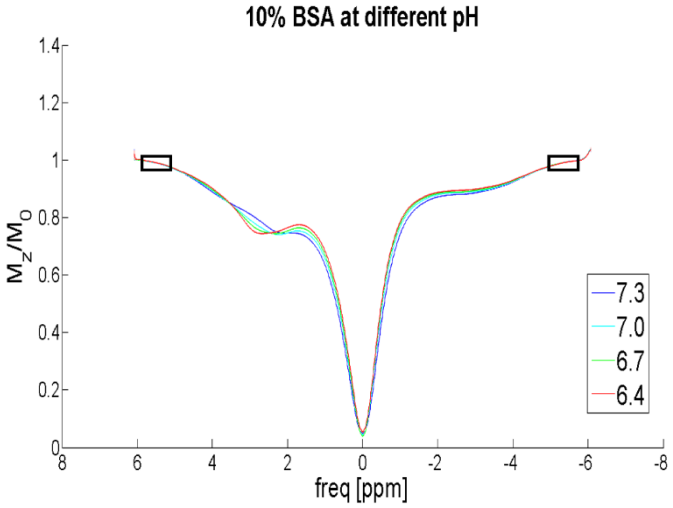

Figure 35: Shows four Z-Spectra which correspond to BSA phantoms of 10% in concentration. The pH of each phantom corresponds to different colour: 7.3 in blue, 7 in light blue, 6.7 in green and 6.4 in red. The two black boxes at the edge of the spectra indicate the values used for the normalisation of each data set. NB: The CEST data are usually presented with positive frequencies on the left and negative ones on the right. This is due to historical reasons as the first time CEST was explored, it was compared with conventional NMR spectroscopy.

All pixels per phantom were averaged (as also done in T_1 and T_2 mapping data) to give a mean value and the standard error of the mean. For the CEST analysis, asymmetry values (MTR_{asym}) and also absolute Z-Spectra values were calculated from different frequency ranges, corresponding to signals from amides, amines and aliphatic peaks. A few of the ranges included 1.2-1.6ppm, 2.5-3 ppm, 3.9-4ppm as well as the value at 3.5ppm and -3.5ppm. In addition, a Lorentzian line-shape (see equation 19 in section 3.1.1) was fitted to the points of the Z-Spectra centred at 0 ppm (-0.5 to 0.5 ppm around the water peak) and the full width half maximum (FWHM) values were determined.

4.2.3. Statistical Analysis

All data sets were assessed for the normality of their distribution, by calculating their skewness and kurtosis values. Data sets with kurtosis less than nine and with absolute value of skewness less than two [83, 84], were considered normally distributed. Note that all data were found to be normal therefore no data were excluded from the analysis. Confidence levels (CL) of the 68th, 95th and 99th percentiles were calculated per data set taking into account all the pixels within each phantom, as shown in figure 36 below.

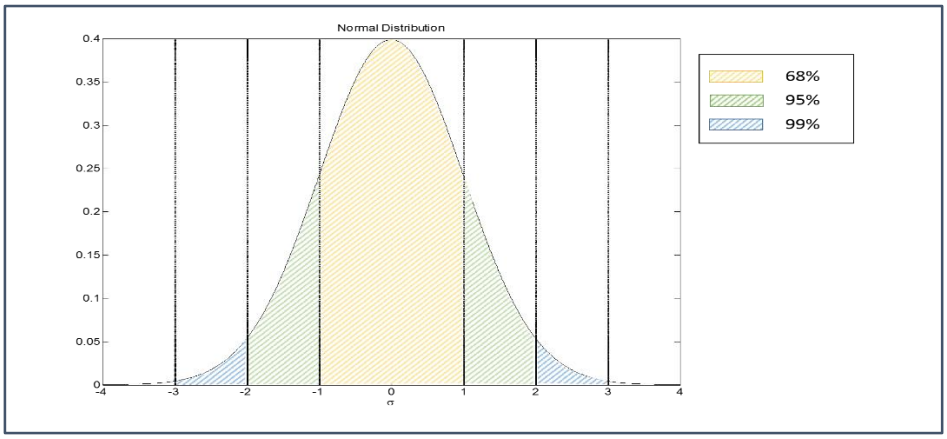

Figure 36: Demonstration of a normal distribution showing 68th (yellow), 95th (green) and 99th (blue) percentiles (2σ, 4σ and 6σ respectively).

Statistical significance between data sets was decided based on the percentage of data points overlap between them. A star annotation is used throughout the result section (4.3) to indicating whether data are statistically different or not. See table 7 below for a summary of the annotation and also figure 37 for examples on each case taken from the phantom study.

Annotation	**Level of Significance**	**Confidence Levels (CL)**	**P-value equivalence**
(***)	High	>99%	< 0.01
(**)	Standard	>95% & <99%	< 0.05
(*)	Low	>68% & <95%	< 0.3
(-)	None	<68%	> 0.3

Table 7: Summarises the star annotation used throughout the results section (4.3). The confidence level column indicates the percentage of different data between two sets.

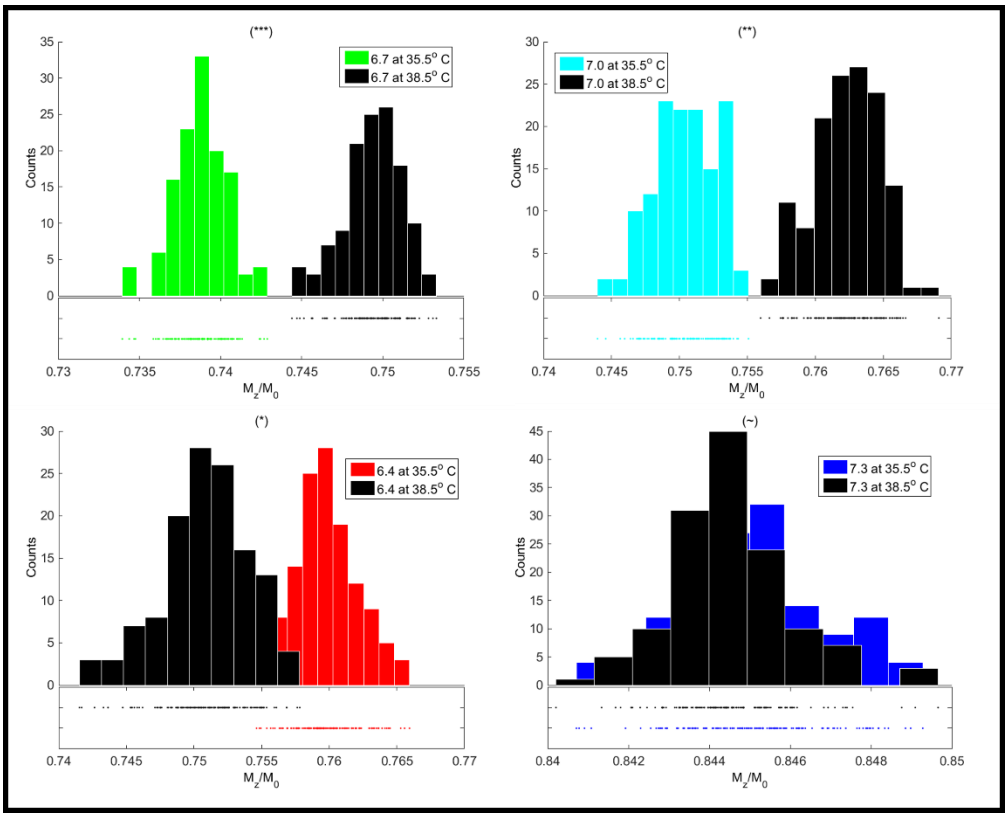

Figure 37: includes four different sets of data where statistical analysis was performed. Each figure uses two types of data presentation, the standardised histograms and below each histogram the spread of all the points per set. ***Top left figure:*** *demonstration of high significant difference (***) between the two data sets (BSA phantoms at 10 % concentration, both represent the Z-spectrum at 2.75ppm and pH value 6.7. In green the sample at 35.5° C and in black at 38.5° C).* ***Top right figure:*** *demonstration of standard significant difference (**) between the two data sets (BSA phantoms at 10 % concentration, both represent the Z-spectrum at 2.75ppm and pH value 7.0. In light blue the sample at 35.5° C and in black at 38.5° C).* ***Bottom left figure:*** *demonstration of low significant difference (*) between the two data sets (BSA phantoms at 10 % concentration, both represent the Z-spectrum at 1.4ppm and pH value 6.4. In red the sample at 35.5° C and in black at 38.5° C).* ***Bottom right figure:*** *demonstration of no significant difference (~) between the two data sets (BSA phantoms at 10 % concentration, both represent the Z-spectrum at 3.5ppm and pH value 7.3. In blue the sample at 35.5° C and in black at 38.5° C).*

4.3. Results & Discussion

A representative selection of results from the BSA phantom study are presented here. These include data on rotated vs non rotated phantoms (spatial reproducibility section), data acquired at two different temperatures (temperature dependence section), with different pH values (pH dependence section), for different concentrations (concentration dependence section) as well as scanned with a range of saturation power (B_1 power dependence section).

Spatial reproducibility

Data comparison between rotated and non-rotated phantoms show no significant differences (CL < 0.68) for the CEST values (for box plots of the statistical analysis refer to following figures 39, 40, 41 and 42). See figure 38 for Z-Spectrum per pH value, where the rotated phantom data are overlapping the non-rotated ones. This suggests that the relative location of different phantoms within the RF coil does not compromise the CEST results, nor favour different locations. Therefore is fair to assume that any significant differences are related more to the parameters changed due to the experiments rather than the location of the phantoms in the RF coil.

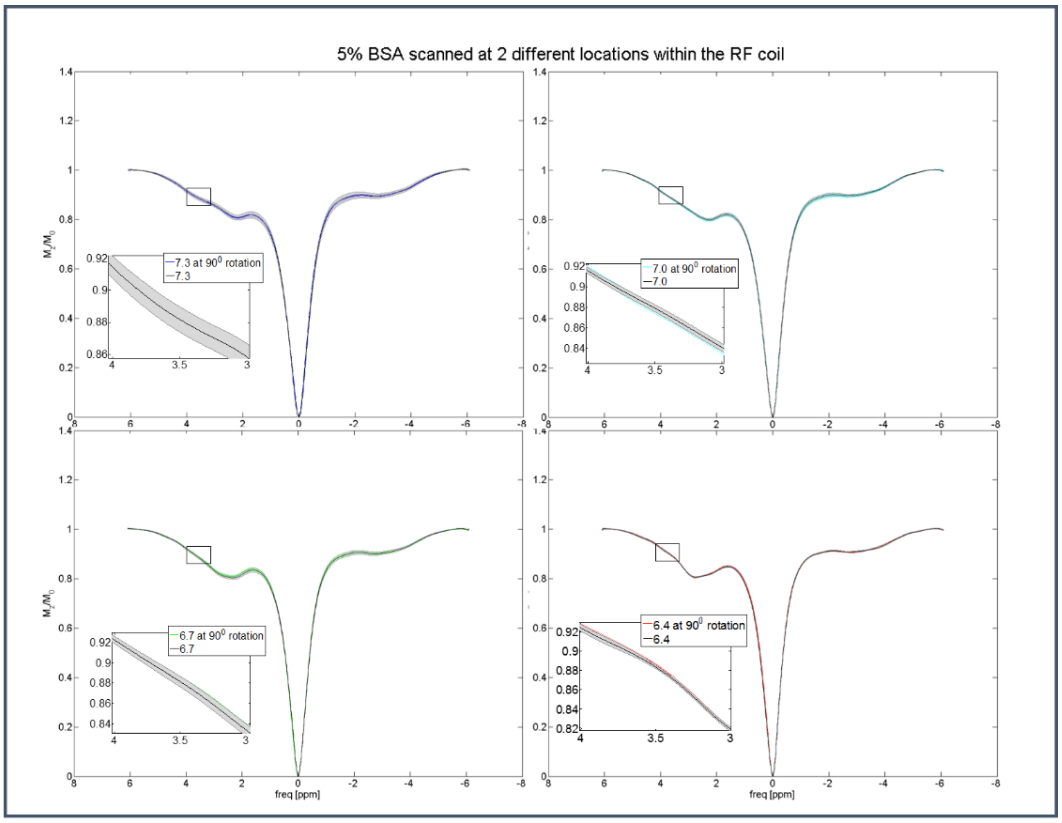

Figure 38: shows four Z-Spectra pairs. Each figure contains two Z-Spectra, from the same phantom, as figure 30 demonstrates (rotated and not rotated). All four phantoms have a concentration of 5%, scanned at 38.5° C and with a saturation power of 1.1 μT (B_1 power equivalent). pH values per phantom are 7.3, 7.0, 6.7 and 6.4 listed from top left figure clockwise. NB: the Z-Spectra are plot as the average of all the values per pixel and standard errors are also plotted on each side of the mean. See zoomed version (between 3 to 4 ppm, centred at 3.5ppm) of each figure for better resolution. It applies similarly for the entire frequency spectra.

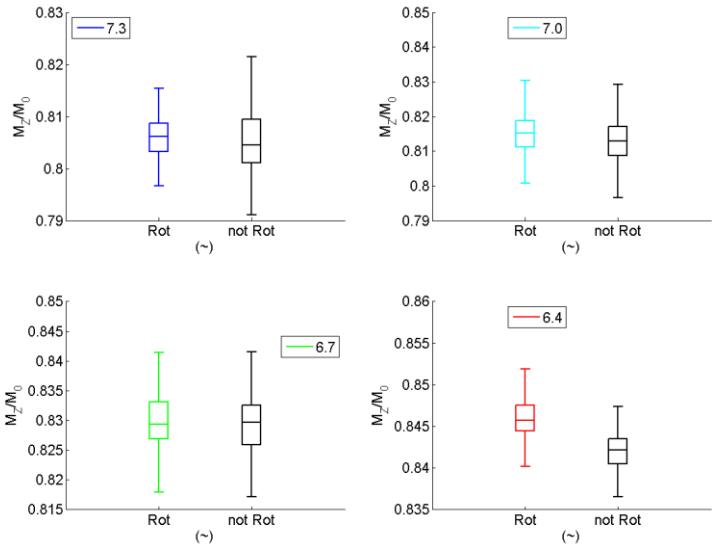

Figure 39: Shows the CEST values at 1.4ppm from water for each of the 4 pH values and for both rotated (coloured depending on the pH value) versus non-rotated (coloured black) phantoms. No significant difference (CL>0.68) is observed for all the phantoms. Note that the level of significance is noted in the star annotation as explained in section 4.2.3.

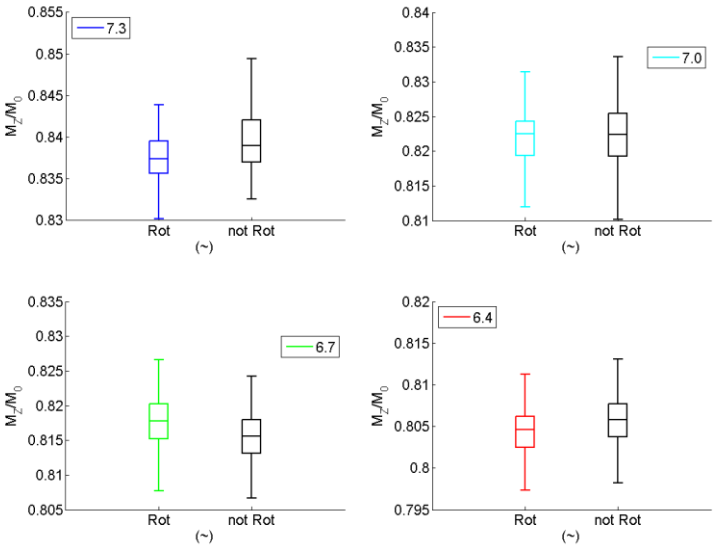

Figure 40: Shows the CEST values at 2.75ppm from water for each of the 4 pH values and for both rotated (coloured depending on the pH value) versus non-rotated (coloured black) phantoms. No significant difference (CL>0.68) is observed for all the phantoms. Note that the level of significance is noted in the star annotation as explained in section 4.2.3.

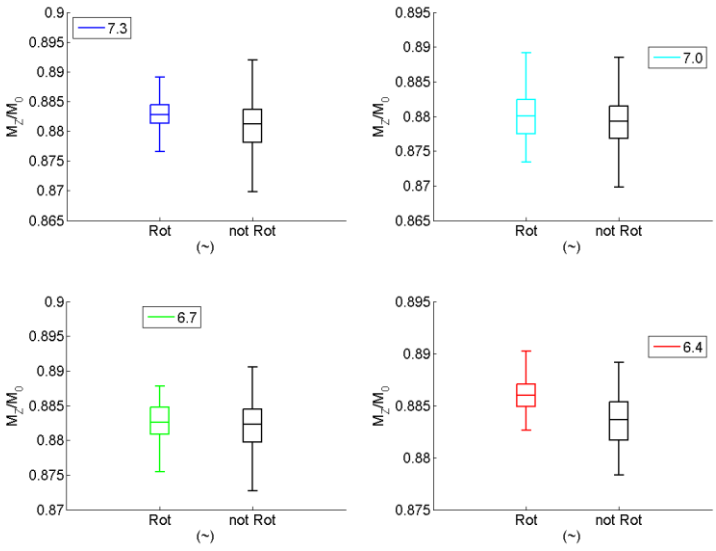

Figure 41: Shows the CEST values at 3.5ppm from water for each of the 4 pH values and for both rotated (coloured depending on the pH value) versus non-rotated (coloured black) phantoms. No significant difference (CL>0.68) is observed for all the phantoms. Note that the level of significance is noted in the star annotation as explained in section 4.2.3.

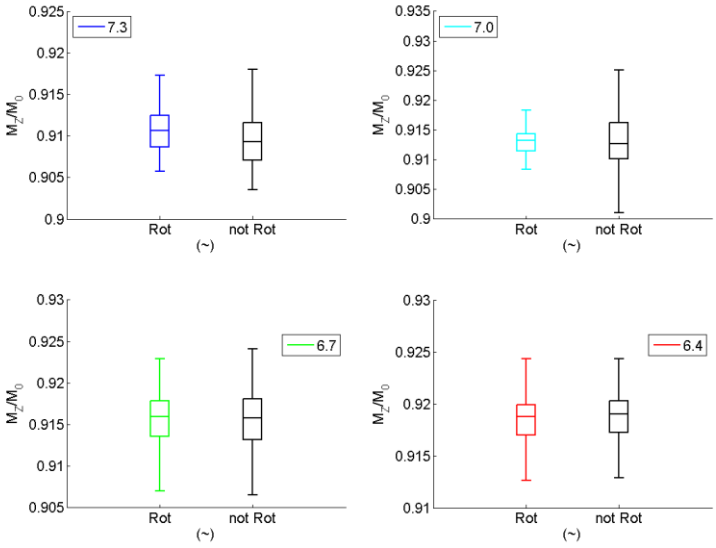

Figure 42: Shows the CEST values at -3.5ppm from water for each of the 4 pH values and for both rotated (coloured depending on the pH value) versus non-rotated (coloured black) phantoms. No significant difference (CL>0.68) is observed for all the phantoms. Note that the level of significance is noted in the star annotation as explained in section 4.2.3.

Temperature dependence

Comparison of CEST data at 10% concentration scanned at different temperatures show significant differences within the range of 2.2ppm and up to 3.5ppm from water. There is a general increasing trend for the Z-Spectrum in that range when the phantoms are heated to 38.5°C compared to the CEST values at 35.5°C. Figure 43 shows the difference between temperatures for a set of phantoms with different pH values at 2.75ppm where all phantoms show statistical significance.

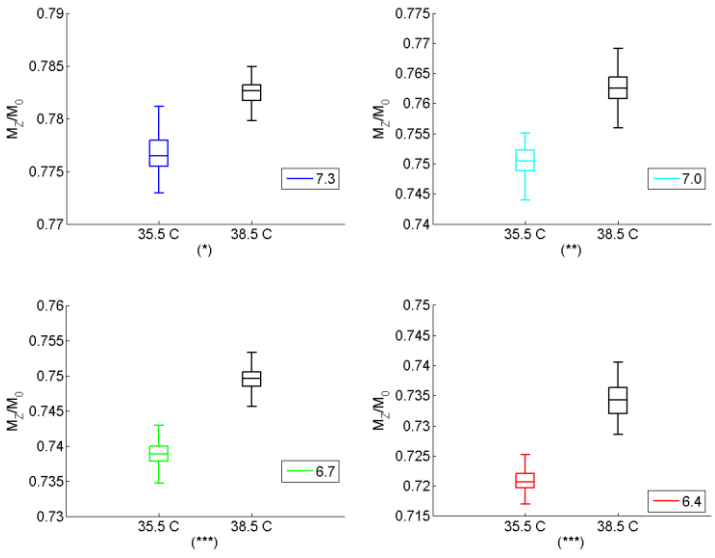

Figure 43: Shows the CEST values at 2.75ppm from water for each of the 4 pH values for a comparison of scanning at 35.5° C (coloured depending on the pH value) and 38.5° C (coloured black). Significant difference is observed to all four sets with high being for the lower pH value samples (6.7 and 6.4 respectively).The samples shown here were scanned after a saturation train of pulses with 1.1μT B_1 power equivalence. Note that the level of significance is noted in the star annotation as explained in section 4.2.3.

Figure 45 displays the Z-spectra of the four phantoms with different pH value. No significant difference is observed in the Aliphatic range (-2 to -4ppm) which suggests no temperature dependence (also see figure 44 which displays the CEST values at -3.5ppm from water, within the Aliphatic range). In fact, no other significance differences are observed other than within the range of 2.2 to 3.5ppm.

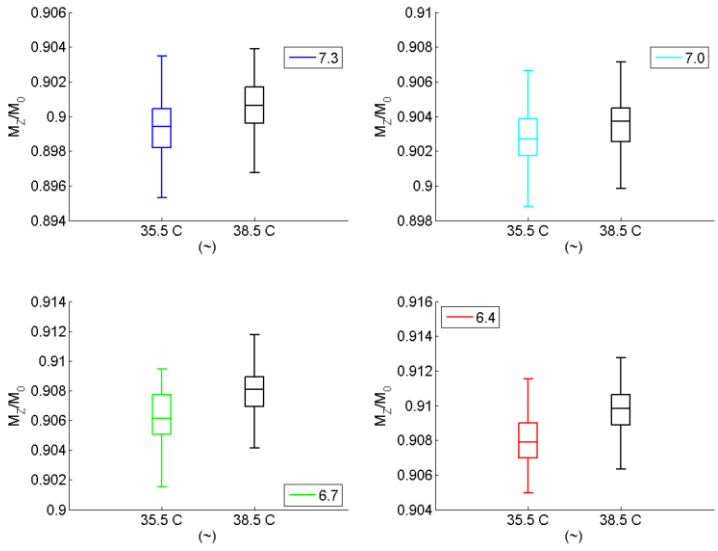

Figure 44:Shows the CEST values at -3.5ppm from water for each of the 4 pH values comparing samples scanned at 35.5° C (coloured depending on the pH value) and 38.5° C (coloured black), showing no significant differences. The samples shown here were scanned after a saturation train of pulses with 1.1μT B_1 power equivalence. Note that the level of significance is noted in the star annotation as explained in section 4.2.3.

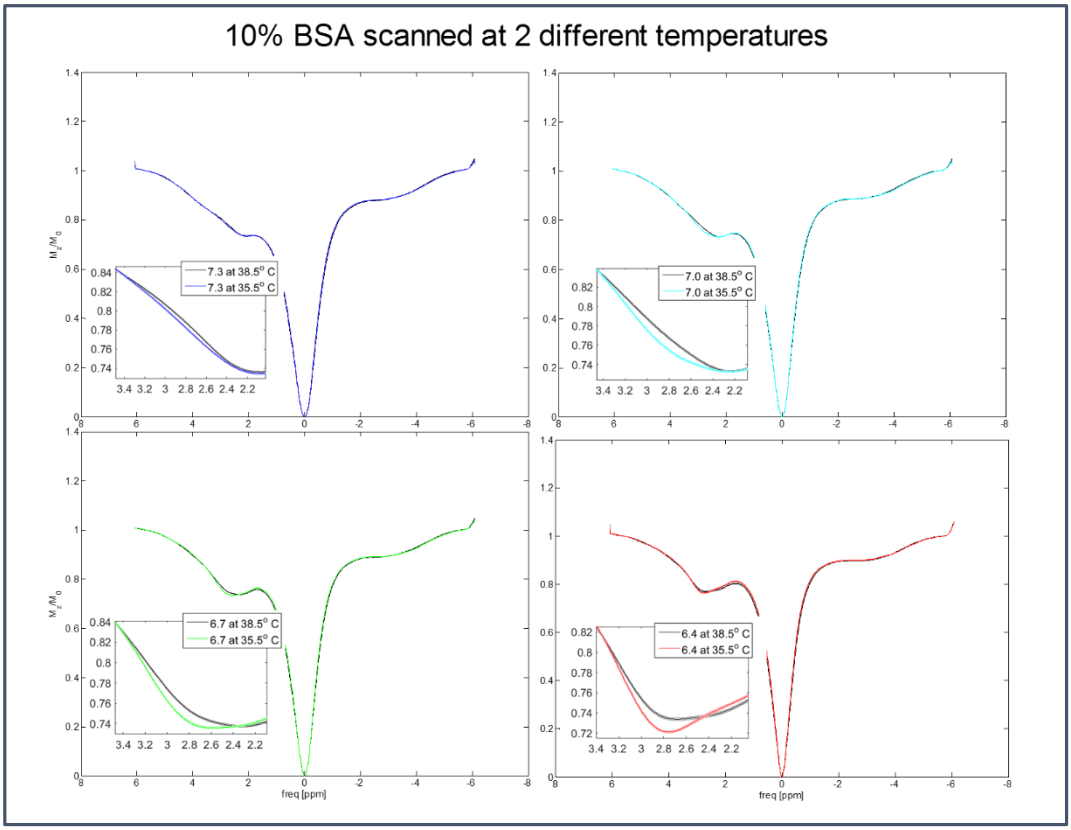

Figure 45: shows four Z-Spectra pairs. Each figure contains two Z-Spectra, from the same phantom, one with temperature maintained at 35.5°C (coloured depending on the pH per phantom) and the other one maintained at 38.5°C (coloured black). All four phantoms have a concentration of 10%, scanned with a saturation power of 1.1 μT (B_1 power equivalent). pH values per phantom are 7.3, 7.0, 6.7 and 6.4 listed from top left figure clockwise. NB: the Z-Spectra are plot as the average of all the values per pixel and standard errors are also plotted on each side of the mean. See zoomed version (between 2.2 to 3.5 ppm, centred at 2.65ppm) of each figure for better resolution on the region where significant differences are observed (figure 43 for level of significance) between spectra (the rest frequencies of the z-spectra are found with no significant differences when comparing temperature dependence).

Data acquired with different saturation powers (0.7, 0.9 and 1μT of B_1 power equivalent) were found to have the same trends as the data shown for 1.1 μT of power (figures 43, 44 and 45) but with CEST values at different absolute values. Figure 46 below summarizes the results from all four powers.

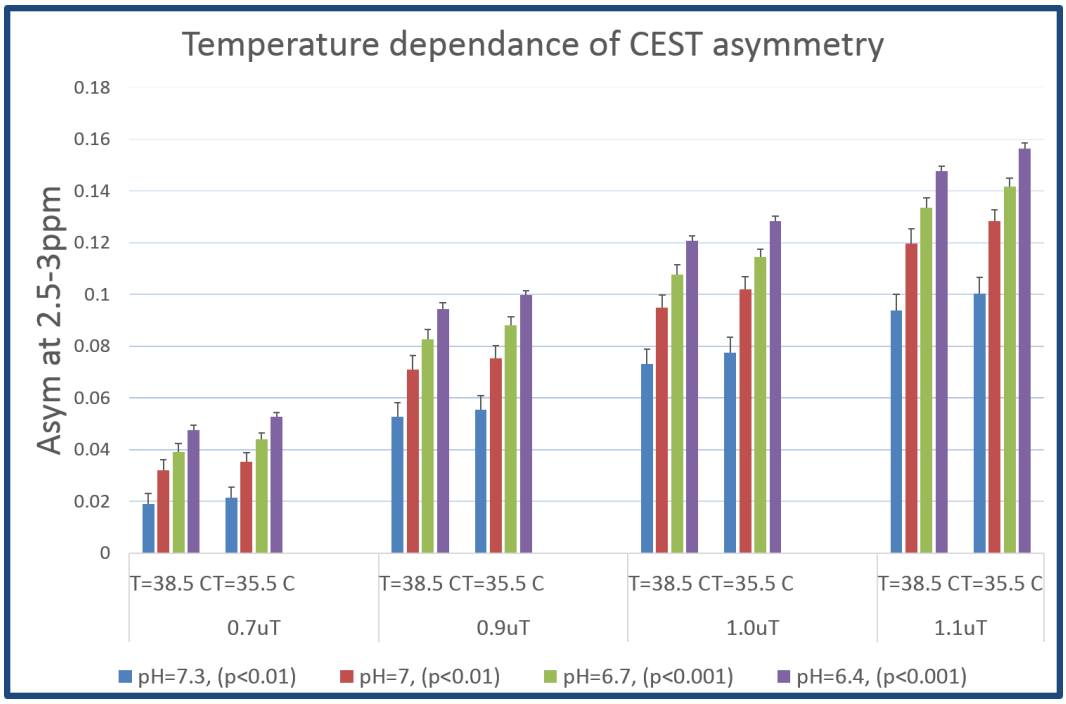

Figure 46: Shows the CEST asymmetry integrated between 2.5 and 3ppm (centred at 2.75ppm) for data acquired at 35.5°C and 38.5°C and with different saturation power each time (0.7, 0.9, 1.0 and 1.1 μT accordingly). Different pH values are given with different colours as figure indicates.

Concentration dependence

As expected from the theory (section 2.3), the CEST effect is dependent on the concentration. In general terms, the higher the concentration, the bigger the CEST effect observed. Figure 47 shows how the different concentrations of BSA affect the Z-Spectra while other parameters, such as pH, temperature or saturation power were not altered. At low concentrations the relationship is approximately linear, but when concentrations become larger, the shape is better described with a 2nd order polynomial [17]. From the Z-Spectra in figure 47, it can be also inferred that the aliphatic side is also concentration dependent due to the negative side of the Z-Spectra increasing with concentration as well.

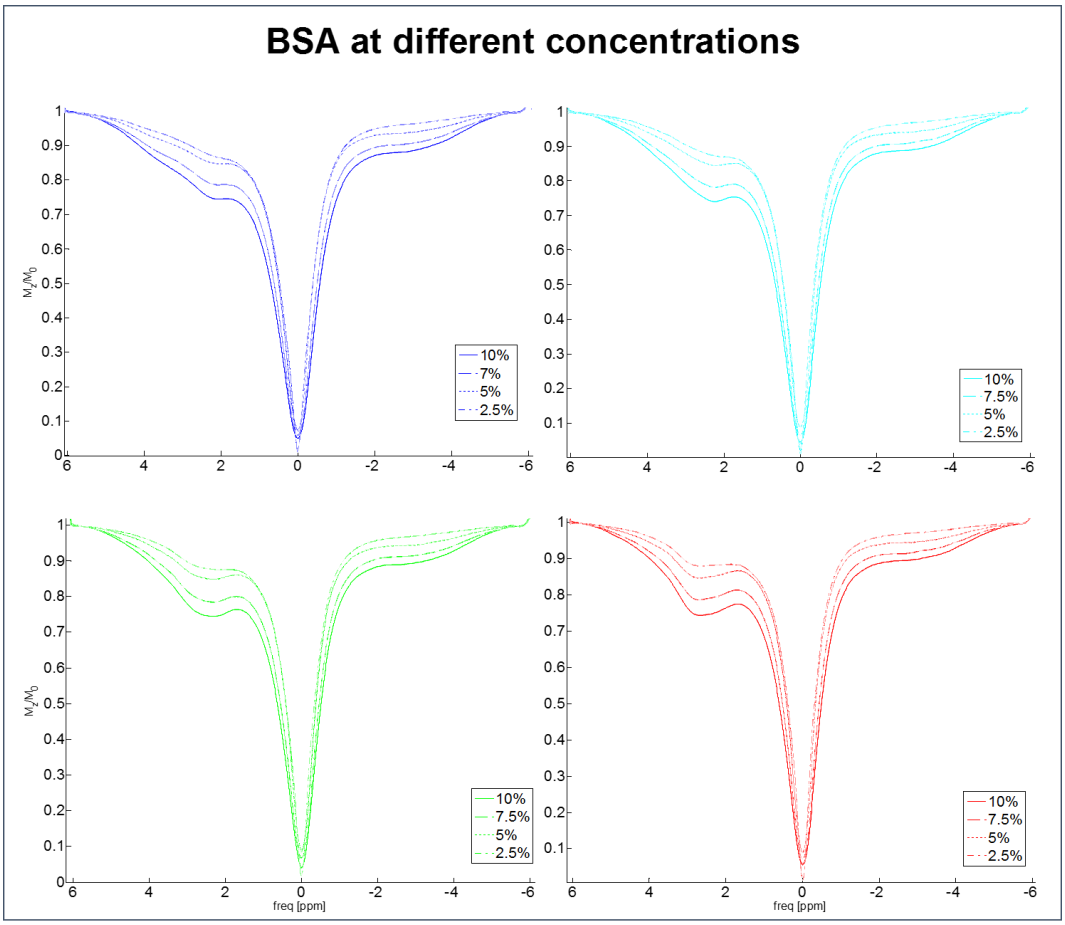

Figure 47: Shows four sets of Z-Spectra, each at a different pH value, indicated with different colours (dark blue for pH of 7.3, light blue for pH of 7.0, green for pH of 6.7 and red for pH of 6.4). Each set contains Z-spectra with different BSA concentration (solid line for10%, dashed line for 7.5%, dotted line for 5% and dashed-dotted line for the smallest concentration of 2.5%). Observe how the shape of each Z-spectrum does not change, but is shallower (driven by bigger CEST effect) when the BSA concentration increases. This is valid for both the aliphatic and the rest of the exchangeable sites. NB: the Z-Spectra are plot as the average of all the values per pixel and standard errors are also plotted on each side of the mean.

For demonstration, the saturation power used was 1.1μT, but similar trends apply to the rest of the saturation powers tested, including 0.4, 0.7 and 1 μT (see figure 48 for summary at all powers in the frequency range of 2.5 to 3ppm).

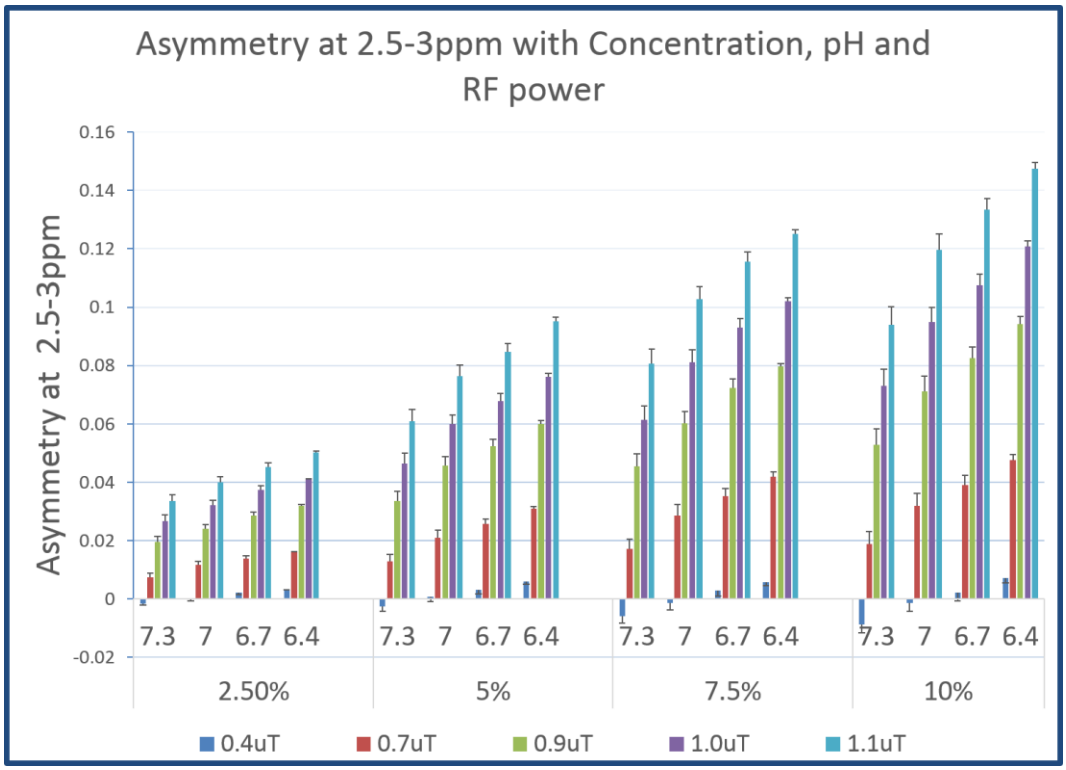

Figure 48: this is a summary showing the same samples scanned at different saturation powers (0.4, 0.7, 0.9, 1.0 and 1.1 μT). The figure contains four pH values for all four concentrations of BSA. Look how other than the very small power (0.4 μT) which was not sufficient saturation, the rest of the powers give the same trend regarding the concentration dependence of the BSA phantoms.

Figure 49 shows the tendency of the CEST signal with different BSA concentrations in the range of 2.5 to 3ppm (centred at 2.75ppm). Data with different pH values are presented including illustrative comparison of fitting curves for one of the data sets (pH 6.4 in red). The Bayesian Information Criterion[16] (BIC) [85] was used as a tool for deciding whether the data followed more a 2nd order polynomial than linear relationship. Three relationships were tested with the BCI approach: linear, 2nd order and 3rd order polynomial. The results revealed lower BIC values associated with the 2nd order polynomial with values {-13.37, -15.68 and -14.30} for 1st, 2nd and 3rd order polynomials respectively. Best fitting yields the lowest BIC, therefore the 2nd order polynomial was judged as the most appropriate for the data sets displayed in figure shown below.

[16] The BIC assessment gives a value to various known fitting curves in order to decide on the most appropriate number of parameters for the fitting curve of a data set.

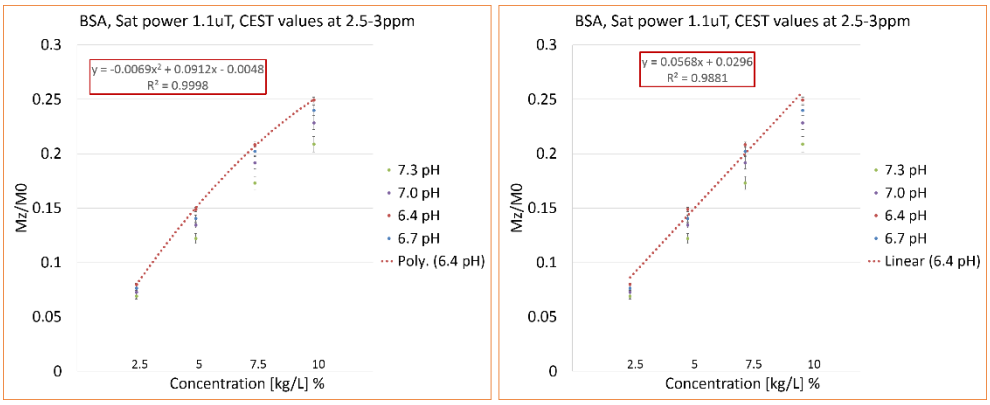

Figure 49: Both figures show the relationship of the CEST effect at the range of 2.5 to 3ppm (centred at 2.75ppm). Data with different pH values are presented at different colours (pH 7.3 in green, pH 7 in purple, pH 6.7 in blue and pH 6.4 in red). Right and Left images are identical in terms of data, but differ in the fitting type. Figure on the left shows data fitting with a 2nd order polynomial, while figure on the right shows data fitting to a linear relationship (illustrative fitting curves for one data set out four: pH 6.4). While the linear interpolation gives a fitting coefficient R^2 of -0.988, the 2nd order polynomial fitting appears improved with an R^2=0.999 goodness of fit (GOF). The relationship of the CEST effect with concentration can be approximated with a linear curve at low concentrations [17].

Note that relaxation values (T_1 and T_2) were not varied, therefore they do have an effect on the Z-Spectra. As the concentration of the samples increases, the T_1 and T_2 values of the samples were found to decrease (see figure 50 for the relationships of both relaxation times with different concentrations of BSA). This decrease in relaxation values is partly responsible for the symmetric broadening of the FWHM of Z-Spectra (at ~ ±1ppm centred at zero). In fact, FWHM was found to decrease with longer relaxation times. Figure 51 displays the relationship of FWHM with each of the relaxation times (T_2 and T_1 respectively).

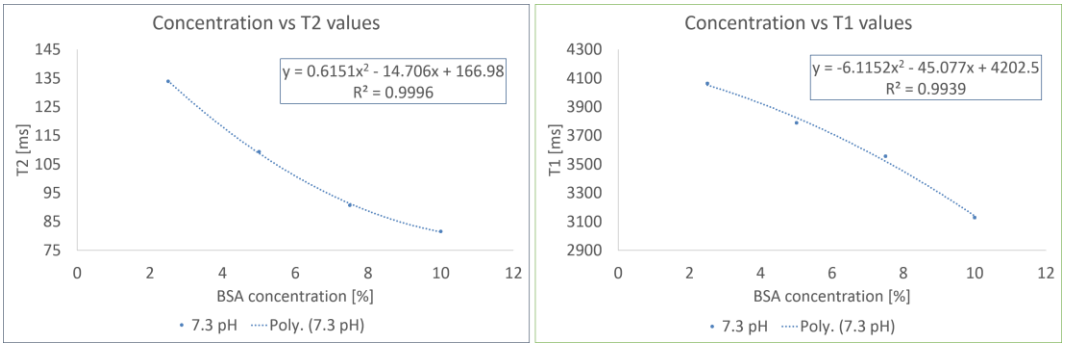

Figure 50: left figure shows the relationship of T_2 values with concentration of BSA and right figure the relationship of T_1 values with concentration of BSA. Both figures correspond to sample values of pH 7.3 and CEST was performed with saturation power of 1.1μT. In both cases there is a trend for higher relaxation values at lower concentrations.

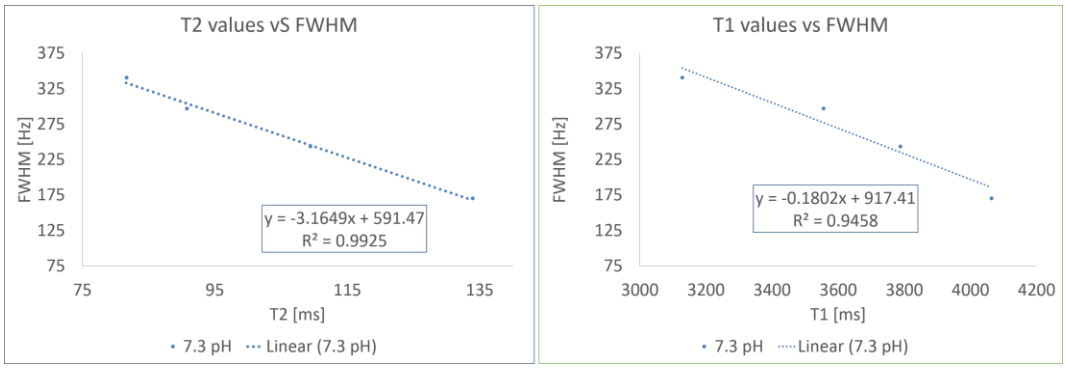

Figure 51: left figure shows the relationship of T_2 values with the Z-Spectra FWHM and right figure the relationship of T_1 values with the Z-Spectra FWHM. Both figures correspond to sample values of pH 7.3 and CEST was performed with saturation power of 1.1μT. In both cases there is a trend for lower FWHM values with increasing values of T_1 and T_2.

While the relationship of T_2 with the FWHM is expected due to the Lorentzian relationship which can be deduce from the Bloch-McConnell equations (equation 19), the relationship of T_1 with FWHM was surprising. To further investigate the effect of FWHM with T_1 and T_2 relaxation times the theoretical model was used. This allows an even more controlled experiment compared to the phantom work, where the BSA sample concentration as well as T_1 and T_2 values could be set as individual parameters. Figure 52 displays the relationship of FWHM to each relaxation time (T_2 on the left and T_1 on the right) from a five[17] pool model of the Bloch-McConnell equations. The parameters of the model were chosen to be as realistic as possible, based on the BSA phantom of 5% at pH value 7.3 (T_1=3500ms and T_2=100ms), which is also the pH value corresponding to the data presented in figure 51 above. Parameters concerning the CEST pools are listed in table 8.

[17] The number of pools used in the model was chosen according to the peaks observed in the Z-Spectra (figure 54).

Pool No.	Frequency [ppm]	Pool size (ratio to water)	Exchange rate [Hz]
1 (water)	0	1	0
2 (Amide)	2.2	0.0017	22
3 (Amine)	2.9	0.0025	400
4 (Amide)	3.6	0.0017	22
5 (Aliphatic)	-3.5	0.04	4.5

Table 8: Summarises the parameter details for all the pools used. The concentration of the exchangeable pool was considered as 5% of the water (ratio of the initial magnetisations M_0 available), at a pH value of 7.3. T_1 and T_2 were considered as 3500 and 100 ms respectively.

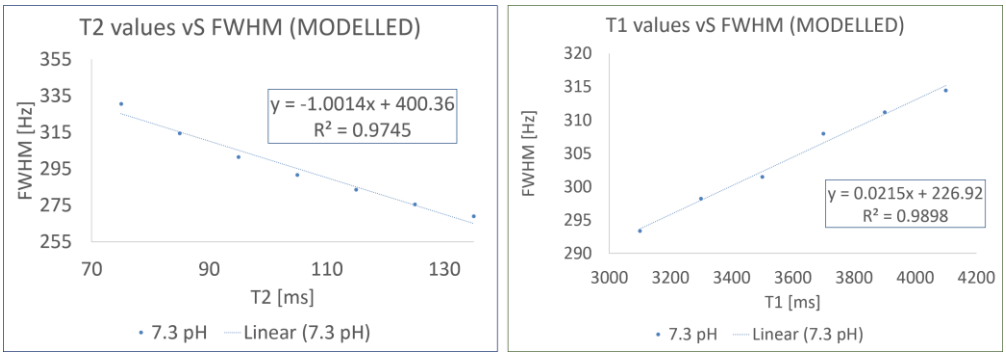

Figure 52: is an illustration of how the behaviour of FWHM is predicted from the Bloch-McConnell model with a range of T_1 (right image) and T_2 values (left image). FWHM was deduced from the Z-Spectra in the same way as for the experimental data (Lorentzian line-shape fitting of the water peak). The B_1 used was 1.1μT, the same as the experimental B_1.

From the comparison of figures 51 and 52 correlation coefficient graphs were created shown in figure 53. One can clearly see that FWHM compared to T_2 values between experimental and theoretical results follow similar trends (correlation factor of 0.31, $p<0.001$) whereas in the case of T_1 an inverse correlation is observed (correlation factor of -0.1, $p<0.001$). However, when looking at figure 53 (relationship on the right), it might be inferred that yet another (or many) factors affect the relationship, hence its slightly exponential shape. Therefore is more likely that the behaviour of T_1 compared to FWHM is mostly attributed to the difference in concentrations (see figure 50 compared to figure 51); not surprising as it is mentioned already that at least the sample's concentration affects the relaxation values.

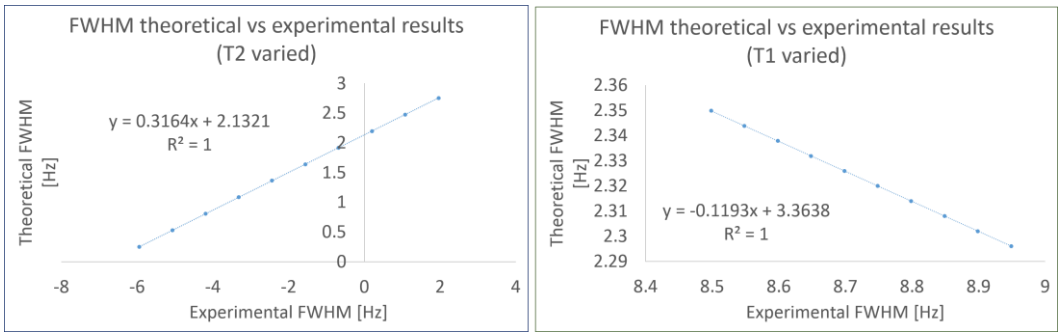

Figure 53: shows the correlation graphs when comparing the experimental vs theoretical results of the FWHM deduced from the Z-Spectra. On the left, the relationship was obtained when comparing the two fitted relationships that arose from the left hand side of figures 51 & 52. On the right, the relationship was obtained when comparing the two fitted relationships that arose from the right hand side of the same figures.

pH dependence

One of the most interesting results from this phantom study was the behaviour of the Z-Spectra when the pH was altered. Figure 54 shows a summary of the effects observed when BSA at 2.5% concentration was buffered at four different pH values and scanned simultaneously with the CEST sequence at B_1 saturation power equivalence of 0.9μT. As expected peaks are more or less enhanced depending on the pH.

Statistical significance of the observed peaks for different pH was performed as described in section 4.2.3 and the results are summarised in the form of boxplots (figure 55). At pH value of 7.3 (shown in blue), two visible CEST peaks exist, at 3.6ppm and at 2.2ppm. The slightly lower pH of value 7.0 (shown in light blue), reveals a less enhanced peak at 3.6ppm , another one of similar CEST effect (as at 7.3 pH value) at 2.2ppm but also a 'hint' of a peak around 2.8ppm. This almost invisible peak becomes more defined when the pH decreases even more, with a value of pH at 6.7 (shown in green). At this pH value, there is no observed peak at 3.6ppm anymore, but a defined peak around 2.9ppm and also a slightly shifted peak (compared to the higher pH values) at 2.3ppm. Finally, at a pH value of 6.4 (shown in red) the peak previously defined at 2.9ppm shifts slightly closer to 2.8ppm, giving a strong CEST signal. Also the peak around 2.3ppm remains visible but less enhanced.

From these observations it can be inferred that the peak resonating around 3.6ppm must be of very slow exchange rate (on the order of Amide exchange), as a decrease in pH reduces the exchange enough; therefore it is no longer within the range of optimum CEST (see section 2.3). As a surprise comes the peak at 2.2ppm which also behaves as if it was of slow exchange rate. This is due to the fact that it also decreases as pH decreases, but does not disappear completely. One could conclude that the exchange rate of the peak at 2.2ppm still lies within the lower limits of optimal exchange rates. It was also surprising to observe a third peak resonating around 2.9ppm. The specific peak seems to behave more like a fast exchangeable peak. This is because when the pH decreases the peak is more enhanced, suggesting that lowering its exchange rate, places it within the optimum exchange regime for the CEST effect.

The experimental findings (top image, blue outline), seem to agree with the modelled outcome (in orange outline, bottom image), using a five-pool model with the parameters listed in table 9. A five pool model was chosen based on the number of peaks experimentally observed.

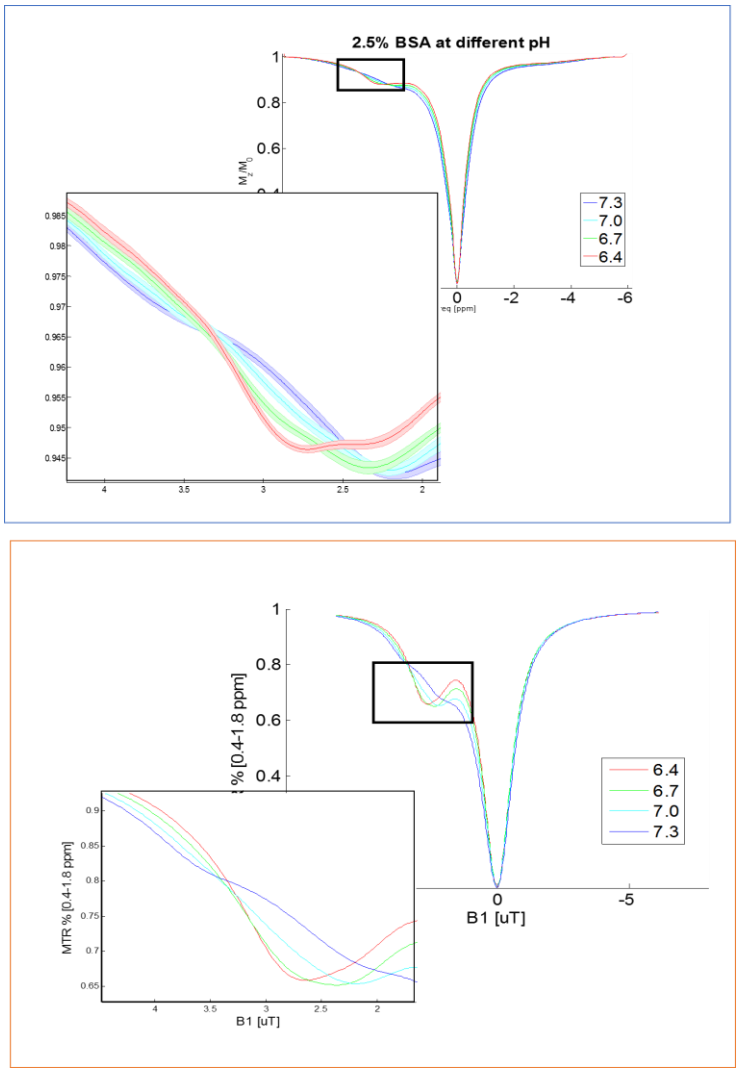

Figure 54: Illustration of four Z-Spectra each corresponding to a different pH value of BSA with concentration of 2.5%, scanned with a saturation pulse train of 0.9μT. CEST peaks differ depending on the pH value of the sample giving more, or less peak enhancement Top set of figures (in blue) experimental data, bottom set of figures (in orange) modelled data from a five-pool model.

Pool No.	Frequency [ppm]	Pool size (ratio to water)	Exchange rate [Hz], at pH=7	T_1 [ms]	T2 [ms]
1 (Water)	0	1	n/a	1850	37
2 (Amide)	2.2	0.0017	22	1500	10
2 (Amine)	2.9	0.0025	400	1500	10
4 (Amide)	3.6	0.0017	22	1500	10
5 (Aliphatic)	-3.5	0.04	4.5	260	0.3

Table 9: Summary of the parameters used per pool for the BSA phantom behaviour with different pH. Equations 15 and 16 were used to model the exchange rate dependence on pH.

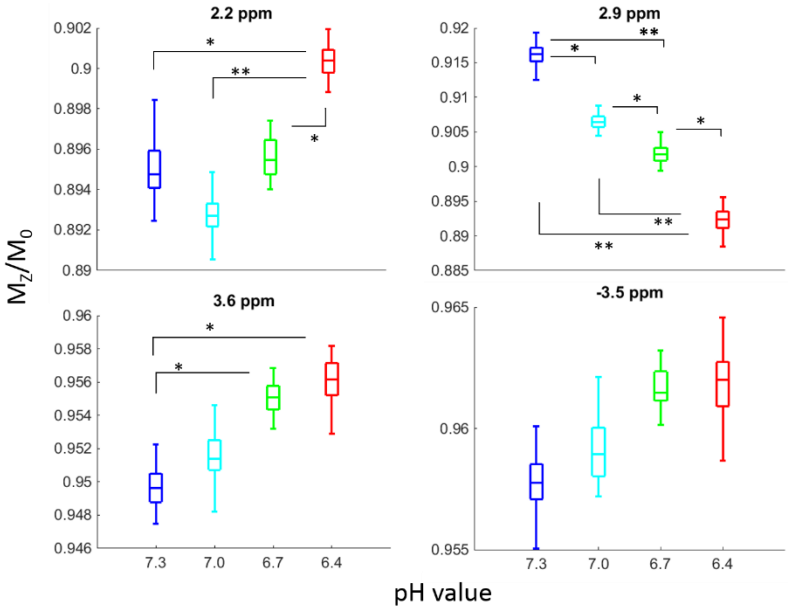

Figure 55: Displays boxplot analysis at the four frequency offsets discussed (2.2, 2.9, 3.6 and -3.5 ppm respectively). Statistical significance tests were applied for different pH values of the same frequency offsets and are given here in the star annotation.

There was also some minor shifting observed between the peak of 2.2 and 2.8ppm. At this stage it is not clear whether the shift is real or apparent due to the different CEST weighting of the two peaks involved, or even an induced error due to the fitting. The general model (see section 2.4) assumes little or no exchange between sites other than with water. This is mainly due to an assumption of soluble substances with much less concentration than water. However BSA is a very rich and complex structure which does not necessary dissolve completely, leading to areas around the protein with potentially more protein hydrogens available for exchange than water hydrogens. This could therefore allow exchange between the two peaks, which if fast enough, it could potentially become the cause of peak shifting (as explained in section 2.3, factors affecting the exchange rate).

Note that no significant differences (CL<0.68) were observed at the aliphatic peak, suggesting that it is not pH dependent. Similar effects were observed at all four concentrations.

B_1 power dependence

Investigation of the CEST effect with different B_1 saturation powers showed larger effect when higher B_1 saturation power was applied, as figure 56 reveals.

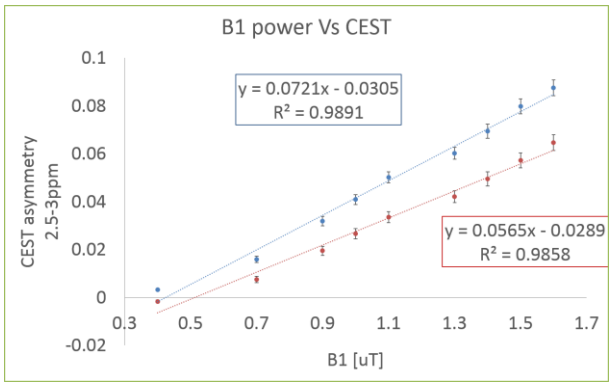

Figure 56: shows a series of CEST scanning at different saturation B_1 powers. Two phantoms are shown here, with pH values of 7.3 (blue data set) and 6.4 (red data set). Highly significant correlation for both curves ($p<0.001$, Pearson's correlation coefficient, for two-tailed test, $n=9$) suggests linear relationship between saturation power and CEST for the range of 2.5-3ppm and at low powers. See also Appendix F.

However careful considerations must be taken into account before deducing general conclusions. Although is not shown through these experiments, the theory suggests that there is an optimal B_1 power for each exchange rate (see section 3.1.2). Therefore, it is expected even for the curves shown here, to reach a maximum peak and not continue in this linear manner indefinitely. The optimum peak depends on the exchange rate, therefore is likely to differ for different exchangeable sites.

4.4. Conclusions

A range of experiments were conducted on a set of BSA phantoms in order to investigate the CEST effects under different physiological conditions and for different setups.

In summary, CEST was tested for spatial reproducibility showing no significant differences in various positions within the RF coil. There were also significant differences observed when different concentrations of BSA were assessed and when samples were scanned at different temperatures. Additionally, unexpected behaviour of the Z-Spectrum profile was observed for solutions of different pH values where peaks seemed to reduce in amplitude or possibly shift (due to the coalescence principle)

The main conclusion from this work is that when attempting to deduce quantitative values for different parameters from CEST experiments, one must be aware that equivalent CEST values can arise from different combinations of concentration, pH,

temperature and the applied B_1 saturation power. One must also take into account the T_1 and T_2 values of the specific tissue, and how those will affect the CEST profile. It is therefore very important to have estimated or directly measured as many of these parameters as possible, in order to obtain reliable, non-confounded inferences from the CEST data.

Chapter 5. Investigation of the CEST signal in the spine of mice with neurodegenerative diseases

This chapter describes the implementation of CEST dedicated to the mouse spine. It also outlines the results from the study of two neurodegenerative disease mouse models provided by the Graham Watts laboratories led by Prof Linda Greensmith, a model of Amyotrophic Lateral Sclerosis (ALS) and a model of Spinal and Bulbar Muscular Atrophy (SBMA). Both mice models are characterised by protein level changes within the spine of affected mice. The CEST technique is known to be sensitive to, among others, the concentration of exchangeable protons. Considering that proteins contain many Amide and Amine groups, CEST was chosen as the appropriate method for assessing the protein changes. Differences in Z-Spectra of healthy compared to affected mice might relate to the potential changes in protein concentration within the spines.

5.1. Experimental procedures

This section offers a description of the experimental setup optimised for the in-vivo scanning of the mouse spine with the CEST sequence (see 5.1.1). In addition, a brief section is included on CEST data processing (section 5.1.2) with Matlab codes written jointly by Francisco Torrealdea (PhD student, Institute of Neurology) and myself. Finally there is a summary of the procedures followed in order to get quantitative values of protein concentrations from the spinal cords (section 5.1.3). The protein quantification procedures were performed by Phillip Smethurst (PhD student, Institute of Neurology) as part of the collaborative project: '*The SOD1 mouse model of Amyotrophic Lateral Sclerosis*', see section 5.2 and also by Anna Gray (PhD student, Institute of Neurology) as part of the collaborative project: '*Spinal and Bulbar Muscular Atrophy mouse model*', see section 5.3.

5.1.1. CEST sequence for the mouse spine

The saturation part of the CEST protocol consisted of 100 Gaussian shaped pulses (duration 50ms and inter-pulse delay of 5ms), each at a flip angle of 540^{o} (giving the equivalent of 0.9 μT of B_1 mean amplitude, see table 6). The CEST acquisition was repeated for 77 frequency offsets linearly spaced within ±6ppm starting from -6ppm alternating to the corresponding positive point and finishing with zero. This range was judged enough to cover the aliphatic side (from about -2.5 up to -5 ppm) and also the positive Amines (around 1.8 to 2.2 ppm) and Amides (from 3 to 4 ppm). B_0 correction was performed by finding the minimum point of the Z-Spectrum and setting that to the frequency of water (zero). Additionally five frequency offsets at 200ppm (far away from any potential MT effects) were acquired for normalisation purposes (Total number of frequency offsets, NF = 82).

Due to the size of the mouse spine, a spectroscopic CEST sequence was judged to be the most suited for these studies. Therefore the saturation scheme was followed by a single voxel 'point resolved' spectroscopic readout (PRESS), modified version of the EXPRESS sequence previously reported by Walker-Samuel et al [86]. The PRESS readout uses three selective excitation pulses (90^{o} applied along the slice selection direction and 180^{o} pulses along the other two orthogonal directions). The signal was acquired at the second echo (TE_2=8ms), with 100 sampling points at a spectral bandwidth of 1000Hz. Refer to the following diagram, figure 57 for a detailed description of the acquisition protocol.

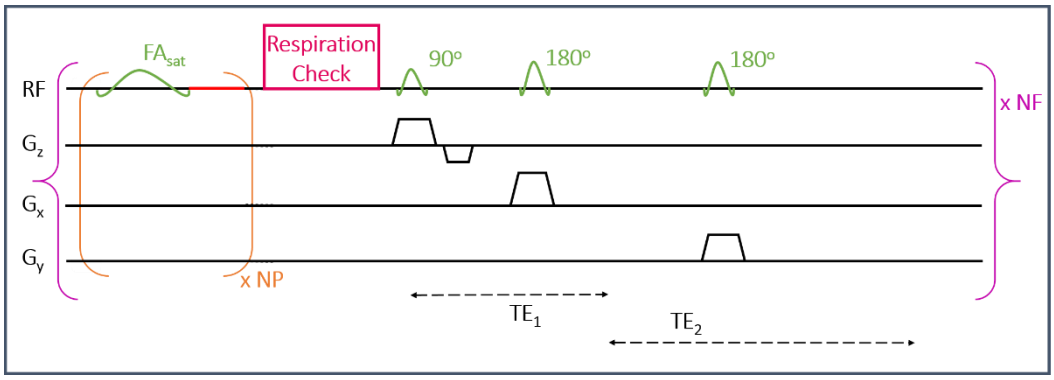

Figure 57: is a schematic of the CEST acquisition applied in the mouse spine. All RF pulses are displayed in green and gradients in black. Orange colour indicates the number of saturation pulses applied with an inter-pulse delay (in red) of 5ms (total number of saturation pulses, NP=100). FA_{sat} indicates the flip angle (540°) with B_1 power equivalence of 0.9μT, as also given in table 6. TE_1=TE_2=8ms with signal acquired following TE_2 with 100 sampling points and at a spectral bandwidth of 1000Hz.Total number of frequency offsets (NF=82), displayed in purple. The pink box following the saturation train of pulses indicates the respiration pattern check prior allowing for the readout.

Triggering for respiration

Spine MRI is very susceptible to motion, mainly due to breathing. Thus, prior the readout, respiration triggering was necessary. Figure 58 shows the typical breathing pattern of a mouse under anaesthesia. In orange is an illustration of the respiration plateau, i.e. the time within this pattern that data collection is allowed when respiration triggering is enabled. However conventional respiration triggering becomes problematic in CEST applications for two reasons.

First, the signal must be acquired immediately after the saturation scheme to avoid magnetisation recovery which will lead to losses in CEST contrast. With conventional respiration triggering enabled and by taking into account the average breathing pattern of a average mouse (≈ 80 breaths/minute), there is a chance of waiting time from 0 up to 0.25 seconds between the saturation scheme and the readout due to the fact that data acquisition is only permitted during the respiration plateau (orange part of figure 58). This is an estimated value considering a plateau of 0.5 seconds during the complete breath cycle (0.75s), which leaves a time between plateaus of 0.25s.

Additionally, if there was to be some delay between saturation and readout, it certainly should not be random. Thus the above scenario which offers a delay of 0-0.75s does not seem ideal.

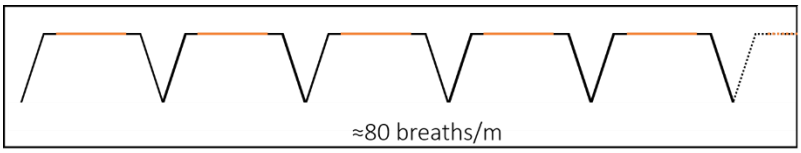

*Figure 58: schematic representation of the respiration pattern of a mouse, under anaesthesia while being scanned. The mouse is placed laying on its back, and Isoflurane levels are maintained at about 1.3% in a mixture of pure oxygen and air (20% oxygen). In orange, an illustration of what is referred to as '**plateau**', i.e. the time in the breathing pattern which signal is allowed to be acquired. Typically under these conditions mice respiration remains at a rate of 80 breaths per minute, which means that between each plateau there could be approximately 0.25 seconds.*

To overcome these problems and achieve respiration triggering while the delay between saturation and readout is always constant, and at the minimum value possible, the protocol had to be adjusted. This somewhat altered protocol included additional saturation pulses, following the main saturation scheme of 100 pulses (5.5 seconds), which were applied one at a time if the respiration triggering condition was not enabled yet. Figure 59 below gives a logical diagram explaining how respiration triggering was achieved for the CEST experiments in the mouse spine.

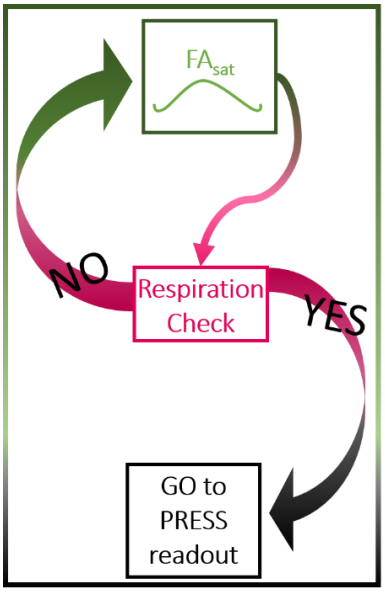

Figure 59: illustration of respiration triggering check. Following the main saturation scheme, a signal is sent to check whether it is OK to proceed to readout. If the mouse respiration is within the plateau then PRESS readout is applied. Otherwise, one additional saturation pulse is applied, maintaining the saturation at steady state. At the end of the saturation pulse, another respiration check is performed. According to the respiration pattern of the typical mouse discussed above, this process might take up to an additional 0.25 seconds adding to the system a maximum of 13 extra saturation pulses.

The above method describing how to trigger for respiration while conducting a CEST experiment might raise some concerns on the effect of the additional saturation time added for different frequency offsets. However simulations were performed in order

to study the evolution of water magnetisation under different saturation times, which showed no effective differences between the application of 5.5 seconds (case were no additional saturation time would be needed other than the 100 pulses) and the additional 0.25 seconds of saturation (case were the maximum extra saturation time would be needed with 13 extra pulses). This is because following 5.5 seconds of saturation the signal is already close to steady state and the additional saturation will not have a considerable effect on the CEST contrast. Figure 60 shows the simulated data for two frequency offsets: at 2 and 3.5 ppm from water using a two pool model (pool A to be water and pool B the exchangeable site at a frequency offset given in ppm from water). Section 2.4.1 gives a detailed description of the theoretical model based on the Bloch-McConnell equations.

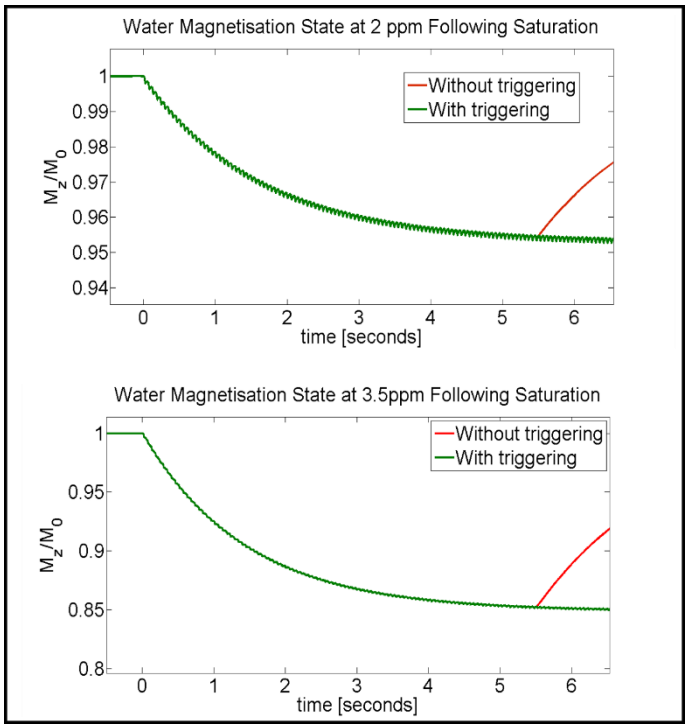

Figure 60: displays the simulated data from two frequency offsets, using a two pool Bloch-McConnell equations model. Top figure: the evolution of Z magnetisation when pool B is set to 2ppm and is connected to pool A with an exchange rate of 2000Hz. A saturation train of pulses is applied at 2ppm (on resonance to the exchangeable pool B). In green is the evolution of the water signal when additional pulses are added (more than 100), to model the case of respiration triggering. In red is the evolution of the water signal when no additional pulses are added. Instead, a wait time is introduced prior the readout which corresponds to the waiting for conventional triggering; within that time, the magnetisation recovers with T_1. Bottom figure: the evolution of Z magnetisation when pool B is set to 3.5ppm and is connected to pool A with an exchange rate of 30Hz. A saturation train of pulses is applied at 3.5ppm (on resonance to the exchangeable pool B). Green and red correspond to with and without triggering for spine, similar to the top figure. Other parameters used: T_{1a}=1700ms, T_{2a}=32ms [87], T_{1b}=1000ms, T_{2b}=10ms, Saturation scheme: Gaussian pulses (5σ as applied in the 9.4T MRI scanner) of 50ms duration and with 5ms inter-pulse delay. Pool B at a concentration of 100mM.

Observe the evolution of the signal in green (both graphs above) between 5.5 and 5.75 (5.5 plus 0.25) seconds. The change corresponds to 0.15% for the 2ppm case (from a signal value of 0.9546 to 0.9532) and 0.18% for the 3.5ppm case (from a signal value of 0.9546 to 0.9532). On the contrary, if no saturation is to be used during triggering, as simulated and shown in red the relaxation effect dominates and reduces the CEST contrast. The change for the 2ppm case is 0.67% (from a signal value of 0.9546 to 0.9609) and for the 3.5ppm case the change corresponds to 2.19% (from signal value 0.8523 to 0.8710)

In conclusion, when using the triggering scheme which allows the application of additional saturation pulses, the system remains in a state of saturation (and also steady state) until signal readout is considered acceptable. In addition the delay between the saturation train and the readout is always constant, allowing the same signal recovery for all the frequency offsets.

Voxel optimisation

Spinal cord CEST lead to another major problem: outer volume suppression (OVS) restriction. Due to the nature of CEST as mentioned in the previous section, the readout must follow as soon as saturation is applied. If one choses to apply outer volume suppression as well, the delay between saturation and readout would increase. To minimise additional delays no OVS was applied. Instead, to ensure that no signal was received from the 'outer volume', the voxel size was optimised in a separate experiment, to give the same signal as when compared with the same voxel following OVS. A voxel of 1x1x4mm^3 was found to be suited in order to avoid outer volume contributions.

Shimming was manually performed for all the experiments within the selected voxel (respiration triggering enabled), to a linewidth of 38 ±3 Hz (0.095 ± 0.008 ppm). Additionally, manual power calibration and frequency shift correction were performed within the voxel of interest.

5.1.2. Post-Processing of CEST data

A minimum of three data sets were acquired per animal. In addition, when data were subjectively judged to be of lower quality than the average, up to three more sets were also acquired. This was done to further decrease artefacts due to breathing or other movement. Raw data were uploaded in Matlab for post-processing. The water signal acquired per frequency offset was fitted to a Lorentzian line shape and integration was done over the range ±. 0.025 ppm from the maximum water signal. The integrated value was used as the water Mz value for the corresponding frequency offset.

All the repeated data acquired per mouse were averaged with weighting in order to minimise the effect of outliers. The weighting factor was calculated per point depending on its relative distance to the rest of the points. This method was decided after careful observation of the data sets which showed that occasionally the measured signal read was clearly erroneous due to some physiological movement. The simple illustration below (figure 61) shows four points collected at the same frequency offset (f). While three of the points (A, B and C) are much closer to each other with similar Mz values, point D (in red) is of much lower Mz value than the rest. Therefore point D is almost not taken into account when the weighted averaging method is used (the impact factor of point D is calculated to be much smaller compared to the rest points). Equation 26 gives the calculated Impact Factor (IF) for a given point (i), by taking into account the summation of the distance of all points j from the point i.

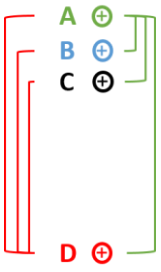

Figure 61: illustration of four points collected from the same frequency offset (f). It is clear how points A, B and C (green, blue and black respectively) are of much closer Mz values compared to point D. With the weighted averaging method described in this section an impact factor is assigned per point, inversely proportional to the distance between the points.

$$IF(i) = \left[\sum_j |x_i - x_j|\right]^p \qquad (26)$$

where IF is the Impact Factor per (i) point and j corresponds to the entire set of points per frequency offset. P was assigned to the value of -2 after a few trials with different values in order to determine a factor that was giving less weighting but not complete elimination of the outlying points. Once the IF values were determined per data point, a weighted average value was calculated for all frequency offsets as given in equation 27 below.

$$M_Z(f) = \frac{\sum_i IF_i(f).x_i(f)}{\sum_i IF(f)} \qquad (27)$$

where Mz corresponds to the weighted average of Z magnetisation per frequency offset, f when i data points were collected individually (x).

Figure 62 shows an example case where four data sets were acquired (shown in blue, red, green and pink respectively). The black line shows the weighted average of the four data sets. The data points in circles indicate the outliers which do not represent the realistic trend of the Z-Spectra and therefore their IF value was calculated to be very low compared to the rest of the data. If conventional data averaging was used, the outliers would compromise the shape of the Z-Spectrum by creating false peaks at random frequency offsets.

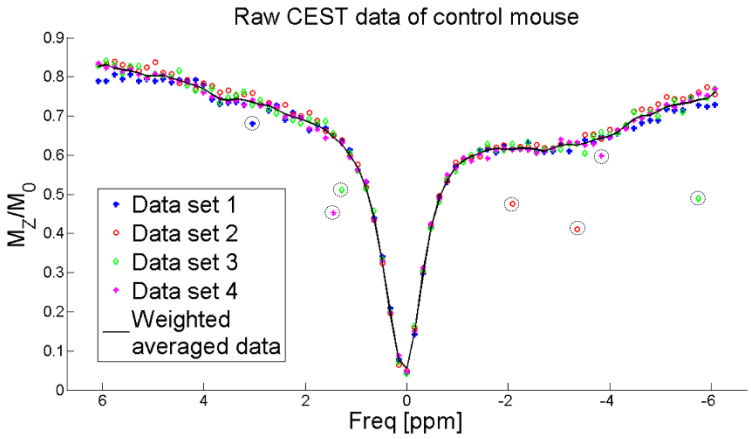

Figure 62: shows an example case were four data sets were acquired from the spine (Lumbar section) of a control mouse (shown in blue, red green and pink respectively). In black, the weighted average of the four data sets, prior to any additional smoothing. The circled points correspond to data acquisition during movement which results to instantaneous water signal change (due to changes of shimming as well as voxel mismatch). If conventional averaging were used, these outliers would affect the shape of the Z-spectrum by creating false peaks at different frequencies.

Following weighted averaging, the Z Spectra were normalised to the point acquired at 200ppm and fitted to a smoothing spline function. Z-Spectra were then B_0 corrected

and interpolated to 1001 points for further interpretation at different frequency offsets including the MTR values (equation 21) between 3.3 to 3.7 ppm (centred at 3.5ppm, were Amide peaks resonate) and between 1.8 to 2.2 ppm (centred at 2.0ppm, were Amine peaks resonate).

5.1.3. Post-Mortem protein quantification

Following MRI scans, mice were euthanized with 0.1ml of Pentorbarbitone and cardially perfused with 0.9% saline. Spinal cords were then extracted and dissected into the sections of interest (depending on the voxel positioning from the CEST scan). The dissected sections were snap frozen in liquid nitrogen and stored at -80^{0}C for use when all samples are gathered at the end of each project.

SOD1 mouse model protocol (by Phillip Smethurst, PhD student, Institute of Neurology)

Analysis of the protein levels required separation into soluble and insoluble fractions. As such, spinal cord segments were weighted and extracted in 1:20 (weight/volume) of TEN buffer[18] containing 0.5% NP-40[19] and 1x protease inhibitor cocktail. Samples are then sonicated on ice using a probe sonicator (Soniprep 150). The lysate was then ultracentrifuged at 100000xg for five minutes and the supernatant was kept as the soluble fraction. The pellet was then re-suspended in 500μl of 1x TEN buffer with 1% of NP-40 and 1x protease inhibitor by sonication as before, then ultracentrifuged again at 100000xg for five more minutes. The pellet was then resuspended in equal volume of water and sonicated as before. Total soluble and insoluble protein concentrations were determined using the Bicinchoninic acid (BCA) protein assay method and Bovine Serum Albumin as the standard [88]. In addition, 50 μg of protein was loaded to the gel for western blotting. Soluble and insoluble SOD1 protein fractions were estimated with the anti-SOD1 antibody and beta actin (β-actin) as the standard [89]. SOD1 staining was only applied to the SOD1 transgenic mice. BCA results for total protein fractions are reported as mg of protein per ml of dilution (1:20)

[18] 10mM Tris, 1mM EDTA, 100mM NaCl at pH=8.0

[19] A mild detergent commonly used to break open cell membranes

while western blot results for SOD1 protein fractions are relative to the protein loaded and therefore are given in a.u.

SBMA mouse model protocol (by Anna Gray, PhD student, Institute of Neurology)

During the SBMA study the primary focus was on total soluble proteins, therefore no insoluble proteins were quantified and no western blotting was perform for specific protein staining. The protocol used for BCA assay was slightly altered as the tissue was extracted in 1:4 (weight/volume) in TEN buffer (instead of 1:20 as previously described). Results are reported in mg of protein per ml of dilution.

It is important to understand that the results of the two mouse studies cannot be compared between them as they were performed at different times and following slightly different protocols. Nonetheless, they are suitable for comparison of the relative protein levels of mice within the same study.

5.2. Amyotrophic Lateral Sclerosis mouse model

This section describes all the experiments done when studying the CEST signal in a genetically modified SOD1 mutant mouse model, which closely resembles the human form of ALS, a devastating Motor Neuron Disease (MND) with no current reliable biomarker. The project aimed to differentiate diseased from control animals by exploring the endogenous CEST signal in the spinal cord and relating the findings to the levels of post mortem protein.

5.2.1. Introduction

ALS is a neurodegenerative disease which affects the motor neurons and usually leads to total paralysis, including the inability to swallow or even breathe without machine support; typically ALS patients die from respiratory failure within two to ten years [90]. ALS is considered mostly sporadic (not hereditary) with a small fraction (5 - 10%) diagnosed as familial (fALS). To date about 5000 people are diagnosed with ALS in the UK alone [91, 92] at an estimated prevalence of 3:100000

very similar to that of Multiple Sclerosis (MS), which is widely considered to be one of the most common MNDs [93]. Extensive research is concentrated on finding early diagnostic markers for MNDs, which would enable treatment to begin earlier and help improve the quality of life for late disease stages.

To this day ALS has no pre-symptomatic diagnostic tool and the processes responsible for the disease are not yet fully understood yet despite ongoing research in the field. Major advances have taken place in developing rodent models which resemble ALS since the discovery of various Copper/Zinc superoxide dismutase 1 (Cu/Zn SOD1) gene mutations [94] from the fALS cases. Currently, the SOD1 model seems to be most established to study the ALS neuropathology because similar disease characteristics are observed in humans and rodents [95, 96, 97]. These include glial and motor neuron loss in the spine and brain, mitochondrial dysfunction and neuromuscular malfunction leading to limb paralysis [98, 99].

5.2.2. The SOD1-G93A mouse model

The SOD1-G93A mouse model used for this study, remains the most well-established of all the SOD1 models generated through the years. This is due to its age related motor phenotype which resembles the human neuropathology better than any other SOD1 model tested [97].

The genetically modified SOD1 mice overexpress the human form of SOD1 protein and as a result, cytosolic aggregates of SOD1-rich fibril inclusions are formed and accumulate in the spinal cord within months of birth [100]. Specifically, reports have revealed the increased formation of unfolded proteins by day 50 from birth for the transgenic animals [101] with the majority of aggregates (such as filament proteins alpha-internexin and periphenin) seen in the cervical and thoracic regions of the spinal cord. At severe stages of the disease similar levels are seen in all spinal cord regions, including the lumbar and sacral regions.

Nucleation- Polymerisation Model

Insoluble protein concentrations from these animals can be associated with the so-called *'Nucleation-polymerisation model'*. This model is found to apply to various

neurodegenerative diseases, including Alzheimer's, Parkinson's, and Huntington's diseases, as well as frontotemporal lobar degeneration and Amyotrophic lateral sclerosis [102]. It has been verified in-vitro (cell culture), and used as a guide-model in the further understanding of the different diseases mentioned above. Figure 63 is an illustration of the model, where monomers and native form proteins undergo conformational changes and misfoldings (Nucleation phase), which grow at a rapid pace to form fibrils and aggregates (Polymerisation or Elongation phase).

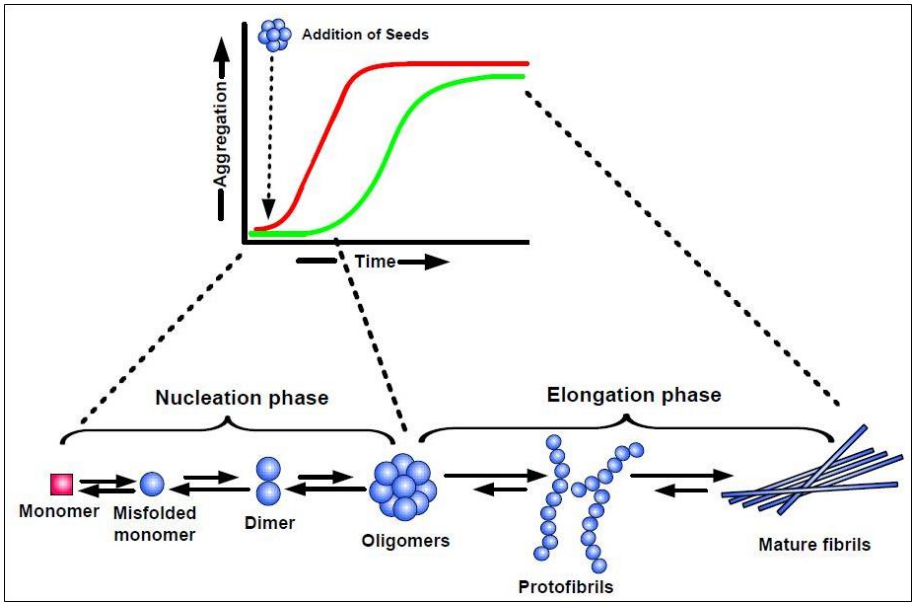

Figure 63: is an illustration of the Nucleation-polymerisation model. Nucleation is the phase in which conformational change and protein misfolding occurs. During the polymerisation phase, the already misfolded proteins create fibrils which grow very rapidly to form mature fibrils and aggregates. The graph shows how protein aggregation changes with age: In green is a healthy aging process where aggregates form but at a low pace compared to the disease process (in red) which shows a much more rapid growth and at earlier stage. Figure reproduced from Kumar and Walter, 2011 [103].

Studies suggest that prior to protein aggregation the SOD1 proteins exist in soluble form and only form large aggregates when the disease is already at late stages [104, 105] & [106]. Proteins in aggregated form could potentially result in less accessibility in some of the hydrogens for interaction with the free surrounding water. As the CEST technique is sensitive to exchangeable groups such as Amides and Amines, it was considered as a potential method to investigate the total protein changes within the spinal cord of mice before the formation of SOD1 aggregates which could restrict

the exchange between water and protein hydrogens. If successful, it could serve as a potential early biomarker of the disease.

5.2.3. Methods

Two groups of mice were used in this study, human mutate SOD1 (n=21) and healthy controls, also referred to as wild type (WT), as they carry the WT form of SOD1 (n=21). Each group was furthermore split into three subgroups (of n=7), for the purposes of different disease time course scanning. This was done so post-mortem protein quantification could be performed at different stages. Subgroup A (n=7 wt & n=7 SOD1) was scanned at 45±1 days of age which is considered an early stage in terms of protein aggregation for this model and also pre-symptomatic for the disease. Subgroup B (n=7 wt & n=7 SOD1) was scanned at 90±1 days of age, still considered pre-symptomatic, just a few days before the 105 days which is reported to be the time when the first clinical signs occur [107]. Lastly, subgroup C (n=7 wt & n=7 SOD1) was scanned at 120±1 days of age which is considered to be symptomatic and near the end stage of the disease [108].

Anaesthesia was initially induced with 3% Isoflurane and the mice were kept anaesthetised during the entire scanning procedure with 1.3% isoflurane in a mixture of pure oxygen and air (Additional oxygen comprises 20% of the mixture). Mice were placed on their back (to minimise motion artefacts) on a small cylindrical bed and kept anaesthetised through a mouth mask. Respiration was monitored through a pressure pad and kept at around 80 breaths per minute by adjusting the isoflurane percentage. Body temperature was maintained at 37^{o}C through a system of hot air receiving feedback through a temperature probe which was placed next to the mouse. All procedures were conducted under an approved protocol from the Home Office.

Mice were scanned in all three planes for voxel positioning (voxel size: 1x1x4mm^{3}) and the signal within the voxel was shimmed achieving a linewidth of 38 ±3 Hz. CEST scans were performed with the parameters and setup described in section 5.1.1. CEST data were acquired from the Lumbar enlargement, located between vertebrae T11-L1. This region is deemed to be the most susceptible to protein aggregation in SOD1 animals [100]. The voxel location is illustrated in figure 64 below, shown in green.

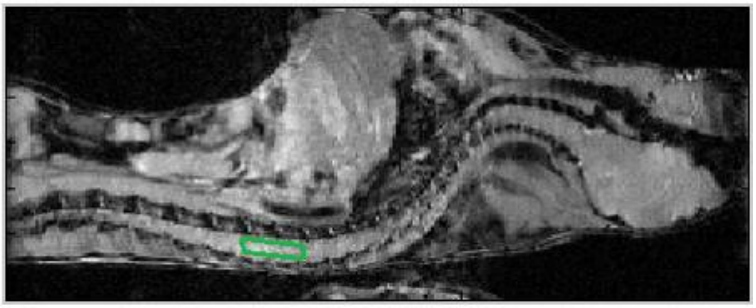

Figure 64: shows a localiser image of a control mouse in sagittal slice plan. Voxel location shown in green, is placed between T11-L1 vertebrae which is known as the Lumbar enlargement.

All scans were performed on a horizontal 9.4T MRI scanner (Agilent Technologies) with a receive/transmit volume coil of internal diameter of 33mm (Rapid Biomedical). Following scanning, all mice were culled for post-mortem protein quantification as already mentioned in section 5.1.3.

CEST data were post processed as described in section 5.1.2 and MTR percentage values were calculated at 3.5ppm for all mice.

5.2.4. Results & Discussion

This section summarises the comparison of CEST to the post-mortem protein concentrations of the total soluble fractions found in the Lumbar region per mouse group respectively (WT and SOD1 for 45, 90 and 120 days of age). The insoluble protein concentrations are also presented, as they offer valuable information about the disease and in addition may be related to the soluble protein concentrations.

CEST versus total soluble protein levels

The calculated MTR values at 3.5ppm show no significant differences ($p>0.1$) in either the control or SOD1 mice through the time course of the disease. Figure 65 summarises the CEST results acquired in the Lumbar enlargement and furthermore reports the total soluble protein levels from the post-mortem analysis following MRI.

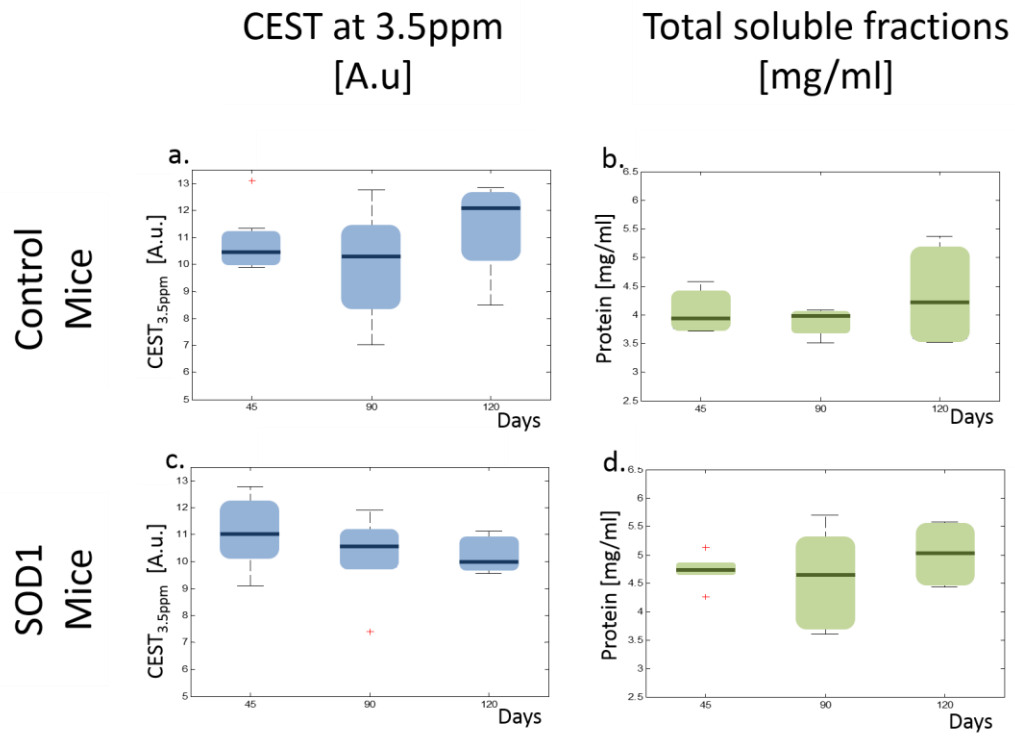

Figure 65: shows comparisons between the CEST results (boxplots in blue) and total soluble protein levels (boxplots in green). Control mice are shown on the top two figures while SOD1 mice are shown on the bottom ones. Each figure contains three boxplots: 45, 90 and 120 days of age respectively.

The MTR percentages consistently remain around 11% for both groups. These findings are supported by the total soluble protein fractions which show the same pattern as CEST: no significant changes ($p>0.1$) either in control or SOD1 mice. For the control animals, the protein levels remained between 4 and 4.5 mg/ml throughout their entire lifespan. Likewise, no increase was observed either from the SOD1 animals, although there is a trend for slightly higher protein levels (values between 4.5 and 5 mg/ml). This difference however is not significant and is not reflected in the CEST data either.

Reproducibility of Z-Spectra during in vivo experiments

In addition to the CEST signal analysed as the MTR at 3.5ppm one might consider to investigate different frequency ranges such as the aliphatic frequency range (centred around -3.5ppm) which may give information about the aggregates/insoluble proteins (as investigated in the human brain [109]), or the Amine range (centred at 2ppm), which could give information about the fast exchangeable (soluble) proteins. In fact, no differences were found comparing the average Z-Spectra of control and

SOD1 at the three different time points. As it can be seen in the following figures (66, 67 and 68), Z-Spectra are in complete overlap within error, which suggests that the lack of detectable differences is not due to poor measurement accuracy. The nicely demarcated features in these spectra indicate the level of reproducibility of the CEST method, with no differentiation between SOD1 and control mice.

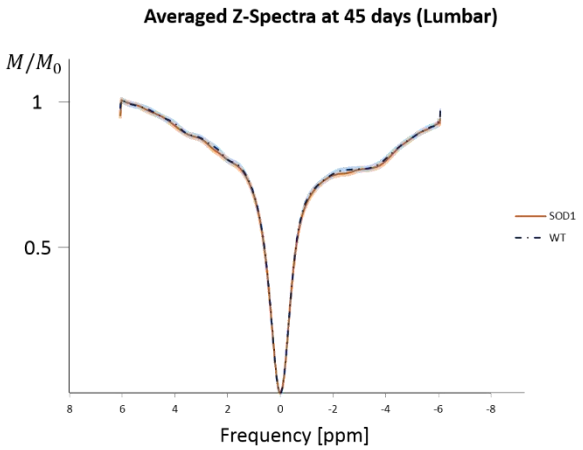

*Figure 66: shows the average Z-Spectra acquired from the Lumbar enlargement of the SOD1 (in solid red line) and the control (in dashed blue line) mice at **45 days of age**. Note the standard error is illustrated per data set as a shaded region, of the same colour for each mouse group respectively.*

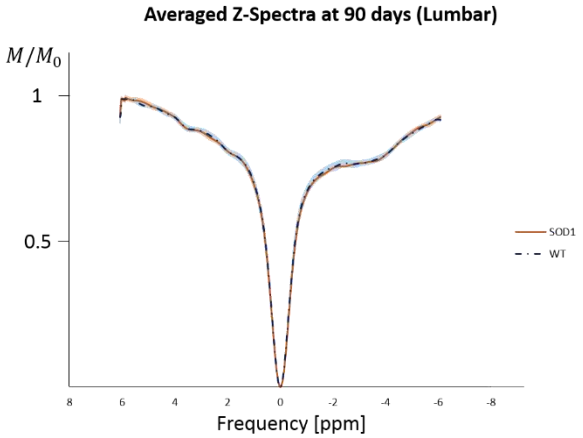

*Figure 67: shows the average Z-Spectra acquired from the Lumbar enlargement of the SOD1 (in solid red line) and the control (in dashed blue line) mice at **90 days of age**. Note the standard error is illustrated per data set as a shaded region, of the same colour for each mouse group respectively.*

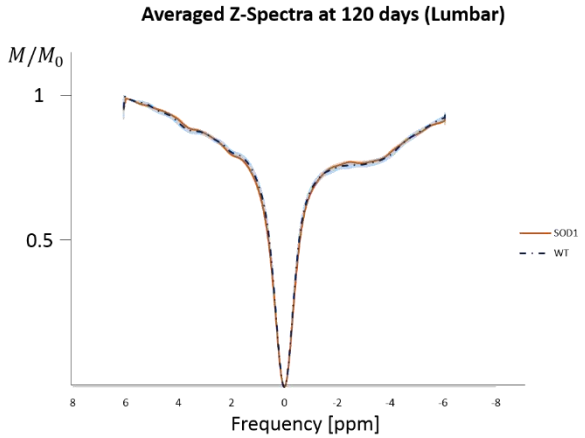

Figure 68: shows the average Z-Spectra acquired from the Lumbar enlargement of the SOD1 (in solid red line) and the control (in dashed blue line) mice at ***120 days of age****. Note the standard error is illustrated per data set as a shaded region, of the same colour for each mouse group respectively.*

Insoluble protein levels

The insoluble protein fractions, formed by aggregates and fibrils, were also obtained by western blots as described in section 5.1.3. The insoluble part of protein is not detectable with the CEST technique, as it does not exist in an aqueous solution which would allow chemical exchange of protons. However, they were still analysed as they give valuable information about the disease mechanism and help toward a deeper understanding of the protein accumulation process throughout the disease time course. Figure 69 shows the total insoluble protein concentrations of the control (top figure) and SOD1 mice (bottom) at the different time points (45, 90 and 120 days of age) and figure 70 shows the SOD1 specific insoluble protein concentrations.

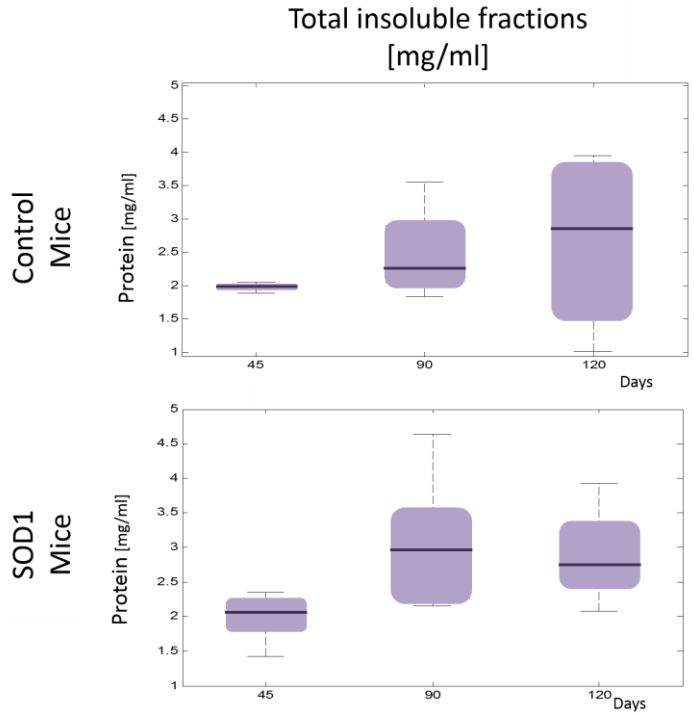

Figure 69: Total insoluble concentrations from control mice (top figure) and SOD1 mice (bottom figure). At 45 days of age both mice groups appear to have similar levels of insoluble protein within the spine (concentration of 2mg/ml). As the mice age, their insoluble protein concentration increases (from 2 to about 3 mg/ml). In control mice the increase is not significant (the variation across individual mice is too large) neither at 90 nor 120 days of age. However, in the case of SOD1 mice, the increase in concentration from 45 to 90 days of age is significant ($p<0.05$). Similar levels are maintained from 90 to 120 days of age for the SOD1 mice (no further increase).

General trends in total insoluble protein concentrations indicate a slight increase from 45 to 90 days of age. In control animals, the increase is not significant neither for 90 nor for 120 days of age; it is only a trend (2mg/ml, slightly increasing to 2.2mg/ml at 90 days old and reaching 2.8mg/ml at 120 days old) with high variability across specific mice. In SOD1 animals however, the increase in total insoluble protein levels is significant ($p<0.05$) from 45 to 90 days of age (from 2 to 3mg/ml). This is supported by Kieran et al [101], claiming an increased formation of unfolded proteins by day 50. If changes in soluble proteins were to occur prior the increase in aggregation as theory suggests [102], they would have occurred between 45 and 90 days of age. No further significant difference is observed from 90 to 120 days of age, the protein levels remain around 3mg/ml.

Moreover, comparisons of the SOD1 only insoluble protein in the transgenic mice, show a significant difference between 90 and 120 days of age ($p<0.01$). No differences were observed between 45 and 90 days old mice. From the protein values it seems

that although the SOD1 insoluble protein is increased, there was no similar increase in the total insoluble protein levels between 90 and 120 days of age.

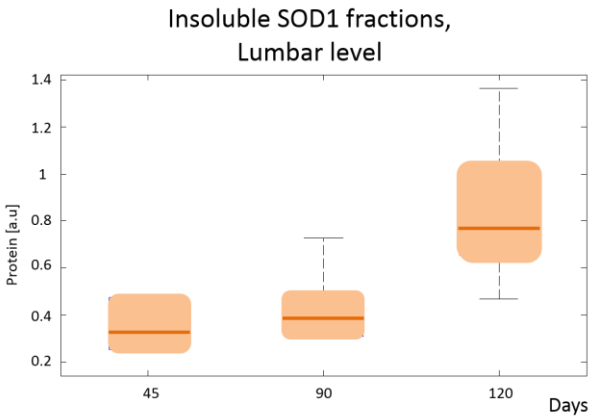

Figure 70: SOD1 insoluble concentrations from transgenic mice reveals a significant increase ($p<0.01$) in concentration between 90 and 120 days of age (from a mean value of 0.35 to 0.78l). Similar levels are maintained from 45 to 90 days of age for the SOD1 mice.

This increase in SOD1 protein leads to a further consideration of how SOD1 mice react, as it seems to compromise by changing the levels of other proteins in order to keep the total concentration at the same level. However, figure 70 suggests that (as previously stated for the total insoluble protein case), if soluble protein levels were to change prior to the formation of aggregates, it would have occurred between 90 and 120 days of age. Whether that would also have resulted in an increase in the total soluble protein concentration, is unclear.

5.2.5. Conclusions

From the results discussed above, no significant differences were found between control and SOD1 mice at any of the three time points investigated with the CEST technique. In addition, no significant differences were observed in soluble protein levels either, while insoluble protein level changes where observed. This might be an indication that the SOD1 mouse model is not the most appropriate one for the validation of the CEST technique in vivo due to the very short life span of the affected mice, which is on average between 120 and 130 days only. As figure 69 shows, the increase in insoluble protein levels occurred between 45 and 90 days of age, suggesting the possibility of soluble protein formation within that period. Therefore, scanning at 45 days of age may have been earlier than the soluble protein formation

(if there was any) point. Similarly, at 90 days of age, the soluble proteins could have already formed aggregates, in which case their concentration would not be elevated any more. Due to the fast onset of the specific disease model, any changes in soluble proteins might have occurred very rapidly (within one day or two), and hence be very difficult to track.

If further work is to be carried out with this animal model, a study on protein levels should be done with samples taken at more time points, before any further CEST data are collected. This should include protein quantification (both soluble and insoluble) of mice aged between 45 and 90 days, as differences are likely to exist (figure 69). Likewise, protein quantification should also be done between 90 and 120 days of age, as the results in figure 70 suggest an increase in SOD1 insoluble levels. These would lead to better justified conclusions for whether the CEST technique would be suited for this disease model, depending on the soluble protein levels observed. On the contrary, if no further work is to be carried out with the SOD1 mouse model and alternative ones are to be considered, they should ideally be of slower disease progression. If such a model allows slower rates of protein concentration changes, it might give more flexibility for detection with the CEST technique.

In summary, there is no conclusive evidence from this study whether the CEST technique is suitable for the detection of accumulated protein within the spinal cord of SOD1 mice. However despite the inconclusive results already discussed, this study showed that for the purposes of mice spinal cord CEST, a challenging application due to the size of the voxels and the highly inhomogeneous environments, the CEST measurement was reproducible and of high stability. Furthermore, the CEST measurements were validated by the direct measurements of protein fractions, which verified no significant differences between mice and throughout the disease time-course.

5.3. Spinal and Bulbar Muscular Atrophy mouse model

This section describes all the experiments performed when studying the CEST signal in an additional genetically modified mouse model, the SBMA, which exhibits the main characteristic features of the human form of spinal and bulbar muscular atrophy disease. Similar to ALS (studied previously, section 5.2), the SBMA disorder is an MND with no current reproducible biomarker or disease altering treatment. In contrast to the SOD1 mice with a disease lifespan of 130 days maximum, SBMA are slower to progress, with a disease lifespan of about 18 months in mice. It is known to be caused by polyglutamine repeat expansion in the Androgen receptor (AR mutations), a polymer with plenty of Amine and Amide groups detectable with the CEST technique. Therefore, the SBMA model was suggested as an alternative option for the validation of the CEST technique in-vivo as the results from the SOD1 model were unclear (sections 5.2.4 and 5.2.5 for discussion and conclusion of this work, respectively).

This project aimed to differentiate diseased from control animals by exploring the endogenous CEST signal in the spinal cord and relating the findings to the levels of post mortem protein quantification through protein assays. In addition, volumetric scans were done in order to evaluate muscular loss with disease progression in the lower limb.

5.3.1. The AR100 SBMA mouse model

SBMA is a devastating hereditary, male only neurodegenerative disease, with an estimate prevalence of 1 in 50000 [110, 111]. During the disease onset the individual experiences weakness of facial, bulbar and limb muscles due to motor neuron loss and degeneration in the spinal cord and brain stem [112, 111]. SBMA is known to be caused by the uncontrolled expansion of polyglutamine tract (group specific antigen - GAG repeat[20]) in the AR gene (x-linked), and is hence an exclusively male disease [113].

[20] Responsible for the coding of core protein structures.

Currently there is no treatment for the SBMA or any other polyglutamine - based disease (nine reported so far, including SBMA [114]), despite the numerous research studies either finished or on-going. However, many studies have shown encouraging, but not significantly conclusive, results in delaying the onset of the disease or improving the quality of life due to symptom suppression. Encouraging results were presented in the study by Banno et al, 2009 [115] showing improved swallowing and functional activities in patients, invigorated by a pre-clinical study on SBMA mice treated with Leuprorelin, a drug shown to reduce polyglutamine expansion and spinal cord inclusions, published by Katsuno et al, 2003 [116]. However, a repeat of the study in 2010 by Katsuno et al, did not have the same outcome with inconclusive results in terms of symptom suppression [117]. A clinical trial with the 5-α-reductase inhibitor dutasteride was also done, suggesting that preventing the conversion of testosterone to dihydrotestosterone (DHT) could have great benefits for the patients; however, the outcome out of a two year study was inconclusive [118]. More encouraging has been the study reported by Jochum et al 2012, which showed in an SBMA fly model reduction in polyglutamine oligomers by the administration of melatonin, [119]. More recently, a study reported by Malik et al 2013, showed significant improvement when Arimoclomol was used. Arimoclomol is believed to be promoting the re-folding of proteins and also discarding the toxic ones [111]. This drug has also shown to improve symptoms in patients with ALS [101, 107] and is currently in trials in the USA [120].

Since the SBMA disease is hereditary, the highest demand is not in diagnostic tools; a gene examination can verify the disease at pre-symptomatic stages. However, the demand is high in non-invasive biomarkers, which would help with disease progression monitoring and drug test response, both for pre-clinical and clinical studies. The CEST technique could possibly provide information related to the protein levels arising from the polyglutamine expansion in the spinal cord and brain stem of affected individuals.

5.3.2. Methods

Two groups of mice participated in the study, AR mutant mice, SBMA (n=12) and healthy controls (n=6). All mice were scanned at 10 months of age and repeat scans were performed at 12 months of age, [111]. Between 10 and 12 months, the SBMA mice received daily treatment: Half of the mice (n=6) were treated with Arimoclomol [107] and the rest of the group (n=6) were on vehicle treatment, given just saline instead. Arimoclomol was administrated daily via the intra-peritoneal (IP) route with a dose of 10mg/kg dissolved in saline. The specific two month period was chosen according to earlier studies by Anna Gray (PhD student, Institute of Neurology) on muscle tension of SBMA mice, showing how muscle force and weight decrease at maximum rates by 12 months of age. This implies that the 12 month time point is a characteristic disease stage before symptoms worsen. Following the second scan, mice were culled and spinal cords were extracted. Half of the mice per group were dedicated to protein quantifications (n=3 from controls and similarly from Arimoclomol treatment and saline treatment as well), section 5.1.3 . The rest of the mice were used for histological analysis for the purposes of a different study. No protein quantification was planned for the mice at 10 months as the study was longitudinal. However, due to the nature of the results (section 5.3.3), three control mice were added to the study, which were scanned at 10 months only and culled for protein quantification. Table 10 summarises the mice numbers per time point

	Control mice		**SBMA mice**			
			Arimoclomol		**Vehicle**	
Scan age	**10**	**12**	**10**	**12**	**10**	**12**
MRI scan	9	6*	6	6*	6	6*
Protein Quantification	3	3	---	3	---	3

Table 10: summarises the number of mice used for the purpose of the SBMA study, both for the CEST-MRI scanning and also the protein quantification. Where the star sign is indicated (*), mice were scanned for the second time.

The procedure for anaesthesia and mouse monitoring was identical to that for the SOD1 mouse study (methods section, 5.2.3).

All scans were performed on a horizontal 9.4T MRI scanner (Agilent Technologies) with a receive/transmit volume coil of internal diameter of 33mm (Rapid Biomedical).Mice were scanned in all three planes for voxel positioning (voxel size: 1x1x4mm^3) and the signal within the voxel was shimmed achieving a linewidth of 38 ±3 Hz. CEST scans were performed with parameters and setup as described in section 5.1.1. CEST data were acquired from the Lumbar enlargement, located between vertebrae T11-L1. The voxel location is illustrated in figure 64, shown in green.

Following spinal cord CEST acquisition mice were repositioned, this time aiming to scan the left calf muscle (between the ankle and the knee). Shimming was repeated (voxel size = 15x15x16mm^3), to about 50±3 Hz linewidth. Forty images of 0.4mm thickness (with no slice gap) were acquired with a fast spin echo multi slice (FSEMS) sequence placed between the knee and ankle, perpendicular to the calf bone as shown in figure 71 (Matrix size = 256x256, FOV = 15x15mm^2, TR=825ms, TE=25ms, NE= 8/excitation).

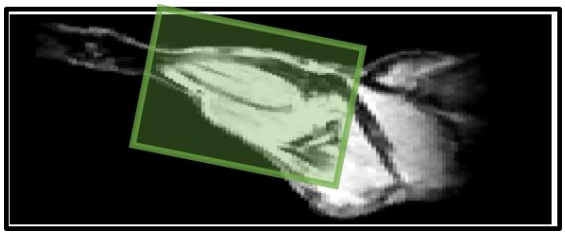

Figure 71: anatomical image of the mouse limb, sagittal orientation. The green box is an illustration of the shim voxel and the total area scanned with the FSEMS sequence for the volumetric study between the ankle (on the left) and the knee. The calf bone is shown in black within the green voxel.

All procedures described, were conducted under an approved protocol from the Home Office.

CEST data were post-processed as already described in section 5.1.2 and the peaks at 2 and 3.5mm (MTR values as described in equation 21) were calculated for all mice groups. In addition volumes of the lower (Right) limb were calculated by Anna Gray (PhD student, Institute of Neurology) using the anatomical images acquired.

5.3.3. Results & discussion

This section summarises the comparison of CEST to the post-mortem protein concentrations of the total soluble fractions found in the Lumbar region per mouse

group respectively (control and SBMA for 10 and 12 months of age). In addition the volumetric results of the lower limb, are also presented.

For the 10 month scan point, SBMA animals (n=12) are presented as the pre-treatment group, and later on (12 month scan point) the animals are presented in two separate groups depending on the treatment they received between the two months (Arimoclomol or vehicle respectively).

CEST versus total soluble protein levels

CEST analysed at 3.5ppm shows no significant differences ($p>0.05$) between healthy controls and SBMA mice, neither at 10 months of age (pre- treatment period) nor at 12 months (following a 2 month treatment/placebo period). All CEST values remain between 1.1-1.3 ± 0.17 percent. Figure 72 gives the results obtained from the CEST peak at 3.5ppm for all mice groups.

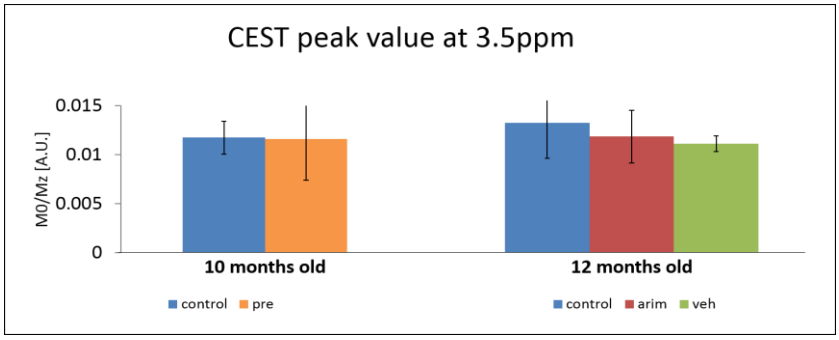

Figure 72: CEST peak value at 3.5ppm from water. The chart shows both age groups: 10 and 12 month of age for control (in blue) and SBMA mice each time (pre-treatment in orange, post-treatment in red and green for Arimoclomol and vehicle respectively). No significant differences of the CEST signal at 3.5ppm are observed between the groups. Mean values per group: 1.18±0.17 in healthy controls at 10 month of age. 1.16±0.42 in pre-treatment SBMA mice, 1.28±0.35 in healthy controls at 12 month of age, 1.14±0.26 in Arimoclomol treated and 1.07±0.08 in vehicle treated.

In addition, CEST was analysed at the frequency of 2ppm from water. As figure 73 describes, significant differences were observed ($p<0.05$) when comparing the control group of 10 months old with any of the other groups. The CEST analysis reveals an elevated signal of 0.87±0.04 percent compared to the signal observed from the rest of the mice which corresponded to 0.32±0.03 (pre-treated mice), 0.47±0.04 (12 month old controls), 0.52±0.04 (Arimoclomol treated) and 0.50±0.02 percent (vehicle treated). No significant differences were observed between healthy controls and SBMA affected

mice at 12 months of age. Also no significant differences were observed between mice with different treatment type (Arimoclomol or Vehicle).

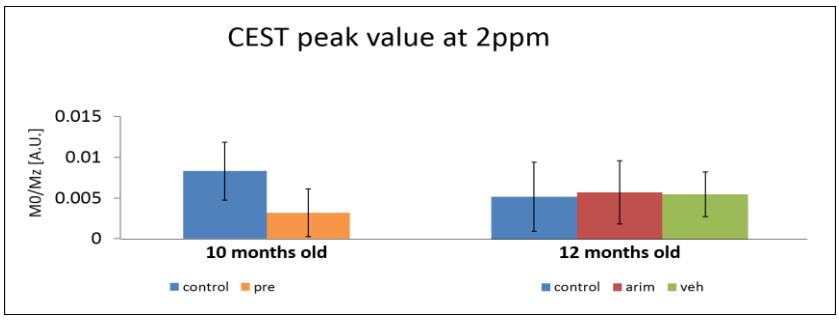

Figure 73: CEST peak value at 2ppm from water. The chart shows both age groups: 10 and 12 month of age for control (in blue) and SBMA mice each time (pre-treatment in orange, post-treatment in red and green for Arimoclomol and vehicle respectively), in the same way as figure 72. Significant differences (unpaired T test) were observed between 10 month old control mice and the rest of the groups (p<0.05). Mean values per group: 0.87±0.04 in healthy controls at 10 month of age. 0.32±0.03 in pre-treatment SBMA mice, 0.47±0.04 in healthy controls at 12 month of age, 0.52±0.04 in Arimoclomol treated and 0.50±0.02 in vehicle treated. No significant differences of mice at 12 months of age.

The unpredicted elevated 2ppm CEST signal of the 10 month old control mice, raised suspicion among the research group and cross-matching to protein soluble proteins was considered necessary. Therefore, three additional controls (mentioned in the study description, section 5.2.3) where added in the protocol. These mice were only scanned at 10 months of age and then sacrificed for protein quantification (all results already include the additional mice).

The following figures show the average Z-Spectra acquired from the mouse spinal cord at 10 (figure 74) and 12 (figure 75) months of age.

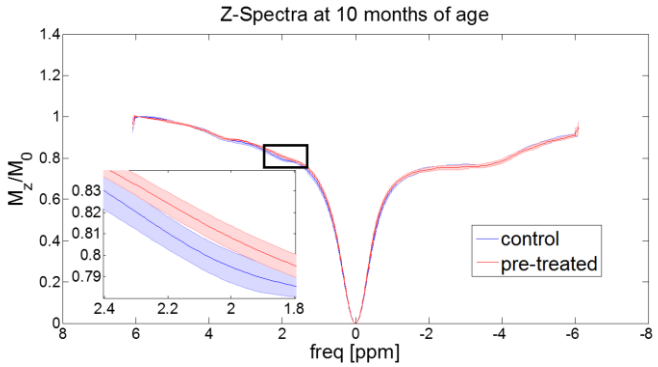

Figure 74: Averaged Z-spectra from the Lumbar enlargement of the spinal cord of healthy controls (in blue) and SBMA mice pre-treatment (in red). Significant difference (p<0.05) at 2ppm is observed between healthy and SBMA mice, however no significant differences are observed either at the amide peak (3.5ppm) or the aliphatic peak (-2.5 to -5 ppm).

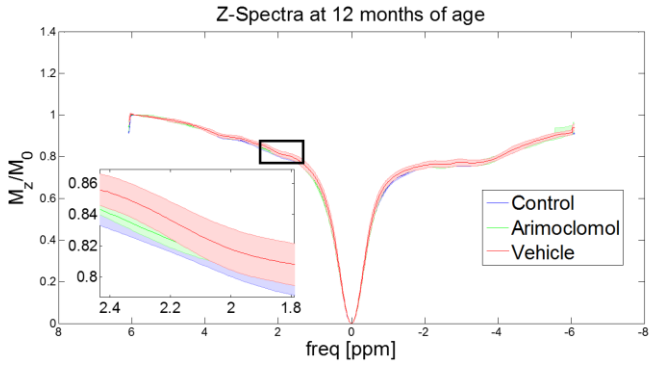

Figure 75: Averaged Z-spectra from the Lumbar enlargement of the spinal cord of healthy controls (in blue) and SBMA mice at 12 months of age, following daily treatment over a 2 month period (Arimoclomol treatment in green, and vehicle treatment in red). No significant differences are observed at any frequency point between the three groups.

The only significant difference is observed when comparing the Z-spectra of 10 months age (figure 74) between 1.8 and 2.2 ppm (centred at 2ppm, peak corresponding to Amines). This is the same results summarised by figure 73 but, as a more complete data set; here it is obvious that no significant differences are observed when comparing any other frequency offset, including the aliphatic frequency range. Similarly, figure 75 shows no significant differences at any frequency offset when comparing the Z-Spectra of mice at 12 months of age.

Total soluble protein levels quantified as described in section 5.1.3, are summarised in figure 76 for control mice at 10 month old as well as for control and treated mice at the 12 month scan point. No samples were taken from the SBMA mice at 10 months of age (pre-treatment stage) as mice were kept alive until their 12 month. Results show significantly ($p<0.05$) increased protein concentration (17.3±0.9 mg/ml) in healthy controls at 10 months of age compared to the protein concentrations at 12 month of age for all the groups: 15.3±0.03 mg/ml (healthy controls 12 months old), 14.6±0.3mg/ml (Arimoclomol treatment) and 13.4±1.3mg/ml (vehicle treatment).

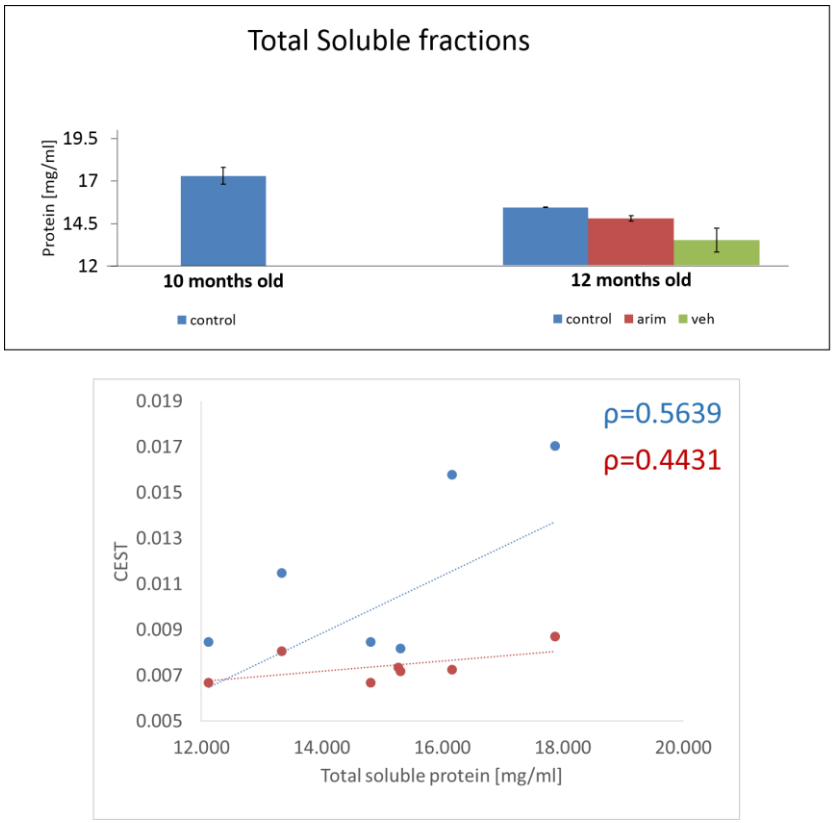

*Figure 76: Total soluble protein concentrations in the spinal cord of mice quantified by protein assays (**top figure**). The chart shows both age groups: 10 and 12 month of age for control (in blue), post-treatment in red and green for Arimoclomol and vehicle respectively); same colour code as figures above. Significant differences (unpaired T test) were observed between 10 month old control mice and the rest of the groups (p<0.05). Mean values per group: 17±0.9 mg/ml (healthy control of 10 month age). 15.3±0.03 mg/ml (healthy controls of 12 months age), 14.6±0.3 mg/ml (Arimoclomol treatment, SBMA mice) and 13.4±1.3 mg/ml (vehicle treatment, SBMA mice). No significant differences between mice at 12 months of age. **Bottom figure** the relationship of CEST with soluble protein levels at 2ppm (in blue) and 3.5ppm (in red). Pearson's correlation (no significance, p<0.1 for both relationships) assuming two-tailed test (n=7). See also Appendix F.*

The total soluble protein fractions (post mortem) in figure 76 agree with the CEST results at 2ppm frequency offset (in vivo) in figure 73. In a similar manner, the CEST signal and the soluble proteins correspond to high values at 10 months of age for the control group, which seem to decrease two months later (month 12 of the same control group). This is quite an unforeseen result as one would expect no significant differences in control mice between the age of 10 and 12 months. Indeed changes do occur during normal aging and degeneration processes cause protein levels to decrease within the spinal cord of otherwise healthy individuals [121, 122] , but mice at 10 or 12 months old are not considered to have different physiology. A typical laboratory mouse has a life span of about 2-3 years [123], thus between 10 and 12 months of age mice are considered young adults. While stating that, no reference could be found on the expected protein levels of healthy mice at these two age points.

Additionally, no significant differences were found with the CEST technique between mice groups at 12 months of age, verified by protein assays supporting no significant differences in protein concentrations between the same groups. Finally regarding the treatment, no significant changes were observed between Arimoclomol and vehicle treated mice ($p>0.05$) neither with the CEST technique nor through protein assays.

Lower limb volume with disease onset

The following results were analysed by Anna Gray (PhD student, Institute of Neurology) and data were collected by myself and Francisco Torrealdea (PhD student, Institute of Neurology) during the SBMA spinal cord study. These data were considered as an additional way of controlling for the treatment period. Figure 77 summarises the calculated volumes obtained by the muscle structural imaging. Volume calculations were done by manually drawing regions of interest around the muscle (excluding bones) and summing the areas for all slices between the knee and the ankle of the mouse limb.

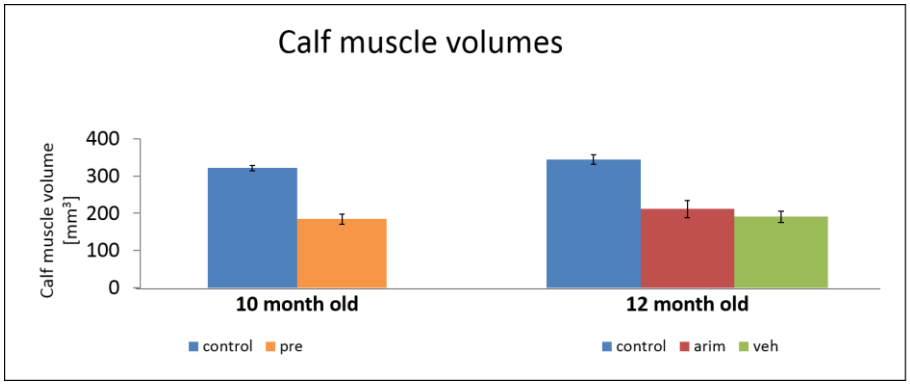

Figure 77: Volume of lower limb muscle measured form the left leg of mice (between the ankle and knee). The chart shows both age groups: 10 and 12 month of age for control (in blue), post-treatment in red and green for Arimoclomol and vehicle respectively); same colour code as figures above. Significant differences were observed between healthy controls and SBMA mice per age groups ($p<0.001$). Mean values per group: 331.39±13.78 mm^3 (healthy control of 10 month age), 184.16±13.61mm^3 (SBMA pre-treated, 10 months old), 332.6±23.66mm^3 (healthy controls of 12 months age), 204.53±44.57mm^3 (Arimoclomol treatment, SBMA mice) and 184.54±28.88mm^3 (vehicle treatment, SBMA mice). No significant differences were observed in muscle volumes between healthy controls at 10 and 12 months of age.

No significant differences ($p>0.05$) were observed between healthy controls of 10 and 12 months of age, while highly significant differences were noted between healthy controls and SBMA mice at the same ages ($p<0.001$). As for CEST and protein

concentrations regarding the treatment, no significant changes were observed in muscle volumes between Arimoclomol and vehicle treated mice ($p>0.05$).

5.3.4. Conclusions

CEST measurements at 2ppm (Amine range) were found to agree with protein concentrations within the spinal cord of mice. The amine range is usually associated with smaller proteins and amino acids which allow a faster transfer rate with water. No differences were found in the Amide range (3.5ppm) or the aliphatic range (centred at -3.5ppm), which could be an indication of no changes in long chained proteins (slower exchange rates).

In addition, all means of measures (including CEST, protein assays and volumetric analysis) revealed no significant changes between treated (Arimoclomol) and non-treated (vehicle) mice, suggesting that either the drug, the dose or length of treatment was not the optimum.

Despite the unexplained differences between healthy controls at the two scan points, it is very encouraging to observe the trend between the 2ppm CEST measurements and the post-mortem protein fractions. To our knowledge, this is the only study performed in the spinal cord of mice relating CEST to the soluble protein levels.

5.4. General Chapter Conclusions

Chapter 5, includes a description on the implementation of spine CEST of in-vivo disease assessment in mice. The mouse spinal cord is a challenging region to scan, due to the highly inhomogeneous fields, physiological movement and small size. Thus reproducible results from the spine are already considered as a significant achievement.

This chapter also includes two studies, a fast disease onset mouse model of ALS, prone to the accumulation of SOD1 proteins in the spinal cord and also a slow disease onset mouse model of SBMA, prone to the accumulation of polyglutamine expansions in the spinal cord and brain stem. Both diseases are characterised by the accumulation

of protein in the process of aggregate fibril formation, thus were thought to be good candidates for validating the CEST technique.

The SOD1 study gave inconclusive results regarding the detection of differences between healthy controls and SOD1 affected mice with the CEST technique. Nevertheless the results were not discouraging due to the fact that protein assays match the CEST results by also giving no differences between groups.

The SBMA study was conducted following the inconclusive results of the first study, with the aim of shedding some light on whether the CEST technique is appropriate as a biomarker in neurodegenerative diseases. The results revealed that, despite the absence of significant differences between different treatments of SBMA affected mice, differences were observed with the CEST technique between healthy controls and sick mice at the pre-symptomatic stage (10 months of age). These findings were also supported by protein assays, revealing a linear trend between the CEST signal and the soluble protein concentrations for the two mice groups.

In summary, this chapter demonstrates encouraging results demonstrating that it may be possible to associate protein concentrations in the spinal cord to CEST measurements. To our knowledge this is the first time CEST signal was correlated with quantified protein concentrations within the spinal cord. Reliable and reproducible non-invasive biomarkers in neurodegenerative diseases are still in high demand and a method such as CEST could possibly help in monitoring disease progression and drug testing in the future.

Chapter 6. Brain pH mapping

This chapter is focused on the implementation of CEST as a measure of pH in the piglet brain in a model of Hypoxic Ischemic Encephalopathy (HIE). Following HI, the brain undergoes dramatic metabolic disturbances leading to alterations in tissue pH. Change of tissue pH is a good early biomarker of the severity of the condition; therefore it is important to develop techniques that track brain pH changes. [124, 125]. ^{31}P NMR allows quantitative pH measurements, however the technique only provides at best limited spatial information [126, 127] and in addition multinuclear capabilities are not widely available in the clinic due to the added costs incurred, therefore ^{31}P measurements are not as widely possible as ^{1}H ones. To achieve the aims of higher spatial resolution and more general applicability, CEST was considered as a potential alternative technique. The sensitivity of CEST to pH has been reported in various papers as discussed in section 1.1 and has also been demonstrated in the phantom chapter (section 4.3). Thus this project aims at developing a method for non-invasive mapping of regional pH in the neonatal piglet brain undergoing HI using CEST-MRI.

6.1. Introduction

HIE in the newborn infant is associated with high mortality and morbidity rates worldwide with a prevalence of 4 in 1000 neonates suffering asphyxiation before or at birth resulting in neonatal encephalopathy (NE). NE has a survival rate of 40% of which at least 25% suffer long term neurodevelopmental sequelae such as cerebral palsy[21] or other severe disabilities (including deafness, blindness, epilepsy, global developmental delay, autism, as well as cognition, memory and fine motor skill problems), [128, 129, 130] & [131]. A well-established piglet model of HIE has recurrently been used over the past 20 years [132, 133, 130] & [129] for the study of NE. Newborn piglets are similar to neonates regarding the brain size, vasculature and

[21] A motor condition which causes physical disabilities in human development.

maturity levels [126, 129]. Due to these similarities, all other life monitoring equipment used (apart from the MRI scanners) for piglet experiments are identical to hospital equipment, resulting in direct clinical translation of new treatments to neonates.

Currently mild hypothermia[22] is the most frequent, and effective-proven treatment in neonates suffering NE [128]. However, the neuroprotective success rate with this method is 2 in 7 babies [134], suggesting the need for additional treatments to produce a synergistic effect along with hypothermia treatment. As crucial as the development of a new treatment is, advanced monitoring methods are also of great need in order to assess treatment effectiveness in animal models and eventually in the clinic.

Among the different biomarkers investigated for assessing HIE is tissue pH. It is known that metabolic acidosis is observed during prolonged asphyxia. Studies in rodents suggest that alterations in pH continue to occur even days after HIE, indicating overall alkalosis or further acidosis in the brain [135, 136]. However the detection of regional pH changes is currently either time consuming, with limited spatial resolution [137, 126] or requires invasive technology [138].It is therefore of great importance to develop non-invasive pH mapping techniques offering higher resolution within a reasonable acquisition time. Toward this goal, CEST is investigated as a potential neuroimaging technique to better understand ischemic tissue by looking into the signal changes due to pH alteration.

6.2. Experimental procedures

Newborn male piglets (n=16), aged <24h, were surgically prepared and placed in the MRI scanner (9.4T Agilent Technologies, bore diameter 305mm). Surgical preparation is briefly described in section 6.2.1 (animal preparation); a more extensive description of the surgical procedure can be found in Lorek et al 1994, [132]. HI was induced by occlusion of both common carotid arteries (ischemia)[23] and reduction of inspired oxygen fraction to 6% (hypoxia). ^{31}P MRS was acquired at baseline (10 minutes),

[22] Gradual reduction of the body core temperature to 33.5^{o}C for a period of about 72 hours.
[23] Partial ischemia due to the physiology of the piglet brain as the middle cerebral artery is not occluded

during HI and for 1 hour afterwards with 1 minute time resolution using an elliptical ^{31}P-tuned surface coil (6.5x 5.5cm). Description of the ^{31}P protocol is found in section 6.2.3. During HI the inspired oxygen fraction was titrated in order to maintain the height of the nucleotide-triphosphate (NTP) signal on the ^{31}P MRS between 30% and 40% of the baseline value for 12.5 minutes [131]. CEST scans were acquired at baseline (before HI), 1 hour after initiation of HI and (for piglets that survived) at 24h post HIE [61] with a volume transmit coil of internal diameter 150mm and an elliptical surface transmit/receive coil with dimentions 6.5cmx5.5cm (Rapid Biomedical); the CEST protocol is described in section 6.2.2. In addition, blood samples were taken at all scan points, which were used for physiological monitoring and to obtain measurements such as blood pH, glucose and lactate levels. All animal experiments were performed under an approved UK Home office protocol.

6.2.1. Animal preparation

Animal surgery and monitoring was performed by the preclinical neonatal neuroprotection research group, led by Prof Nicola Robertson (Institute for Women's Health): Dr Kevin Broad (post doctoral research fellow), Dr Go Kawano (neonatologist), Dr Mojgan Ezzati (neonatologist), Dr Igor Fierens (intensivist), Dr Jamshid Rostami (surgeon) and Dr Daniel Alonso Alconada (research associate).

Initial sedation was achieved by intramuscular midazolam (0.2mg/kg) and 4% v/v isoflurane given through a face mask for tracheostomy and intubation. Piglets were ventilated to maintain partial oxygen pressure (PaO_2) at 8-13kPa and carbon dioxide ($PaCO_2$) at 4.5-6.5kPa. A venous catheter (umbilical) was placed for fluid infusion (10% dextrose, 60/ml/kg/day), fentanyl (3-6µg/kg/h) and antibiotics (benzylpenicillin 50mg/kg and gentamicin 2.5mg/kg, both every 12 hours). Heart rate and blood pressure were monitored by an arterial catheter (umblilical); arterial blood pressure was maintained higher than 40mm Hg with infusions of inotropes and colloid (Gelofusin, B Braun Medical Ltd). Animals also received arterial infusion of 0.9% saline solution (1ml/hour).

Both common carotid arteries were isolated (at the same level as vertebra C4-fourth Cervical) and remotely controlled vascular occludes (OC2A, in-vivo Metric) were

placed around them. During the surgical procedure isoflurane was maintained at 3% and for the rest of the experiment at 2%. Body temperature was monitored with a rectal temperature probe and maintained at 38.5^{o}C with a hot water blanket system (SAII instruments). All animals were continuously monitored and received intensive care throughout the experiments.

6.2.2. CEST protocol

The CEST protocol was optimised and tested by Francisco Torrealdea (PhD student, Institute of Neurology) and myself. CEST data were acquired by Dr Alan Bainbridge (Clinical scientist, UCLH), Dr David Price (Clinical scientist, UCLH), Miss Magdalena Sokolska (PhD student, Institute of Neurology) and myself.

The CEST acquisition used during the HIE experiments consisted of 80 Gaussian shaped saturation pulses. Each pulse was applied for 50ms (with 5ms inter-pulse delay) with a FA=540^{o}, equivalent to 0.9μT mean amplitude. Saturation was followed by a GE readout with TE=2ms (minimum allowed by the 305mm gradient set) and TR_{RO}= 4.1ms (section 4.2.2.1). Phase encoding during readout was chosen to be of centric order (section 3.1.3), matrix size 128x128 with FOV = 80x80mm^2, thickness=4mm (number of slices= 3). Prior to the readout, no inter-pulse delay was added in order to maximise the CEST contrast achieved. The CEST sequence was repeated for 77 frequency offsets ranging between ±6.08 ppm centred at water with steps of 0.16 ppm (64 Hz at 9.4T). Frequencies were alternated from positive to negative to compensate for any potential B_0 field drifts, starting from the furthest positive point (+6.08ppm) and continuing all the way to 0 ppm. Total TR per frequency (TR_{tot}) was 4441ms. Figure 34 shows a schematic of the CEST sequence used. In addition reference images were acquired (at frequency 200ppm from water) with the same FOV for registration and normalisation purposes. Shimming was performed on a voxel covering the FOV within the brain achieving a linewidth of <20Hz for all the experiments.

CEST slice positioning

As the experimental procedure was designed to collect both CEST data and ^{31}P spectra, it was necessary to switch RF coils for each part of the experiments. In addition, at the end of the first day the piglet was taken back to the lab for overnight monitoring and returned the next day for further scanning. Thus, there was potential for the animal to have considerable positional shifts between scan points, and registration was mandatory prior to CEST processing. In addition, a single CEST slice required 5.7 minutes and as a consequence a limited number of slices were acquired per scan (three in total). Therefore it was crucial for the animals to be repositioned as accurately as possible for all scans, in a reliable and reproducible way.

Positioning scans were acquired in all planes. In the coronal plane, the CEST FOV was placed with an angle such that it was perpendicular to the midline of the brain (midline of the brain is indicated with light blue in figure 78). In the sagittal plane, the central slice was chosen (i.e.: the slice in which the spinal cord appears thickest) and the FOV was placed precisely in the middle of the brain in order to include the basal ganglia and the cortical area within the three slices [139].

Figure 78 illustrates the FOV in all three planes (coronal, sagittal and axial in a, b and c respectively).

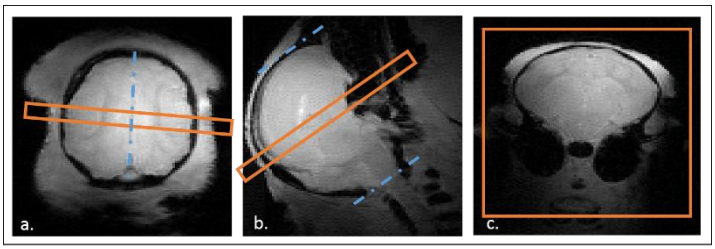

Figure 78: Illustration of the FOV used (shown in orange) for the piglet CEST experiments FOV is shown in all three planes: coronal (a), sagittal (b) and axial (c).

CEST data processing

CEST data were imported into Matlab for post processing and images were sorted according to the frequency offset from -6 to + 6 ppm. The three slices acquired per time-point (baseline, 1 hour and 24 hours after HI) were used for registration purposes; only the slice corresponding to the middle of the brain was used for further analysis. Time-points of 1 and 24 hours post HIE were registered to the baseline images. Registration was performed manually by selecting at least six similar points per image applying a global transformation to all the pixels (translation and rotation of the images, with no distortion correction). Assuming stability of the piglet throughout the CEST acquisition, the same transformation was applied for the entire Z-Spectrum.

Pixel by pixel fitting (smoothing spline function) was performed along the frequency offset dimension, following registration. Data were further interpolated to 1001 points (increase of the Z-Spectra resolution from 0.16 to 0.012 ppm) and normalised to the reference images (200ppm).

CEST of Amide groups (APT) has been reported as pH dependent via the exchange rate through a base-catalysed relationship (equation 15 and Section 2.3), [9]. The APTasym (MTRasym at 3.5ppm, as described in section 3.2, equation 22), is more often used for pH-weighted images. However, this method is highly weighted by the negative side (aliphatic range) of the Z-Spectrum and although not sensitive to pH, it can vary with concentration and different folding states of the proteins [82, 140]. In addition the inherent signal mainly of the aliphatic range is of much higher value than the APT signal change due to pH, making the visual presentation not as clear as it could be. Figure 79 shows the same data set (case a from group A, section 6.3) analysed at 3.5ppm looking at the height of the peak (APT*, top set of images) compared to the APTasym (bottom set of images).

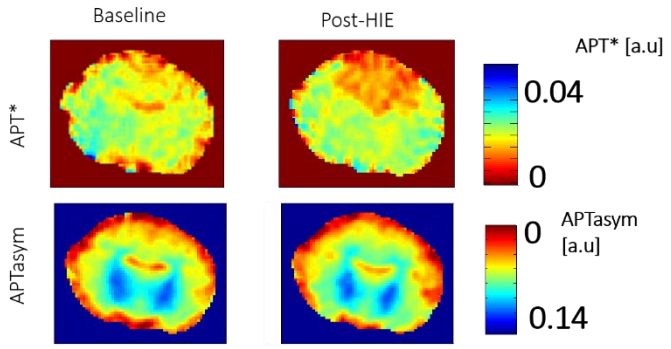

Figure 79: Illustrative data set analysed with the APT method (top pair of images) and with the APTasym method (bottom pair). Units are arbitrary, corresponding to the height of the peak and value of the Z-Spectrum asymmetry respectively. From the two pairs it is clear that the APT* method is not contaminated by the anatomical features of the brain.*

Therefore for the investigation of pH, CEST data were analysed by measuring the height of the Amide peak (APT*) at 3.5ppm (described in section 3.2). Figure 80 shows the behaviour of Amide peak under HIE in the cortical region of piglet bran, indicating reduction of the peak.

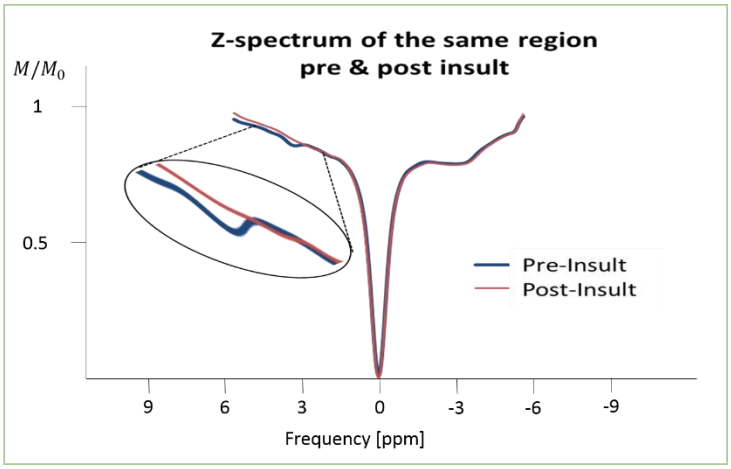

Figure 80: Demonstrative data from cortical region ROI of a piglet undergoing HIE (pH_i =5.7 post HIE). In blue the baseline (pre-insult) and in red 1hour post HIE. This figure illustrates how the amide peak (in circle) 'disappears' following HIE. This behaviour is compatible with exchange rate reduction due to pH decrease (equation 15).

6.2.3. ^{31}P MRS protocol

^{31}P MRS protocol was optimised and tested by Dr Alan Bainbridge (Clinical scientist, UCLH), [141]. Spectra were acquired by Dr Alan Bainbridge (Clinical scientist, UCLH), Dr David Price (Clinical scientist, UCLH) and Miss Magdalena Sokolska (PhD student, Institute of Neurology).

The ^{31}P MRS data were acquired with an elliptical transmit/receive surface RF coil (diameter 10cm) with a single pulse acquisition (hard pulse). TR = 10s, six repetitions (NR), giving a temporal resolution of 1 minute per acquisition. No voxel selection was used; the signal was acquired from the sensitive volume of the RF coil (see section 6.2.4). Shimming was done globally with the ^{1}H surface RF coil used during the CEST acquisition (section 6.2.2), achieving a linewidth of <20Hz.

^{31}P MRS data processing

^{31}P MRS data were analysed by Dr Alan Bainbridge and myself [141] using Advanced Method for Accurate, Robust and Efficient Spectral fitting (AMARES) and prior knowledge data as described by Vanhamme et al 1997, [142] as implemented in the jMRUI software [143].

The NTP multiplet structure was fitted according to prior knowledge data; α- and γ-NTP were fitted to doublets and β-NTP to a triplet. NTP consists of 70% of Adenosine triphosphate (ATP) as reported by Mandel & Edel-Harth in 1966, [144]; thus the NTP changes mainly reflect changes in ATP, [141, 145]. Inorganic Phosphate (Pi) was fitted with four separate components and Phosphocreatine (PCr) with a single component.

Intracellular pH (pH_i) was quantified using the Henderson-Hasselbalch equation [124], given below (equation 28).

$$pH_i = 6.67 + log_{10}\left(\frac{\delta - 3.29}{5.68 - \delta}\right) \quad (28)$$

where δ is the chemical shift between Pi and PCr peaks, as also shown in figure 81. Pi peak was calculated as the weighted average (peak shift multiplied by the square of the amplitude) chemical shift of all four Pi peaks such as shown in equation 29 below.

$$Pi = \frac{\sum_j f_j . A_j^2}{\sum_j A_j^2} \quad (29)$$

where f_j is the chemical shift and A_i the corresponding amplitude for each peak [141, 126].

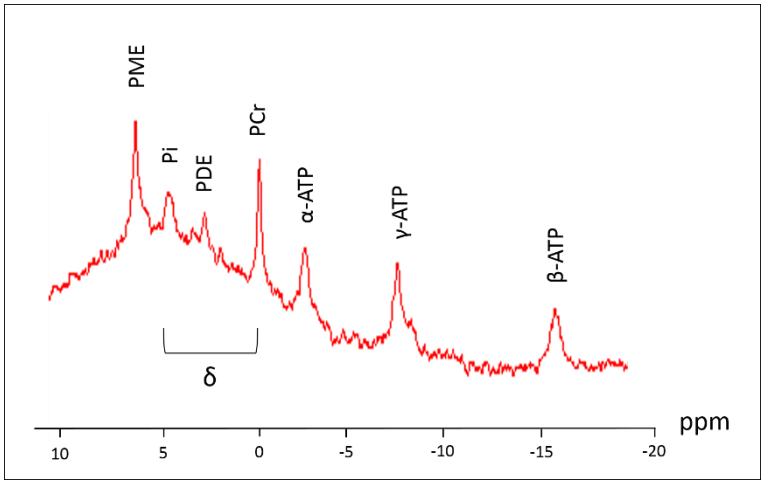

Figure 81: Expanded ^{31}P MRS spectrum of the piglet brain (baseline acquisition), illustrating the peaks and the Pi-PCr shift (δ) from which the pH_i is quantified. Note that ATP changes mainly reflect to NTP changes as explained above.

6.2.4. Comparison of CEST data to ^{31}P MRS

A phantom with pure Orthophosphoric acid (H_3PO_4) was scanned in order to identify the sensitive volume of the phosphorous RF coil. The phantom was of similar size and loading [24]to the piglet head for a better approximation of the source signal of ^{31}P MRS data.

A 3D-gradient echo sequence was used with TR=10s and TE=1.5ms (set to the minimum possible). FOV was 100x100x100mm^3 and matrix size 64x32x32, giving a spatial resolution of 1.56x3.125x3.125mm^3.

Figure 82 demonstrates the phosphorus signal in three planes (xz, yz and xy). The sensitive volume of the phosphorous coil was found to cover only the top cortical area of the brain (as shown in figure 83) with 85% of the signal calculated to reach penetration depth of 31.25mm (from pixel 10-30 in planes X-Z and Y-Z).

[24] Loading was achieved by adding salt to the solution and comparing with a piglet brain loading profile using a network analyser (Agilent technologies)

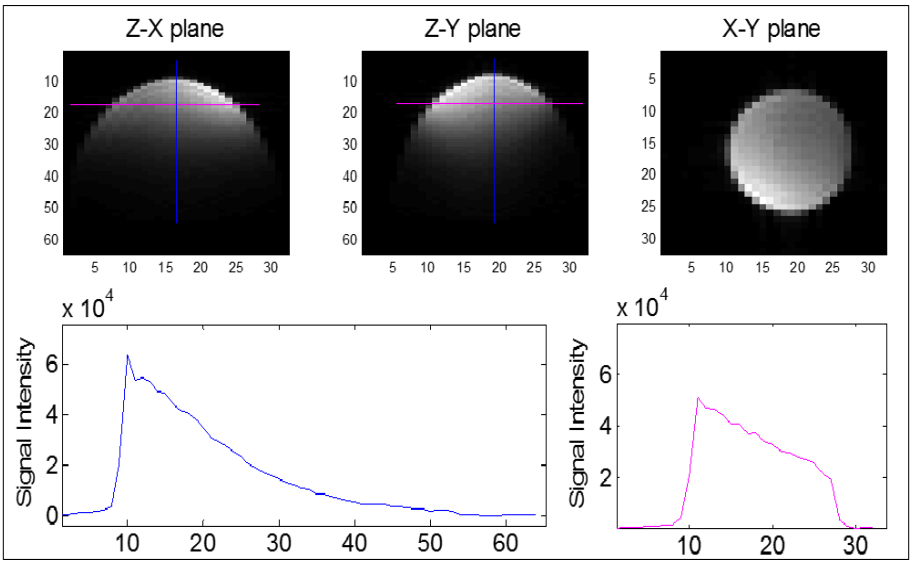

Figure 82: demonstration of the phosphorous signal origin in three planes (xz, yz and xy). The signal intensity graphs are colour coded; graph on the left (in blue) corresponds to the signal intensity in the Z direction and graph on the right (in pink) corresponds to the signal intensity in the xy plane, as illustrated in the images.

The CEST signal was therefore averaged in this area, in order to best match the source tissue of the two pH measurements, as demonstrated in figure 83.

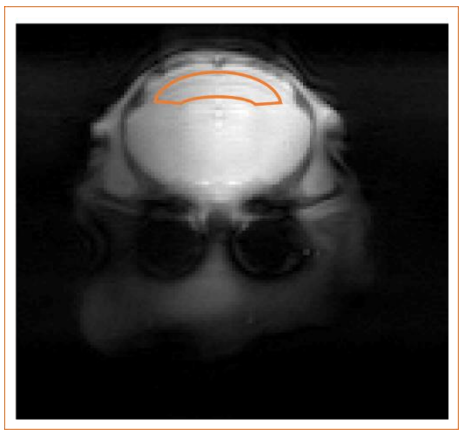

Figure 83: Axial image of the piglet brain showing the area in which the CEST signal was averaged (in orange).

Despite the APT* reflecting the exchange rate changes due to pH alteration, it is not a direct quantitative measurement. To further understand the APT* measurement when only pH is changed (according to equation 15), data were simulated using a four pool model derived from the Bloch-McConnell equations (section 2.4). The simulation was repeated three times for different T1 values (1480, 1850 and 2200ms) to investigate the APT* value change. The rest of the parameters used were kept the same and are summarised in table 11 below.

Pool No.	Frequency [ppm]	Pool size (ratio to water)	T_1 [ms]	T2 [ms]
1 (Water)	0	1	1480, 1850, 2220	37
2 (Amine)	2	0.0025	1500	10
3 (Amide)	3.5	0.0017	1500	10
4 (Aliphatic)	-3.5	0.04	260	0.3

Table 11: Summary of the parameters used per pool for modelling the piglet brain.

6.2.5. Comparison of CEST data to ^{1}H MRS

^{1}H MRS protocol was optimised and tested by Dr Alan Bainbridge (Clinical scientist, UCLH). Spectra were acquired by Dr Alan Bainbridge (Clinical scientist, UCLH), Dr David Price (Clinical scientist, UCLH) and Miss Magdalena Sokolska (PhD student, Institute of Neurology), part of the HIE experiment. ^{1}H MRS were acquired 48 hours post-HIE on the surviving piglets. All the analysis was done by Dr Alan Bainbridge and ratios of Lactate/N-acetylaspartate (NAA) are used here for comparison to APT*.

The protocol is described by De Vita et al 2005 [146]. Briefly, ^{1}H MRS data were acquired with a LASER (Localisation by adiabatic selective refocusing) sequence [147, 148], with VAPOR water suppression [149]. TR=5000ms, TE= 288ms and spectral bandwidth of 4006 Hz. Two voxels were acquired as illustrated in figure 84, in the cortical region (green) and thalamic region (blue). Comparison data for the available piglets are demonstrated in the results section.

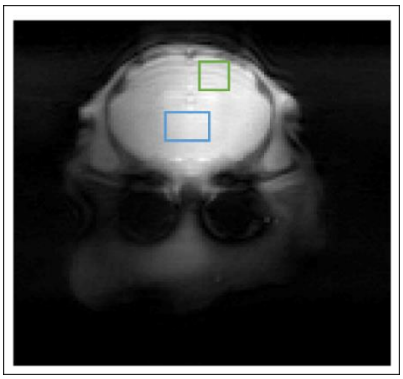

Figure 84: Axial image of the piglet brain showing the two voxels used for ^{1}H MRS. Cortical region (in green) and thalamic region (in blue).

6.2.6. Piglet categorisation

Piglets were categorised in two groups depending on the outcome of the insult characterized by the summation of the β-NTP peaks (three β-NTP peaks in total). Piglets in which the β-NTP peak height failed to recover to at least 75% of its baseline were considered as *not fully recovered* and placed in group A, while the rest cases were classified as *fully recovered* and placed in group B. The percentages were calculated by averaging the β-NTP amplitude value at baseline (10 spectra in total), comparing them to the average amplitude value of the last 10 spectra at 1 hour post HI. Figure 85 shows examples of a *fully recovered* HIE piglet case (left graph) and a *not fully recovered* HIE piglet case (right graph).

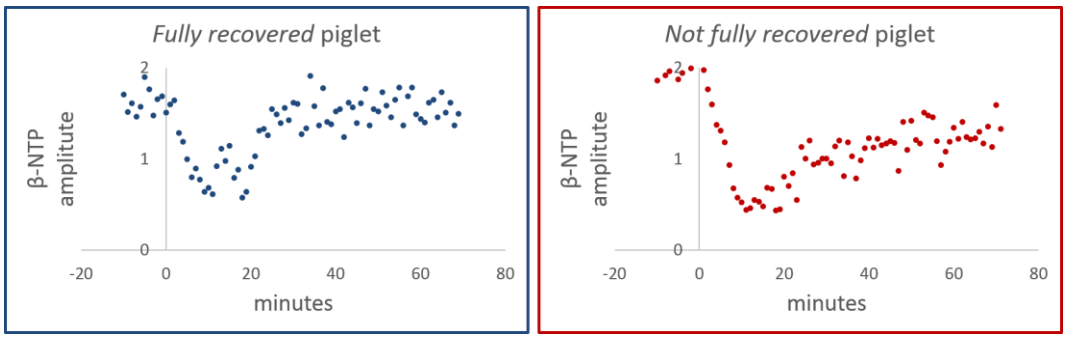

Figure 85: the β-NTP evolution in time for two piglets. On the left (in blue) the β-NTP peak recovers to 94% of the baseline; the piglet' HI is considered fully recovered (group A). On the right (in red) the β-NTP peak recovers to 61% of the baseline; the piglet' HI is considered not fully recovered (group B) in this case. 10 spectra were acquired at baseline (10 minutes in total). Time zero corresponds to the start of the insult. Once the β-NTP peak reached 40% of the baseline, it was maintained for 12.5 minutes (12 spectra acquired during this period). The rest of the time-points correspond to 1 hour of scanning during the recovery period (60 spectra).

6.3. Results & Discussion

Out of sixteen piglets that were part of this study, seven were classified as as group A cases (shown in figure 86) and the rest as group B cases (shown in figure 87), characterised as described in section **Error! Reference source not found.**. Figures 86 and 87, show the value of the APT peak height (APT* at 3.5ppm) from the three scan-points (baseline, 1 hour post-HIE and for the piglets that survived 24 hours post-HIE). Throughout the experiments, APT* values ranged from 0 to 0.04 [arbitrary units (a.u.) of the peak height] with 0.04 giving the most defined peak and 0 giving no peak (similar to figure 80).

Cases are compared to Arterial blood gas levels of lactate, glucose, and pH values. Lactate provides additional proof of poor tissue oxygenation and possible cell damage [150]. Similar to lactate, serum pH levels also provides information on acidosis; if serum pH values are lower than 7.35 and are combined with high lactate levels, hypoxia is assumed [151, 152].

Group A HIE cases

A clear reduction in the APT signal is observed following HI in six out of the seven cases of group A. Although the piglets suffered global HI, it is clear from figure 86 that the APT signal patterns in the brain are localised. Specifically, cases a-e show signal drop in the cortical area (from mean baseline value 0.018±0.002 reduced to 0.011±0.005), on data acquired 1 hour post-HI. The cortical area is known to be extremely sensitive to ischemia; 5 minutes of oxygen and blood restriction is enough to damage pyramidal neurons within the cortex, leading to apoptosis [153], chapter 2]. Cases f & g show decrease of the APT signal across the entire brain 1 hour post-HI. The two animals did not survive for the 24 hour post-HI scan, suggesting they suffered more protracted HI compared to the rest of the cases. More severe HI results in damage of the neurons in the thalamic area, brainstem, and eventually the entire brain [153], chapter 2 & [154], leading to a complete and irreversible brain function loss [155]. Arterial blood measurements of Lactate levels also confirm the greater severity in these two animals with higher concentrations than normally expected (11.73 and 12.07 mM respectively); the mean value of Lactate across all animals at 1

hour post-HI was measured to be 4.36±1.24mM. Figure 88 (top figure) outlines the mean values of Lactate levels.

It is also worth noting that the baseline APT images were generally flat compared to the post-HI images (mean APT* value = 0.018±0.002), suggesting no changes in the APT peak across the brain before HI. However, the baseline APT image of case g shows unexpected contrast between the left and right hemispheres: left hemisphere gives a mean APT* value of 0.012 while the right hemisphere 0.028. The elevated blood lactate levels (7.7mM when 2.87±1.41mM mean Lactate concentration at baseline) of this specific piglet leads to the conclusion of the potential presence of brain damage prior the induction of HIE (either during the surgical operation, or even during birth). Such damage might be able to explain the left-right difference in APT* shown in this piglet.

Group B HIE cases

Animals considered as fully recovered (group B) are summarised in figure 87. Similarly to cases of group A, APT* measured 1 hour post-HIE is decreased compare to the baseline. Particularly in cases b, c, d & f, the APT* signal is decreased in the cortical area (as seen in cases a-e in group A). Furthermore, blood lactate levels measured 1.5 hour post-HIE in these four cases indicate levels higher than the average (5.99, 6.74, 6.47 & 5.02 mM respectively), with levels similar to group A exhibiting analogous APT* images. This might suggest that while the piglets recovered in terms of the NTP peak 1 hour after HIE, the APT technique can provide contrast which might be related to the irreversible cell damage caused during insult [156]. On the contrary, APT* images corresponding to animals g, h & i show on average flat response, with no signal decrease 1 hour post ischemia. The very low lactate values corresponding to the three cases (1.76, 2.05 & 1.75 mM respectively), might relate to a lesser brain injury due to HI.

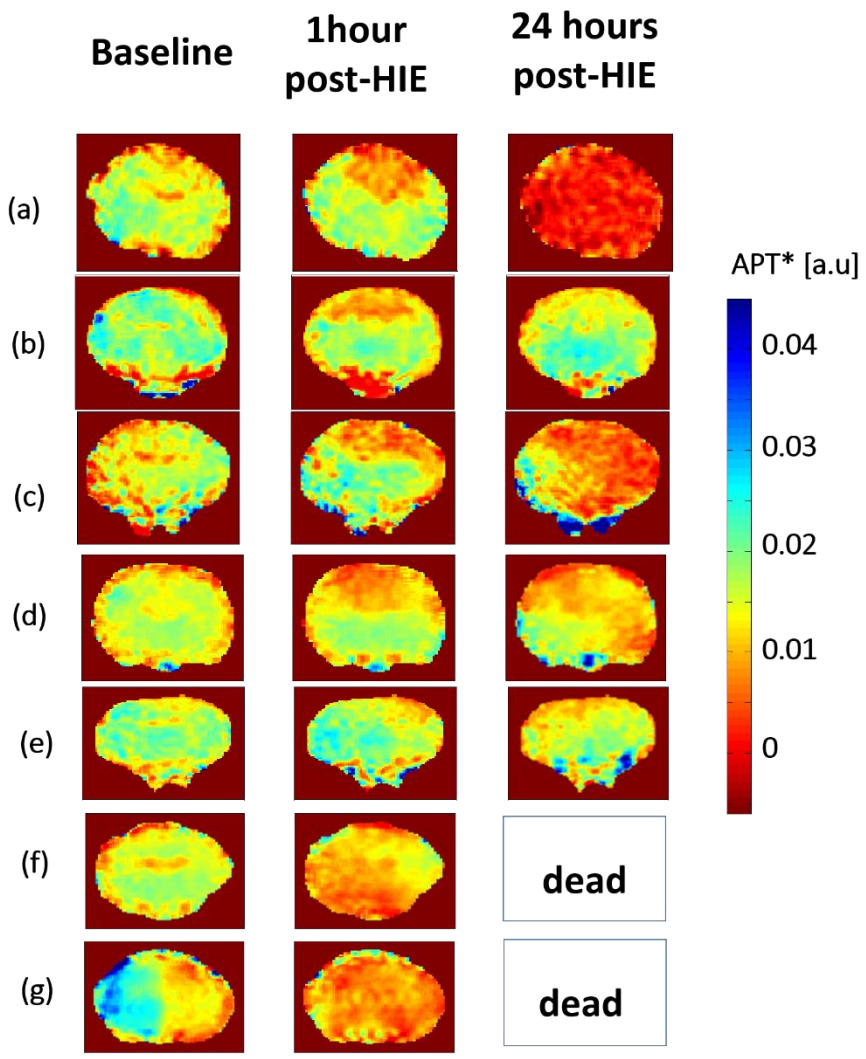

Figure 86: GROUP A: Summary of all HIE cases (a - g) characterised as 'not fully recovered. Images correspond to the APT value (height at 3.5ppm) for the baseline, 1 hour and 24 hours post-HIE. The APT* scale ranges between 0-0.04 units of height of the Z-Spectra analysed per pixel. Where no image is shown, experiment was terminated due to the animal's death. Cases a-e present APT* maps of reduced signal compared to the baselines, localised in the cortical area. Cases f & g show APT* maps less localised but with reduced signal in the entire brain compared to the baseline scans. Animals of cases f & g did not survive for the 24h post-HIE.*

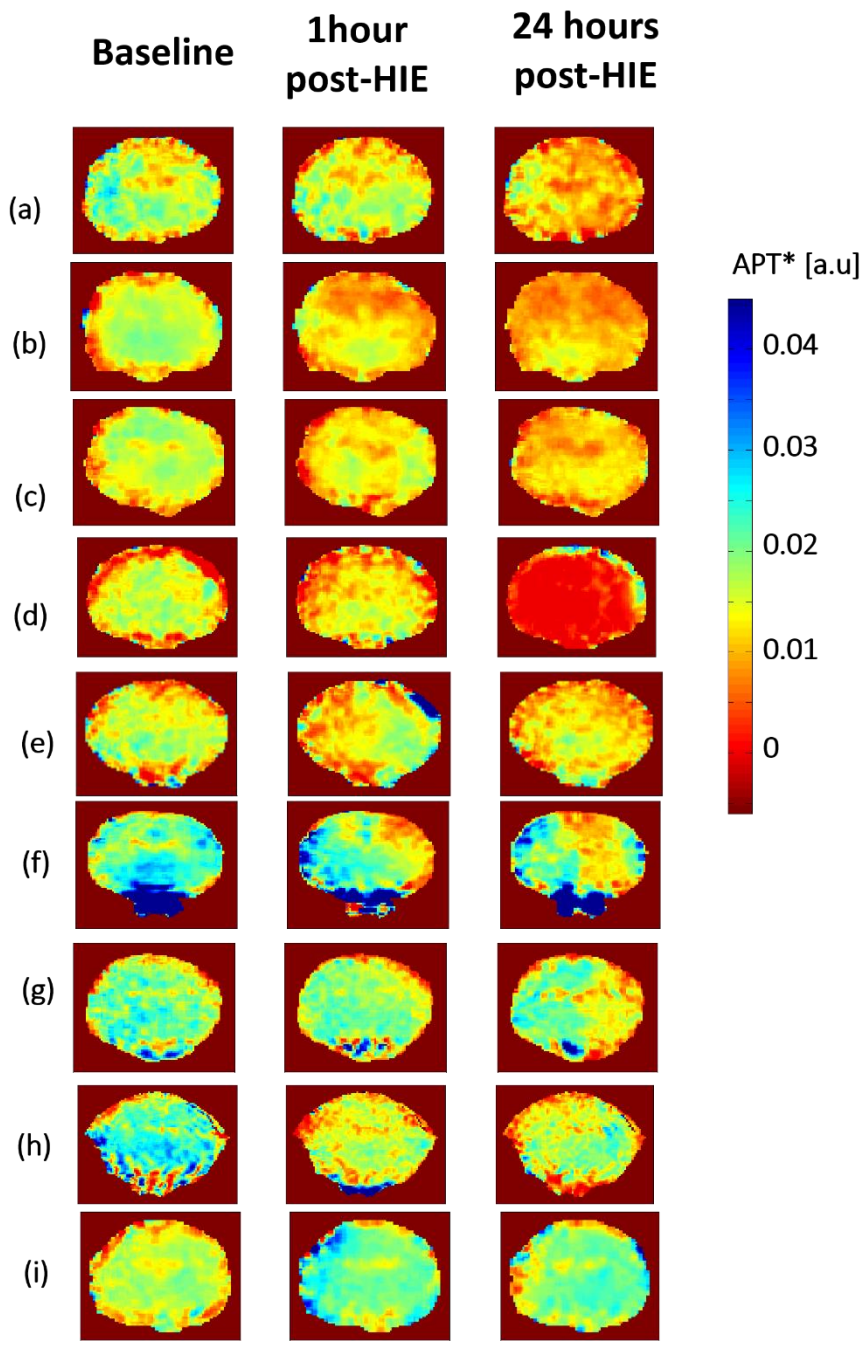

Figure 87: GROUP B: Summary of all HIE cases (a - i) characterised as 'fully recovered'. Images correspond to the APT value (peak height at 3.5ppm) for the baseline, 1 hour and 24 hours post-HIE. The APT* scale ranges between 0-0.04 units of height of the Z-Spectra analysed per pixel. Two main subcategories can be distinguished by visual observation of the APT* maps: cases a-f where APT* signal reduces in post-HIE scans compared to the baseline and cases g-i where the APT* maps show much less APT* signal reduction (flat response compared to the baseline).*

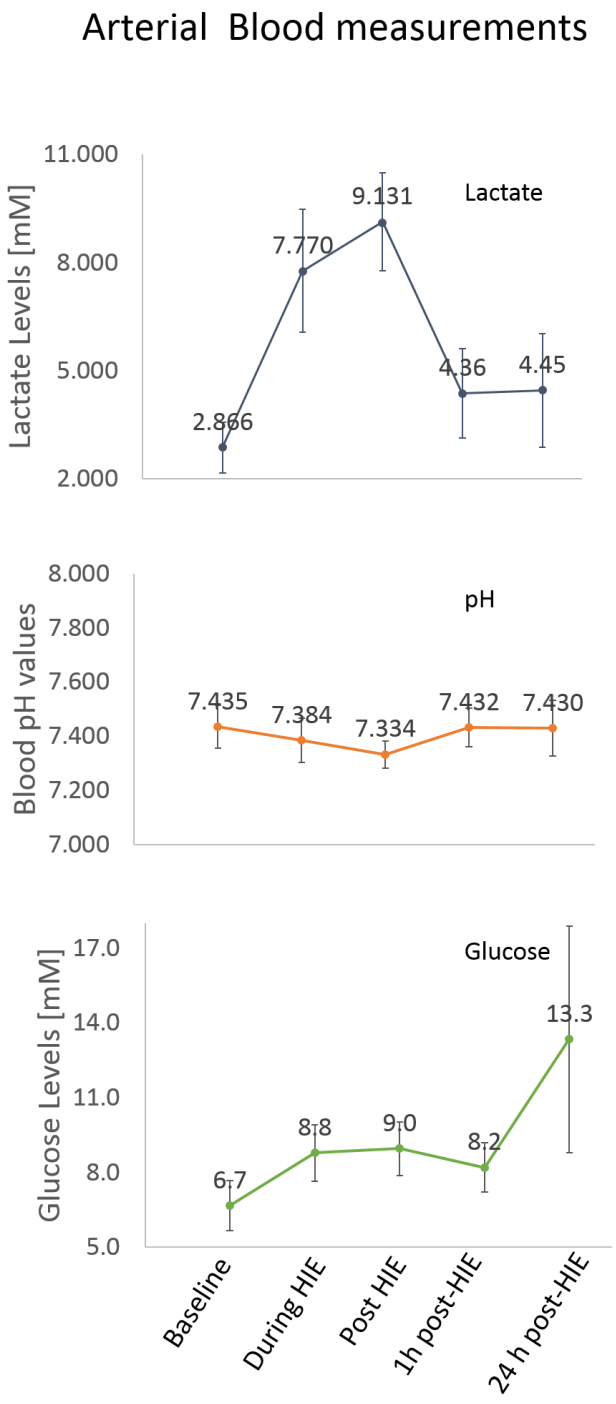

Figure 88: Shows the evolution of Lactate, pH and Glucose levels during the experiments. Blood samples were taken for analysis at baseline, during HIE, straight after, 1 hour and 24 hours post-HIE. Lactate (in blue) shows significant increase during and straight after insult ($p<0.001$) compared to the baseline values and post-HIE. Blood pH values (in orange) remain at similar levels (7.43) apart from the time straight after HIE, were the mean value dropped to 7.33 ($p<0.05$ compared to baseline values). Lastly, Glucose levels (in green), were elevated during and remained elevated after HIE ($p<0.01$). At 24 hours post insult animals varied in glucose levels with the majority maintaining values around 10mM but in three cases the glucose levels were found to reach more than 25mM (and up to 35mM). Data per piglet are included In Appendix E.

Factors affecting the APT signal

At least half of the piglets characterised as fully recovered, display similar patterns to the ones of group A (not fully recovered), emphasising the fact that encephalopathy episodes cannot be categorised only according on the NTP recovery at 1 hour post HI. Identifying the origins of the APT signal will furthermore help in understanding the physiological changes occurring after HI. As already discussed in section 2.3 ('factors affecting the CEST signal'), and reported by various papers [74, 30, 45], the sensitivity of CEST signal to a range of factors adds a level of complexity in any attempt for pH quantification; such factors are discussed in this section.

Temperature dependence

It is known that during vessel occlusion the brain temperature drops; studies report up to 5^{o}C of temperature difference compared to the core body temperature which is maintained at normothermia[25] [157, 158, 159]. This would have been an issue if CEST data were acquired during HIE. However CEST data were acquired 1 hour post-HI, at which time brain temperature is expected to be restored to normal levels [159]. In addition, studies have shown that the deep brain temperature correlates with the core body temperature when perfusion is restored (i.e. not during HI) in both animal models [160, 161, 162, 163] and neurosurgical patients [164, 165]. Since the animals were kept at 38.5^{o}C (body core temperature) during the experiments, it is assumed that deep brain temperature is maintained at 38.5^{o}C for the CEST data collection (baseline, 1 hour and 24 hours post HI).

Perfusion changes

For the duration of HI and for some time after, perfusion in the brain is highly disturbed. This is of course due to the actual vessel occlusion but also due to the recovery process the brain experiences afterward [166, 167]. Immediately following HI, perfusion increases up to 150% of the baseline value [166, 168] followed by a reduction to 80% of the baseline around 50 minutes post-HIE. Hypoperfusion duration is related to the severity of the insult [169], but can last for several hours

[25] Normal body temperature

post-HI, with similar levels of hypoperfusion in grey and white matter [170]. While the absolute APT values may vary from animal to animal due to different hypoperfusion levels, this will not contribute to the regional contrast of APT images as perfusion is estimated to be at similar level across the brain.

Metabolite concentration

One of the main characteristics of the CEST signal is its dependence on the concentration of the substrates containing exchangeable protons, as reported by Wolff and Balaban in 1990 [1], and followed by numerous subsequent studies [30, 45, 74]. The relationship of concentration to CEST is explained in section 2.3 and also part of Chapter 4, which is dedicated to the concentration dependence on BSA of the CEST signal. Any change in metabolite concentration can significantly alter the CEST effect.

During the experiments, blood samples were taken and glucose levels were measured, summarised in figure 88 (bottom graph, in green). A significant rise ($p<0.05$) in blood glucose concentration is found post HI, which is otherwise maintained during the time course of the experiments. However, if the change in glucose levels found in the circulating blood was corresponding to equivalent changes in brain glucose concentration and therefore affecting the outcome of the results, it would do so in an opposite trend compared to what has been reported post-HIE for the animals in this study (i.e. the elevated glucose levels would have resulted in an increase in the CEST signal). Additionally, the glucose resonance frequency range does not extend to 3.5ppm, the frequency investigated during this study [56, 17].

Moreover, no changes in the negative side of the Z-spectra (aliphatic range) were observed (illustration of overlapping signals from the aliphatic range in figure 80), while the APT peak was reduced post-HI. Aliphatic* was calculated in the same way as APT* at -3.5ppm. Figure 89 demonstrates the average APT* (in red) and Aliphatic* (in green) calculated from the cortical watershed region in the piglet brain (n=16). While APT* is significantly changed post-HIE ($p<0.001$ and $p<0.01$ for 1 hour and 24 hours respectively), no significant changes are observed in the Aliphatic* ($p>0.1$ for both post-HI measurements).

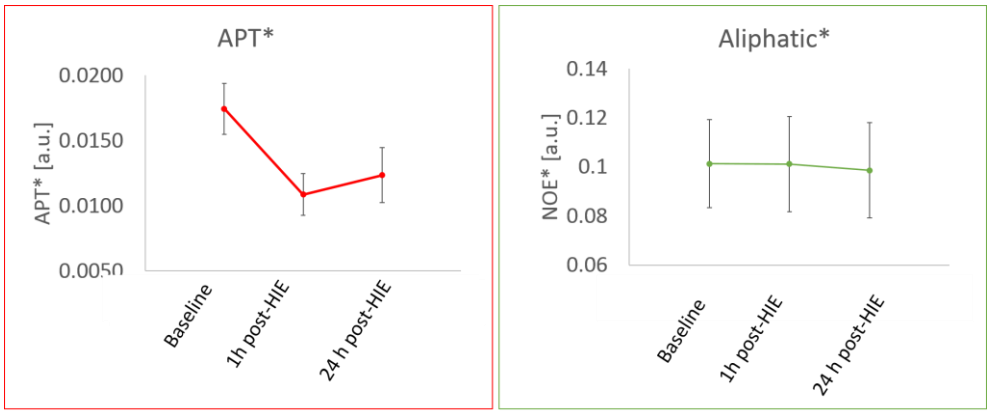

Figure 89: mean APT (in red) and Aliphatic* (in green) values calculated from the cortical watershed region of the piglet brain (All piglets included). APT*shows significant signal decrease post-HIE (p<0.001 1-hour and p<0.01 24 hours post-HIE). Aliphatic* shows no significant differences post-HIE (p>0.1 for both 1hour and 24 hours post-HIE).*

The findings of Chapter 4 and also a study by Jin et al 2013 [70] suggest that the aliphatic side of the BSA Z-spectra is concentration dependent but relatively pH-insensitive. This leads to the conclusion that post-HI the concentration of proteins was not altered and thus the reduction in the APT* signal was not likely to have occurred due to protein concentration changes (no reduction observed in the signal originating from the aliphatic peak).

Relaxation times

Changes in T_1 and T_2 values of the tissue also lead to modification of the CEST signal. Following an ischemic episode, the relaxation times of brain tissue might deviate from baseline values due to calcification [171], lipid release [172], haemorrhage and inflammation [145]. Unfortunately T_1 maps were not acquired as a part of this study, however simulations were performed (see figure 93) and are presented below in this section, suggesting that a change in T_1 value of ± 20% from the original value does not have a significant effect in the APT* contrast. Similarly, T_2 maps were also not acquired however, FWHM measurements were taken (as previously described in section 4.2.2.3 of the phantom study, and associated to T_2 in figure 51). Figure 90 shows the mean FWHM calculated from the same region as APT* (cortical watershed region in the brain). No significant changes (p>0.1) were observed post-HI, hence is assumed that no significant T_2 changes occurred during the time-course of the experiments.

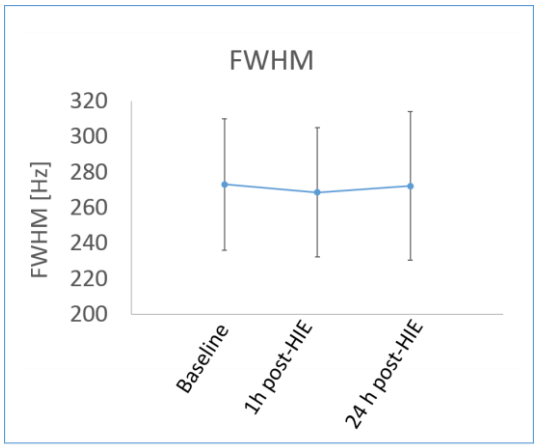

Figure 90: the mean FWHM values calculated from the same region as the APT measurements. No significant differences were observed comparing the baseline FWHM to any of the post-HIE FWHM.*

Association of APT* signal to tissue pH

Disturbances of metabolism during HI directly leads to the alteration of tissue pH as already discussed (see section 6.1, introduction), [173, 174]. As described in section 2.3 (*'Factors affecting the CEST signal'*), APT is sensitive to pH changes via the base-catalysed exchange rates of protons [9] and has been considered as a method for obtaining pH-weighted contrast by various groups; it has been applied to stroke rat models [175, 176, 69] and human studies [177, 178].

This section links the APT* signal calculated from the CEST data to pH quantified from ^{31}P MRS, assuming that the APT signal is mostly originating from the intracellular compartment [9].

Data in figure 91 display the relationship of the APT* signal averaged from the cortical watershed region in the piglet brain (figure 83) and pH measurements from a similar region (see section 6.2.4). A logarithmic relationship was chosen as the exchange rate is known to vary in this manner ($p<0.001$). The relationship deduced is given in equation 30 below and was used to calibrate the pH scale of APT* images.

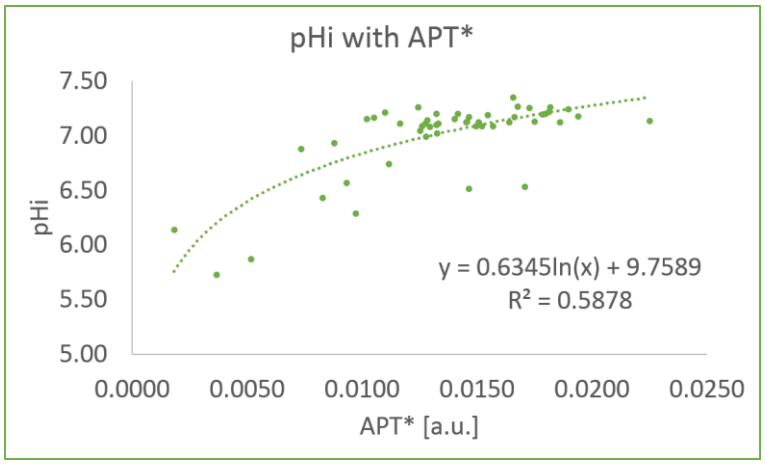

Figure 91: Correlation of pH values with the APT signal from all the animals in the study. A logarithmic relationship was chosen as the exchange rate is expected to vary in a similar manner (see equation 15 and figure 14). Pearson's correlation coefficient r indicates high statistical significance (p<0.001) for two-tailed test (n=52). See also Appendix F.*

$$pHi = 0.6345 \cdot ln(APT^*) + 9.7589 \qquad (30)$$

Three sample piglet data (from figures 86 & 87) are shown in figure 92 to demonstrate the pH scale calibrated from the APT* images.

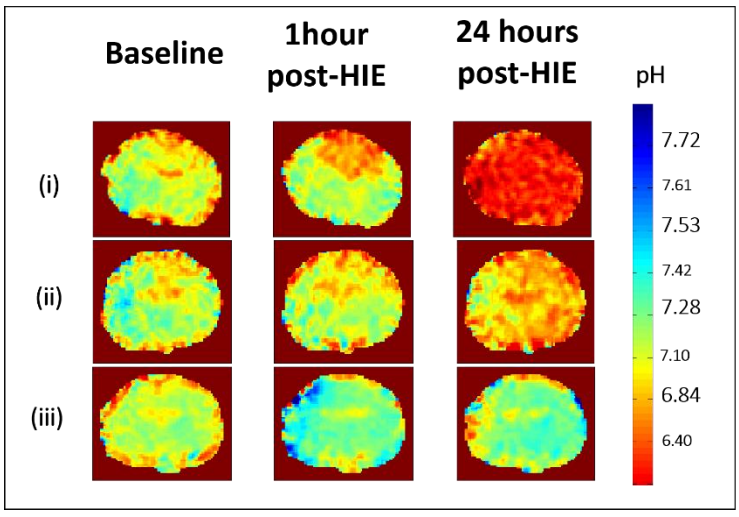

Figure 92: Calibrated pH maps from equation 30. (i) Corresponds to animal (a) of group A (not fully recovered), (ii & iii) animals (a) and (i) of group B (fully recovered) respectively.

In addition, the simulated data of APT* change with pH are shown in figure 93 for three T_1 values of the water pool. Different values were investigated as T_1 data were not available for the animals (section Relaxation times, 6.3).

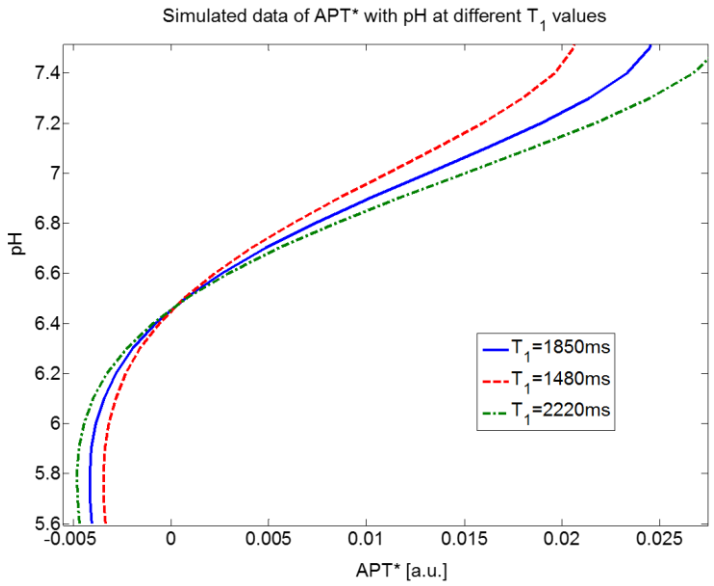

Figure 93: Simulated APT with pH variation for three different T_1 values for the water pool (1850ms, 1480ms and 2220ms corresponding to blue, red and green line respectively).*

From the simulated data, a variation in the APT* signal can be seen for different T_1.values, suggesting that for full pH quantification T_1 maps are also needed. However, the pH range from the experimental data is on average between 6 and 7 (as shown in figure 91), where the APT* trend remains very similar for different T_1 values. In addition any alteration due to T_1 is likely to be less than the variation caused by measurement noise.

APT* signal compared to Lactate/NAA

The ratio between Lactate/NAA has been associated with secondary energy failure[26] in HIE sufferers [179]. Mean APT* values 1 hour post-HI from the corresponding regions of the two MRS voxels (cortical and thalamic) are compared to the ^{1}H MRS data acquired 48 hours post-HI. Out of sixteen animals, eleven were available for comparison: group A cases (b), (d), (e) and group B all except case (e).

An inverse correlation is found (see figure 94, with a Pearson's correlation coefficient, ρ=0.67, p<0.02), with low APT* value present in regions of high Lactate/NAA ratios. Lactate is generally accepted as an indicator of anaerobic glycolysis [180] and NAA is believed to be a neuronal marker [146]. Hence the correlation suggests that the

[26] Brain injury occurring with a delay from the initial HI event

APT*signal may also be partially informing on the combined effect of neuronal damage due to lactate production.

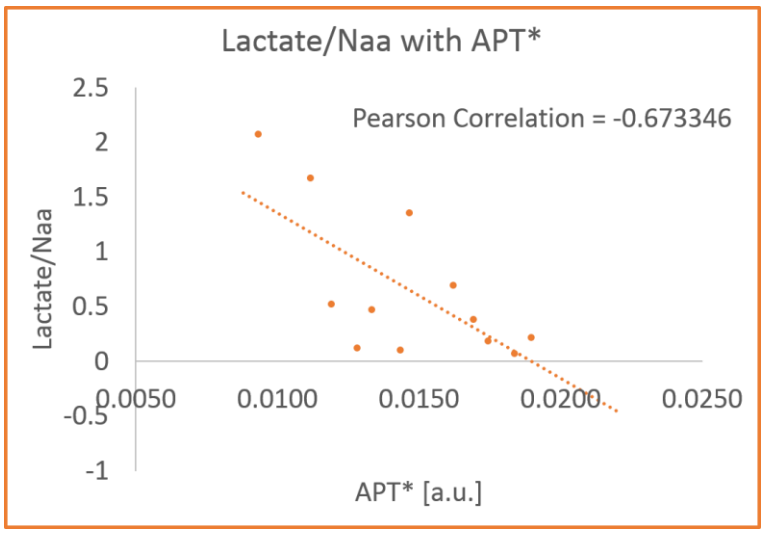

*Figure 94: Comparison of Lactate/NAA data measured 48 hours post-HIE to APT*measured 1 hour post-HIE. Pearson's correlation coefficient r= 0.6778 indicates significance (p<0.02) for two-tailed test (n=12). See also Appendix F.*

6.4. Conclusions

In this chapter the CEST technique was investigated in piglets suffering HI episodes as a potential biomarker of brain injury and pH alteration. Following HI, the APT* signal was shown to be decreased in the cortical region of the piglet brain in both groups (A & B). Data were compared and found to agree with blood lactate concentration but not with blood pH. It was concluded that APT may be informing on brain injury following HI.

In addition, the possibility of pH brain mapping was explored. The APT* signal was shown to be associated with the intracellular pH (chemical shift of Pi to PCr in ^{31}P MRS) via a logarithmic relationship and with the extracellular pH (lactate/NAA in ^{1}H MRS) via an inversed linear relationship. Eventually, if APT* is further shown to give important information on brain injury and pH, it would provide a supplementary diagnostic tool in the clinic for the assessment of neonatal HIE and for monitoring treatment effectiveness. However as discussed above, absolute pH quantification is challenging as the CEST effect is sensitive to numerous factors. Parameters such as

T_1, T_2 values, brain perfusion and temperature must be either tightly controlled or monitored to enable APT-CEST to provide semi-quantifiable pH measures in the clinic.

Chapter 7. Summary and directions for the future

A summary of the work done for this PhD thesis is outlined in this chapter, along with a discussion for future plans regarding research and applications of the CEST technique.

7.1. Summary of the PhD thesis

Being a relatively new MRI technique, the mechanisms involved in saturation experiments via chemical exchange are not yet fully understood. Hence there is still a requirement for basic research to investigate these effects.

The primary aim of this PhD thesis was to investigate the endogenous CEST signals and explore the utilisation of the technique for in-vivo neurological applications. This was achieved by studying the Bloch-McConnell equations (section 2.4) through a theoretical model implemented for the purposes of this PhD and relating the outcome to the BSA phantom study findings (Chapter 4).

An additional aim was to explore the CEST effects in the spine of mice with neurodegenerative diseases (specifically ALS and SBMA, Chapter 5) to identify potential early (pre-symptomatic stage) biomarkers, related to soluble protein accumulation. The spinal cord is a particularly challenging area of scanning due to its size, inhomogeneous B_0 and B_1 fields and physiological movements. A new sequence was therefore developed for this application, which accounts for physiological movement during data acquisition by using a respiration triggering scheme adapted for saturation experiments (Chapter 5, section 5.1.1).

Post-processing methodology was also implemented to weight down outliers in the spine-CEST data caused by motion (section 5.1.2). In both disease models, no changes were observed between affected mice at the different time points checked; findings were confirmed with post-mortem protein quantifications. Surprisingly, differences were observed between the control mice of 10 and 12 months of age; outcomes were also supported by post-mortem protein quantifications which revealed similar trends

in protein concentrations at the two scan-points. To our knowledge this is the first time such subtle protein changes have been found to correlate with CEST data from animal models. These findings were also surprising as such changes in the proteasome were not expected.

The last aim of this Ph.D was to study another facet of the endogenous CEST signal, namely its dependence in pH. For this, we studied the CEST signal in piglets undergoing HI, a model of neonatal encephalopathy and related the findings to pH alterations as measured by ^{31}P MRS following HI. This would ideally provide spatial information on the pH changes following ischemia and therefore allow better monitoring of the neonates if the technique is to be translated to the clinic. For the purposes of this work an imaging CEST sequence was implemented and adopted for the piglet brain (Chapter 6). In addition, a new method was proposed to analyse the CEST data (APTp/APT* in section 3.2), which is not confounded by any other endogenous contributions but is (mostly) related to the changes due to the induced HI.

7.2. Future work directions

Research in the CEST field has been exponentially increasing within the last decade, however there are still many questions to tackle and numerous areas to explore within the CEST world. Basic science is still required as the CEST effects are not yet fully understood.

CEST validation research

A small example is found in our work done with the BSA phantom (Chapter 4), where the behaviour of the Z-Spectra in different pH environments is unclear. More CEST experiments are required as well as comparison with other methods, such as NMR spectroscopy, in order to understand better the underpinnings and subtle variations of the CEST dependence on pH.

Another example would be to explore the CEST signal in amino acids compared to polymers (i.e: lysine to poly-L-Lysine, glutamine to poly-L-glutamine, etc). Such experiment would help understand the changes in the CEST signal between small

mobile molecules and larger molecules (of the same species). So far, a simple multiplication effect has always been estimated, however protein folding might alter access of water protons to exchangeable sites and therefore lead to large variations in the CEST effects with the number of exchanging sites.

Many CEST areas of interest were not covered within this thesis, including CEST effects in liposomes (lipoCEST) [45], hyperCEST, paraCEST agents [30], glucoCEST, [17] etc. Nonetheless, a large amount of research is focused on contrast-based CEST imaging, with agents that may serve as temperature or pH probes and contribute to pharmacokinetic studies.

More pre-clinical studies should also be conducted, such as extended work in the spinal cord of mice with larger cohorts, looking at the CEST signal in comparison to post-mortem protein quantification and other MRI techniques such as MT, T_1 and T_2 maps. This would be an important step in understanding the nature of the CEST signal and the potential future application of the CEST technique in neurodegenerative diseases. As a long-term plan one would expect to implement spine-CEST in the clinic to study neurodegenerative diseases in patients, but only after better understanding of the basic physiology of the proteasome has been gathered in animals.

Regarding the work conducted in the piglet brain (Chapter 6), it would be interesting to use a dual-tuned ^{1}H and ^{31}P RF coil to avoid changing during the experiments. This would improve the experiments in terms of better reproducibility (less imaging registration issues), while interleaved CEST, ^{31}P MSR and ^{1}H MRS can be acquired for a better comparison between APT*, pH_i and Lactate/NAA levels. Eventually, the method should translate into the clinic for neonates suffering HI.

Standardisation of the CEST technique

As the CEST technique grows among research institutions and work is translated into the clinic, the need for standardised measurements becomes more urgent. As

discussed in this work, many methods can be used in order to achieve CEST contrast (section 3.1) and even more techniques have been implemented for the interpretation of the signal (section 3.2). Even looking throughout this thesis, a few different procedures have been reported for measuring the CEST signal. The problem starts when there is a need for data comparison across sites, which is complicated if data were acquired with different protocols, or even just analysed in different ways. The variation might come from something as simple as the normalisation of the Z-Spectra, or the frequency integration range. Therefore, it is crucial for the field to study the effects of all parameters, including RF coil transmission and reception, signal readout, saturation methods and data analysis.

Finally, the clinical potential of the technique needs to be more extensively explored. With the current standards, there are currently important limitations due to B1 and B0 inhomogeneities as well as SAR limitations to overcome. Efforts for harmonising clinical protocols need to be implemented and only by doing this can the CEST technique grow into a truly valuable contrast mechanism that can be used widely and routinely in hospitals across the world.

Appendix A – *'The multipool Bloch McConnell model'*

The Bloch-McConnell equation system describing the total magnetisation M, is given in a matrix form such that

$$\frac{dM}{dt} = A \cdot M - B$$

The system can be expanded following the same pattern for n number of pools. Considering below a 5 pool model (Pools **A-E**) the equation system can be written as

$$\begin{bmatrix} \partial M_x^A/\partial t \\ \partial M_y^A/\partial t \\ \partial M_z^A/\partial t \\ \partial M_x^B/\partial t \\ \partial M_y^B/\partial t \\ \partial M_z^B/\partial t \\ \vdots \\ \vdots \\ \partial M_x^E/\partial t \\ \partial M_y^E/\partial t \\ \partial M_z^E/\partial t \end{bmatrix} = A \cdot \begin{bmatrix} M_x^a \\ M_y^a \\ M_z^a \\ M_x^b \\ M_y^b \\ M_z^b \\ \vdots \\ \vdots \\ M_x^e \\ M_y^e \\ M_z^e \end{bmatrix} - \begin{bmatrix} M_x^a/T_2^a \\ M_y^a/T_2^a \\ (M_0^a - M_z^a)/T_1^a \\ M_x^b/T_2^b \\ M_y^b/T_2^b \\ (M_0^b - M_z^b)/T_1^b \\ \vdots \\ \vdots \\ M_x^e/T_2^e \\ M_y^e/T_2^e \\ (M_0^e - M_z^e)/T_1^e \end{bmatrix}$$

where

$$A = \begin{bmatrix} -k_{ab}\,[\cdots] - k_{ae} & -\Delta\omega_a & 0 & k_{ba} & 0 & 0 & \cdots & k_{ea} & 0 & 0 \\ \Delta\omega_a & -k_{ab}\,[\cdots] - k_{ae} & -\omega_1 & 0 & k_{ba} & 0 & \cdots & 0 & k_{ea} & 0 \\ 0 & \omega_1 & -k_{ab}\,[\cdots] - k_{ae} & 0 & 0 & k_{ba} & \cdots & 0 & 0 & k_{ea} \\ k_{ab} & 0 & 0 & -k_{ba} & -\Delta\omega_b & 0 & \cdots & 0 & 0 & 0 \\ 0 & k_{ab} & 0 & \Delta\omega_b & -k_{ba} & -\omega_1 & \cdots & 0 & 0 & 0 \\ 0 & 0 & k_{ab} & 0 & \omega_1 & -k_{ba} & \cdots & 0 & 0 & 0 \\ \vdots & \vdots & \vdots & \vdots & \vdots & \vdots & \ddots & \vdots & \vdots & \vdots \\ \vdots & \vdots & \vdots & \vdots & \vdots & \vdots & \ddots & \vdots & \vdots & \vdots \\ k_{ae} & 0 & 0 & 0 & 0 & 0 & \cdots & -k_{ea} & -\Delta\omega_e & 0 \\ 0 & k_{ae} & 0 & 0 & 0 & 0 & \cdots & \Delta\omega_e & -k_{ea} & -\omega_1 \\ 0 & 0 & k_{ae} & 0 & 0 & 0 & \cdots & 0 & \omega_1 & -k_{ea} \end{bmatrix}$$

where $M_x^{A,B,C,D,E}, M_y^{A,B,C,D,E}, M_z^{A,B,C,D,E}$ are the magnetisation components of pools **A-E** at time t along the x, y and z axis respectively. The loss of magnetisation in pool **A** is described by $K_{ab}.M_z^b$ and the gain in pool **B** is described by $K_{ba}.M_z^a$ (the same applies for all the other pools in the same manner). $\Delta\omega_{a,b,c,d,e} = \omega_{RF} - \omega_{a,b,c,d,e}$ is the resonance frequency of the corresponding exchangeable site pool given relative to the RF frame (ω_{RF} corresponds to the frequency of the applied RF pulse). If pool A corresponds to water, then $\omega_a = 0$.

The equation system above considers interaction between pools **B-E** with **A**, where **A** is considered to be the main water pool and **B-E** any other exchangeable site pools present. No interaction between other pools has been taken into account. Illustration of such a system is given in (Appendix B, *'Simulation of the Bloch-McConnell model'*, Steady State solution).

Appendix B – *'Steady State Solution of the Bloch-McConnell model. Simulation of 8 pools'*

The following is an example script used as an *eight-pool steady state model*. It is based on the Bloch-McConnell system of equations as given in Appendix A but expanded to accommodate eight exchangeable site pools. This model also includes a connection between pools **C** and **D**, used to study the interaction between sites other than the free water.

```
%% 8 Pool Bloch-McConnell model STEADY STATE
interaction_CD=0; %to add a connection between pools C and D
%constants
gamma=42.576*10^6*2*pi; %[Radians s-1 T-1], B0=9.4; %T, w0=gamma*B0; np=1001;
One_ppm= 3.995259712500000e+02; %9.4T Queen Square house
%% B1equivalet for Agilent Gaussian
nsigma=5.84; %number of sigmas the pulse shape uses. Calculated from shape lib.
FA=540; FA=FA*pi/180; %to radians Duration=50; Duration=Duration/1000; %to secs
IntDelay=1; IntDelay=IntDelay/1000; %to secs
sigma=Duration/nsigma;, intePercentage=erf(nsigma/sqrt(2));
B1eq=sqrt(FA^2*sqrt(pi)/(2*pi*sigma*gamma^2*(Duration+IntDelay)*intePercentage));
B1=B1eq; w1=gamma*B1 %w1 goes in rad/s BUT delta ,ppmc and exRates in Hz. in the equations delta is multiplied by 2pi
%Relative concentration
M0a=1; %water; glucoseMolarity=160;%in mMolar
%pool sizes
M0b=3*M0a/100; %MT pool M0c=3/3*glucoseMolarity/(1000*55); %Glucose poolsM0d=3/4*glucoseMolarity/(1000*55);
M0e=0*glucoseMolarity/(1000*55);M0f=1*M0a/25; M0g=0*M0a/50; M0h=1*glucoseMolarity/(1000*55); %
Mall= M0a+M0b+M0c+M0d+M0e+M0f+M0g;
pH=7
%% Relaxation Times of each spin species
T1a=1.85*1.2; %s T1b=0.01;%for MT, T1c=1.5;T1d=1.5;T1e=1.8;T1f=0.26; T1g=0.1;T1h=1.5;
T2a=3.2*exp(-M0b*140); T2b=0.00001/2;for MT T2c=0.035; T2d=0.035;T2e=0.0007;T2f=0.00034;T2g=0.00034; T2h=0.4;
Tranfer rates
% K0=0;Ka=25;Kb=1.2*10^10;pKw=14; % values that allow lower exchange rates for acidic environments
K0=1000;Ka=25;Kb=0.7*10^10;pKw=14; % values that match Chan, van Zijl MRM2012
KexG=K0+Ka*10.^(-pH)+Kb*10.^(pH-pKw);
Rb=50;  %fot MT Rg=KexG*0.55;  %s^(-1)Rg=KexG*0.75;Rh=KexG*1;
Re=4.5; %for fat or NOE
%from pH mapping based on the ratiometric amide and amine relationship from
%endogenous CEST  Kim Desmond1, Greg Stanisz 1,2
% pH=[6.4 6.7 7 7.3]
AminesEx=10.^(pH-5.2);  AminesEx=10.^(pH-4.4); %At 2ppm, Rc=1*AminesEx;
AmidesEx=5.57*10.^(pH-7.2); AmidesEx=5.57*10.^(pH-6.4); % At 3.5 ppm, Rd=1*AmidesEx;
Rinteract=100000 %pH independent. For NH2 to NH exchange rate [H+]

%% Saturation efficiency to account for relaxation in XY plane
alphab=w1^2/(w1^2+Rb^2*T2b); alphac=w1^2/(w1^2+Rc^2*T2c); alphad=w1^2/(w1^2+Rd^2*T2d);
alphae=w1^2/(w1^2+Re^2*T2e); alphaf=w1^2/(w1^2+Rf^2*T2f); alphag=w1^2/(w1^2+Rg^2*T2g);
alphah=w1^2/(w1^2+Rh^2*T2h);
```

```
M0b=M0b*alphab; M0c=M0c*alphac; M0d=M0d*alphad; M0e=M0e*alphae; M0f=M0f*alphaf; M0g=M0g*alphag;
M0h=M0h*alphah;
%% CEST pool off resonance frequency from water pool
ppmb=0; ppmc=+2.1; ppmd=3.6; ppme=-3.5; ppmf=1.3; ppmg=3; ppmh=1;

dcb=w0*10^-6/(2*pi)*ppmb; dcc=w0*10^-6/(2*pi)*ppmc; dcd=w0*10^-6/(2*pi)*ppmd; dce=w0*10^-6/(2*pi)*ppme;
dcf=w0*10^-6/(2*pi)*ppmf; dcg=w0*10^-6/(2*pi)*ppmg; dch=w0*10^-6/(2*pi)*ppmh;
%for the cone picture
% wrf=w0*(1+ppm*10^-6);
% B0eff=(w0-wrf)/gamma; %in Z direction
%Beff=[B1,0,B0eff];
%%%%%%%%%%%%%
MM=zeros(22,np); Rrfb=zeros(1,np); D=zeros(1,np); ppm=zeros(1,np);maxoffsetppm=2432/One_ppm;
for p=1:np
        ppm=2*maxoffsetppm/(np-1)*(p-1)-maxoffsetppm;
        D=w0*10^-6/(2*pi)*ppm;
        %% Superlorentzian function
        q=10000;
        % p=1000;
        o = linspace(0, pi/2, q);
        value=sin(o).*(2/pi).^0.5*T2b./abs(3*cos(o).^2-1).*exp(-2*(2*pi*(D-dcb).*T2b./(abs(3*cos(o).^2-1))).^2);
        da=pi/(2*(q-1)).*value; Amt=sum(da); %superlorentzian function for every D
        Rrfb(1,p)=Amt*w1^2*pi; %Rrfb(1,p)=1*Amt*w1^2; not sure if we have to multiply by w1^2
        % %% 8 pool system
        %% Tranfer rates
        Rbp=Rb*Rrfb(1,p);%Rb; %fot MT
        Rcp=Rc;%s^(-1)
        Rdp=Rd;
        Rep=Re;
        Rfp=Rf;
        Rgp=Rg;
        Rhp=Rh;

        dm1=[(-1/T2a-Rc*M0c-Rd*M0d-Re*M0e-Rf*M0f-Rg*M0g-Rh*M0h),-
2*pi*D,0,0,Rc*M0a,0,0,Rd*M0a,0,0,Re*M0a,0,0,Rf*M0a,0,0,Rg*M0a,0,0,Rh*M0a,0,0];
        dm2=[2*pi*D,(-1/T2a-Rc*M0c-Rd*M0d-Re*M0e-Rf*M0f-Rg*M0g-Rh*M0h),-
w1,0,0,Rc*M0a,0,0,Rd*M0a,0,0,Re*M0a,0,0,Rf*M0a,0,0,Rg*M0a,0,0,Rh*M0a,0];
        dm3=[0,w1,(-1/T1a-Rbp*M0b-Rcp*M0c-Rdp*M0d-Rep*M0e-Rf*M0f-Rg*M0g-
Rh*M0h),Rbp*M0a,0,0,Rcp*M0a,0,0,Rdp*M0a,0,0,Rep*M0a,0,0,Rfp*M0a,0,0,Rgp*M0a,0,0,Rhp*M0a];

        dm6=[0,0,Rbp*M0b,(-1/T1b-Rrfb(1,p)-Rbp*M0a),0,0,0,0,0,0,0,0,0,0,0,0,0,0,0,0,0];

        if interaction_CD==1
            dm7=[Rc*M0c,0,0,0,(-1/T2c-Rc*M0a-Rinteract*M0d),-2*pi*(D-
dcc),0,Rinteract*M0c,0,0,0,0,0,0,0,0,0,0,0,0,0];
            dm8=[0,Rc*M0c,0,0,2*pi*(D-dcc),(-1/T2c-Rc*M0a-Rinteract*M0d),-
w1,0,Rinteract*M0c,0,0,0,0,0,0,0,0,0,0,0,0,0];
            dm9=[0,0,Rcp*M0c,0,0,w1,(-1/T1c-Rcp*M0a-Rinteract*M0d),0,0,Rinteract*M0c,0,0,0,0,0,0,0,0,0,0,0];

            dm10=[Rd*M0d,0,0,0,Rinteract*M0d,0,0,(-1/T2d-Rd*M0a-Rinteract*M0c),-2*pi*(D-
dcd),0,0,0,0,0,0,0,0,0,0,0,0,0,0];
            dm11=[0,Rd*M0d,0,0,0,Rinteract*M0d,0,2*pi*(D-dcd),(-1/T2d-Rd*M0a-Rinteract*M0c),-
w1,0,0,0,0,0,0,0,0,0,0,0,0,0,0];
            dm12=[0,0,Rdp*M0d,0,0,0,Rinteract*M0d,0,w1,(-1/T1d-Rdp*M0a-Rinteract*M0c),0,0,0,0,0,0,0,0,0,0,0,0];
            else
            dm7=[Rc*M0c,0,0,0,(-1/T2c-Rc*M0a),-2*pi*(D-dcc),0,0,0,0,0,0,0,0,0,0,0,0,0,0,0];
            dm8=[0,Rc*M0c,0,0,2*pi*(D-dcc),(-1/T2c-Rc*M0a),-w1,0,0,0,0,0,0,0,0,0,0,0,0,0,0];
            dm9=[0,0,Rcp*M0c,0,0,w1,(-1/T1c-Rcp*M0a),0,0,0,0,0,0,0,0,0,0,0,0,0,0];

            dm10=[Rd*M0d,0,0,0,0,0,0,(-1/T2d-Rd*M0a),-2*pi*(D-dcd),0,0,0,0,0,0,0,0,0,0,0,0];
            dm11=[0,Rd*M0d,0,0,0,0,0,2*pi*(D-dcd),(-1/T2d-Rd*M0a),-w1,0,0,0,0,0,0,0,0,0,0,0];
            dm12=[0,0,Rdp*M0d,0,0,0,0,0,w1,(-1/T1d-Rdp*M0a),0,0,0,0,0,0,0,0,0,0,0];
        end
            %Interaction between Pool C and Pool D
```

```
        dm13=[Re*M0e,0,0,0,0,0,0,0,0,0,(-1/T2e-Re*M0a),-2*pi*(D-dce),0,0,0,0,0,0,0,0,0,0];
        dm14=[0,Re*M0e,0,0,0,0,0,0,0,0,2*pi*(D-dce),(-1/T2e-Re*M0a),-w1,0,0,0,0,0,0,0,0,0];
        dm15=[0,0,Rep*M0e,0,0,0,0,0,0,0,0,w1,(-1/T1e-Rep*M0a),0,0,0,0,0,0,0,0,0];

        dm16=[Rf*M0f,0,0,0,0,0,0,0,0,0,0,0,0,(-1/T2f-Rf*M0a),-2*pi*(D-dcf),0,0,0,0,0,0,0];
        dm17=[0,Rf*M0f,0,0,0,0,0,0,0,0,0,0,0,2*pi*(D-dcf),(-1/T2f-Rf*M0a),-w1,0,0,0,0,0,0];
        dm18=[0,0,Rfp*M0f,0,0,0,0,0,0,0,0,0,0,w1,(-1/T1f-Rfp*M0a),0,0,0,0,0,0];

        dm19=[Rg*M0g,0,0,0,0,0,0,0,0,0,0,0,0,0,0,0,0,(-1/T2g-Rg*M0a),-2*pi*(D-dcg),0,0,0,0];
        dm20=[0,Rg*M0g,0,0,0,0,0,0,0,0,0,0,0,0,0,0,0,2*pi*(D-dcg),(-1/T2g-Rg*M0a),-w1,0,0,0];
        dm21=[0,0,Rgp*M0g,0,0,0,0,0,0,0,0,0,0,0,0,0,0,w1,(-1/T1g-Rgp*M0a),0,0,0];

        dm22=[Rh*M0h,0,0,0,0,0,0,0,0,0,0,0,0,0,0,0,0,0,0,0,(-1/T2h-Rh*M0a),-2*pi*(D-dch),0];
        dm23=[0,Rh*M0h,0,0,0,0,0,0,0,0,0,0,0,0,0,0,0,0,0,0,2*pi*(D-dch),(-1/T2h-Rh*M0a),-w1];
        dm24=[0,0,Rhp*M0h,0,0,0,0,0,0,0,0,0,0,0,0,0,0,0,0,0,w1,(-1/T1h-Rhp*M0a)];
        %%

A=[dm1;dm2;dm3;dm6;dm7;dm8;dm9;dm10;dm11;dm12;dm13;dm14;dm15;dm16;dm17;dm18;dm19;dm20;dm21;d
m22;dm23;dm24];
        B=[0;0;M0a/T1a;M0b/T1b;0;0;M0c/T1c;0;0;M0d/T1d;0;0;M0e/T1e;0;0;M0f/T1f;0;0;M0g/T1g;0;0;M0h/T1h];
        M=A\(-B);  %"matrix division"
        MM(:,p)=M;
end
```

Appendix C – *'Dynamic Solution of the Bloch-McConnell model. Simulation of 2 pools'*

A dynamical model was also used to simulate saturation train lengths, readout pulses and to study the evolution of magnetisation in time. The following piece of code is written based on a two pool system.

```
%% 2Pool Bloch-McConnell model DYNAMIC SOLUTION
gamma=42.576*10^6*2*pi; %[ s-1 T-1]
FlipA=1540; num_gauss=200; interpuseDelay=5*10^-3; duration=50*10^-3;
ppm=2; %Rf pulse off resonance frequency from water pool
ppmc=2; %CEST pool off resonance frequency from water pool
M0a=1;
molarity=200;%[mMolar]
M0c=3/3*molarity/(1000*55); %Glucose pools
Ex1=30; %exchange rate of water and cest pools
T2a=0.032; T1a=1.7; T2c=0.01; T1c=1;
tspan = [-0.5 10];
M0(1,:)=[0,0,M0a,0,0,M0c];
for offset=1:1;
   ppm=-4.1+offset/10; %Rf pulse off resonance frequency from water pool
   ppm=3.5;
   [t, M] = ode45(@sixequations, tspan, M0(1,:));
   All_M{offset}=M;
   All_t{offset}=t;
end
%%%%%%%%  Definition of the equation function %%%%%%%%%%%%
function dM=sixequations(t,M)
      dM=zeros(6,1); B0=9.4; w0=gamma*B0; D=w0*10^-6/(2*pi)*ppm;
      dc=w0*10^-6/(2*pi)*ppmc;
      t0=0;  tmax=(t0+duration/2);
      s=duration/5.86; FA=FlipA*pi/180; Amp=FA/(s*sqrt(2*pi)*gamma); %FA in Rad
      yy=0; %for the begining of the loop
      for n=1:num_gauss
      yy=yy+exp(-((t-(tmax+(n-1)*(duration+interpuseDelay)))/s).^2/2);
      end
      B1=Amp*yy;
      %% Square pulse a
       ti=0.3; tf=5;Ba=0; if (ti <= t) && (tf > t), Ba=B1;, end
       Square pulse b
       delay=0.00372; ti2=tf+delay; tf2=0.55+delay; Bb=0;
       if  (ti2 <= t) && (tf2 > t);, Bb=0*1*B1; end
        B1=Ba+Bb;
      %%Triangular  pulse
       tia=0.0; tfb=0.05; tfa=(tfb-tia)/2; tib=tfa; B1=0;
       if (tia <= t) && (tfa >= t);,B1=200*5*20*0.1175*10^-6*t;,end
       if  (tib < t) && (tfb > t) , B1=200*5*20*0.1175*10^-6*(2*tfa-t);end
       %%Pulse Sequence
      mtcrusher=3*10^-3; %time duration at the end of sat pulse train.
      Bef_Read=0.008; %time delay before the readout pulse.
      Aft_Read=4.5*10^-3;  %time delay after the readout pulse.
       %%% Saturation pulses train
      SatFlip=7000; %in degree.
      SatPulse=50*10^-3; %time duration of the sat pulse.
```

```
    SatDelay=4*10^-6; %time duration between sat pulses.
     SatFlipRad=SatFlip*pi/180;
    %B1c_Sat=SatFlipRad/(gamma*(SatPulse+SatDelay)); i thinks its worng
    sigmaSat=SatPulse/7;  A_Sat=SatFlipRad/(sqrt(2*pi)*gamma*sigmaSat);
    b0=4*10^-6;  t0=3.5*sigmaSat;  b=0; B1=0; %just to start with
     for p=1:10
       spike=A_Sat*(exp(-(t-t0-b-Aft_Read).^2/(2*sigmaSat^2)));
       b=b+b0+SatPulse+SatDelay;
       B1=B1+spike;
    end
    % Readout pulse
    ReadFlip=20;  %in degree too.
    ReadPulse=20*10^-3; %time duration of the readout pulse.
    Bef_Read=12*10^-6;
    mtcrusher=12*10^-6;
    sigmaRead=ReadPulse/7;
    ReadFlipRad=ReadFlip*pi/180;
    %B1c_Read=ReadFlipRad/(gamma*(ReadPulse)); % [T] For 20 degrees, 2ms pulse
    A_Read=ReadFlipRad/(sqrt(2*pi)*gamma*sigmaRead);
    Readout=A_Read*(exp(-(t-(mtcrusher+Bef_Read+ReadPulse/2)-b).^2/(2*sigmaRead^2)));
    B1=B1+Readout;
    TR=b0+p*(SatPulse*SatDelay)+mtcrusher+Bef_Read+Aft_Read+ReadPulse;
    w1=gamma*B1;
    if (w1==0)
       D=0; dc=0;
    end
    if t> num_gauss*(duration+interpuseDelay) %%sets the offset of the readout pulse to the water freq
       D=0;
    end
    % 2-Pool model equations
    dM(1)=(-1/T2a-Ex1*M0c)*M(1)+(-2*pi*D)*M(2)+Ex1*M0a*M(4);
    dM(2)=2*pi*D*M(1)+(-1/T2a-Ex1*M0c)*M(2)-w1*M(3)+Ex1*M0a*M(5);
    dM(3)=w1*M(2)+(-1/T1a-Ex1*M0c)*M(3)+Ex1*M0a*M(6)+M0a/T1a;

    dM(4)=Ex1*M0c*M(1)+(-1/T2c-Ex1*M0a)*M(4)-2*pi*(D-dc)*M(5);
    dM(5)=Ex1*M0c*M(2)+2*pi*(D-dc)*M(4)+(-1/T2c-Ex1*M0a)*M(5)-w1*M(6);
    dM(6)=Ex1*M0c*M(3)+w1*M(5)+(-1/T1c-Ex1*M0a)*M(6)+M0c/T1c;
end
```

Appendix D – *'B_1 Calculations. Continuous to pulsed saturation'*

The saturation power of an RF pulse of any shape $B_1(t)$ is calculated as the equivalent power of a hard pulse of duration Δt. Often in literature, the equivalent power is given as B_{1eq} (T) such as

$$P \propto \frac{\int_0^{\Delta t} B_1^2(t)dt}{\Delta t} = B_{1eq}^2$$

Experiments in this study were performed with a train of Gaussian pulses; the equation below shows the B_{1eq} for such pulses.

$$\mathrm{B_{1eq}} = \frac{\theta}{\gamma\sqrt{2\sqrt{\pi}\sigma(t_{gauss} + t_{delay}) \cdot f_{err}(n_\sigma/\sqrt{2})}}$$

where θ is the flip angle (in rad), γ the gyromagnetic ratio (in rad/s/T), σ the standard deviation of the Gaussian pulse, n_σ the number of standard deviations included in the pulse width (for the experiments conducted in this study, n_σ =5.84). The duration of the Gaussian pulse, t_{gauss} and the interpulse delay, t_{delay} are both given in ms.

Appendix E – *'Arterial blood measurements for piglets of Chapter 6'*

TABLE 1: Lactate levels given in mM concentration for group A (gA) and group B (gB).

Piglet	Baseline	During HIE	Post HIE	1.5h Post HIE	24h Post HIE
a (gB)	1.69	9.46	9.79	1.70	5.47
b (gB)	4.99	8.92	10.59	5.99	5.80
c (gB)		5.78		6.74	1.62
d (gB)	2.38	4.44	14.07	6.47	10.17
f (gB)	1.72	5.51	9.21	5.02	3.06
g (gB)		9.65		1.77	4.18
h (gB)		12.73		0.95	2.79
i (gB)	3.42	9.01	10.93	1.75	7.29
b (gA)	0.70	2.67	7.08	1.86	1.65
c (gA)	3.44	1.98	4.07	3.81	1.92
d (gA)	3.3	8.38	9.88	7.411	2.84
e (gA)	2.06	10.68	8.85	7.75	1.40
f (gA)	4.96	11.8	6.84	5.52	2.98
g (gA)	7.7				11.14

TABLE 2: pH values for for group A (gA) and group B (gB).

Piglet	Baseline	During HIE	Post HIE	1.5h Post HIE	24h Post HIE
a (gB)	7.339	7.600		7.450	7.530
b (gB)		7.507	7.277	7.424	7.483
c (gB)		7.561	7.409	7.795	7.411
d (gB)	7.595	7.412	7.435	7.482	7.749
f (gB)		7.394	7.447	7.489	7.463
g (gB)	7.409	7.195	7.256	7.412	7.438
h (gB)	7.337	7.283	7.251	7.197	7.152
i (gB)	7.397	7.216	7.265	7.345	7.832
b (gA)	7.235	7.300		7.360	7.050
c (gA)	7.760	7.633	7.430	7.545	7.420
d (gA)	7.35	7.058		7.411	7.490
e (gA)		7.400			7.264
f (gA)		7.414	7.169	7.270	7.295
g (gA)	7.494	7.408	7.398	7.440	7.446

TABLE 3: Glucose levels in mM concentration for for group A (gA) and group B (gB).

Piglet	**Baseline**	**During HIE**	**Post HIE**	**1.5h Post HIE**	**24h Post HIE**
a (gB)	8.2			8.5	12.3
b (gB)		6.9	8.3	7.0	6.3
c (gB)	10	11.8		7.6	9.8
d (gB)		10.4			13.3
f (gB)		6.6	7.2	7.2	8.7
g (gB)	5.2	6.1	5.7	4.8	26.2
h (gB)	6.9	6.5		7.0	5.3
i (gB)		7.9	8.1	9.3	5.7
b (gA)		7.1	7.1	7.4	9.8
c (gA)	3.7	8.5	8.5	7.5	11.8
d (gA)		11.6	11	9.6	7.2
e (gA)		12.9	12.8	12.5	34.3
f (gA)	6.3	8.9	11	11	27.1
g (gA)	6.4	9	9.8	7.2	9.0

NB: Blood measurements were taken as consistently as possible by the team responsible for the welfare of the animals. However potential issues, physiological or technical would not always allow for these measurements to be taken in time. The data provided have been collected from matching time points. In addition there were no data collected on piglet a(gA).

Appendix F – *Critical Values for Pearson's correlation r'*

	Level of Significance for a Two-Tailed Test (p value)					
df	0.2	0.1	0.05	0.02	0.01	0.001
1	0.951	0.988	0.997	0.9995	0.9999	0.999999
2	0.8	0.9	0.95	0.98	0.99	0.999
3	0.687	0.805	0.878	0.934	0.959	0.991
4	0.608	0.729	0.811	0.882	0.917	0.974
5	0.551	0.669	0.755	0.833	0.875	0.951
6	0.507	0.621	0.707	0.789	0.834	0.925
7	0.472	0.582	0.666	0.75	0.798	0.898
8	0.443	0.549	0.632	0.715	0.765	0.872
9	0.419	0.521	0.602	0.685	0.735	0.847
10	0.398	0.497	0.576	0.658	0.708	0.823
11	0.38	0.476	0.553	0.634	0.684	0.801
12	0.365	0.457	0.532	0.612	0.661	0.78
13	0.351	0.441	0.514	0.592	0.641	0.76
14	0.338	0.426	0.497	0.574	0.623	0.742
15	0.327	0.412	0.482	0.558	0.606	0.725
16	0.317	0.4	0.468	0.542	0.59	0.708
17	0.308	0.389	0.456	0.529	0.575	0.693
18	0.299	0.378	0.444	0.515	0.561	0.679
19	0.291	0.369	0.433	0.503	0.549	0.665
20	0.284	0.36	0.423	0.492	0.537	0.652
21	0.277	0.352	0.413	0.482	0.526	0.64
22	0.271	0.344	0.404	0.472	0.515	0.629
23	0.265	0.337	0.396	0.462	0.505	0.618
24	0.26	0.33	0.388	0.453	0.496	0.607
25	0.255	0.323	0.381	0.445	0.487	0.597
26	0.25	0.317	0.374	0.437	0.479	0.588
27	0.245	0.311	0.367	0.43	0.471	0.579
28	0.241	0.306	0.361	0.423	0.463	0.57
29	0.237	0.301	0.355	0.416	0.456	0.562
30	0.233	0.296	0.349	0.409	0.449	0.554
40	0.202	0.257	0.304	0.358	0.393	0.49
60	0.165	0.211	0.25	0.295	0.325	0.408
120	0.117	0.15	0.178	0.21	0.232	0.294
∞	0.057	0.073	0.087	0.103	0.114	0.146

where df=n-2 (n, number of data points). NB: Infinite was calculated at df=500.

References

[1] S. D. Wolff and R. Balaban, "Nmr imaging of labile proton exchange," *Journal of magnetic resonance*, vol. 86, p. 164:169, 1990.

[2] V. Guivel-Scharen, T. Sinnwell, S. D. Wolff, and R. Balaban, "Detection of proton chemical exchange between metabolite and water in biological tissues," *Journal o Magnetic Resonance*, vol. 133, p. 36:45, 1998.

[3] K. M. Ward, A. H. Aletras, and R. S. Balaban, "A new class of contrast agents for mri based on proton chemical exchange dependent saturation transfer (cest)," *Journal of Magnetic Resonance*, vol. 143, p. 79:87, 2000.

[4] K. Ward and R. Balaban, "Determination of ph using water protons and chemical exchange dependent saturation transfer (cest)," *Magnetic Resonance in Medicine*, vol. 44, p. 799–802, 2000.

[5] P. Z. Sun, T. Benner, A. Kumar, and A. G. Sorensen, "Investigation of optimizing and translating ph-sensitive pulsed-chemical exchange saturation transfer (cest) imaging to a 3t clinical scanner," *Magnetic Resonance in Medicine*, vol. 60, no. 4, pp. 834–841, Oct 2008. [Online]. Available: http://dx.doi.org/10.1002/mrm.21714

[6] P. Z. Sun, E. Wang, X. Cheung, J. S. ans Zhang, T. Benner, and A. G. Sorensen, "Simulation and optimisation of pulsed radio frequency irradiation scheme for chemical exchange saturation transfer (cest) mri-demonstration of ph-weighted pulsed-amide proton cest mri in an animal model of acute cerebral ischemia," *Magnetic Resonance in Medicine*, vol. 66(4), pp. 1042–1048, 2011.

[7] P. Z. Sun and A. G. Sorensen, "Imaging ph using the chemical exchange saturation transfer (cest) MRI: Correction of concomitant RF irradiation effects to quantify cest MRI for chemical exchange rate and ph," *Magnetic Resonance in Medicine*, vol. 60, no. 2, pp. 390–397, Aug 2008. [Online]. Available: http://dx.doi.org/10.1002/-mrm.21653

[8] P. Z. Sun, J. Zhou, J. Huang, and P. van Zijl, "Simplified quantitative description of amide proton transfer (apt) imaging during acute ischemia," *Magnetic*

Resonance in Medicine, vol. 57, no. 2, pp. 405–410, Feb 2007. [Online]. Available: http://-dx.doi.org/10.1002/mrm.21151

[9] J. Zhou, J.-F. Payen, D. A. Wilson, R. J. Traystman, and P. C. M. Van Zijl, "Using the amide proton signal of intracellular proteins and peptides to detect ph effects in mri," *Nature Medicine*, vol. 9(8), pp. 1085–1090, 2003.

[10] P. Z. Sun, J. Zhou, W. Sun, J. Huang, and P. C. van Zijl, "Detection of the ischemic penumbra using ph-weighted mri," *Journal of Cerebral Blood Flow & Metabolism*, vol. 1-8, 2006.

[11] J. Zhou, B. Lal, D. A. Wilson, J. Laterra, and P. C. van Zijl, "Amide proton transfer (apt) contrast for imaging of brain tumors," *Magnetic Resonance in Medicine*, vol. 50, no. 6, pp. 1120–1126, Dec 2003. [Online]. Available: http://dx.doi.org/10.1002/-mrm.10651

[12] A. Salhotra, B. Lal, J. Laterra, P. Z. Sun, P. C. M. van Zijl, and J. Zhou, "Amide proton transfer imaging of 9l gliosarcoma and human glioblastoma xenografts," *NMR in Biomedicine*, vol. 21, no. 5, pp. 489–497, Jun 2008. [Online]. Available: http://-dx.doi.org/10.1002/nbm.1216

[13] J. Zhou, E. Tryggestad, Z. Wen, B. Lal, T. Zhou, R. Grossman, S. Wang, K. Yan, D.-X. Fu, E. Ford, B. Tyler, J. Blakeley, J. Laterra, and P. C. M. van Zijl, "Differentiation between glioma and radiation necrosis using molecular magnetic resonance imaging of endogenous proteins and peptides," *Nature Medicine*, vol. 17(1), pp. 130–4, 2010.

[14] P. C. M. van Zijl, C. K. Jones, J. Ren, C. R. Malloy, and A. D. Sherry, "Mri detection of glycogen in vivo by using chemical exchange saturation transfer imaging (glycocest)," *Proceedings of the National Academy of Sciences*, vol. 104, no. 11, pp. 4359–4364, Mar 2007. [Online]. Available: http://dx.doi.org/10.1073/pnas.0700281104

[15] W. Ling, R. Regatte, G. Navon, and A. Jerschow, "Assesment of glucosaminoglycan concentration in-vivo by chemical exchange-dependent saturation transfer (gagcest)," *Proceedings of the National Academy of sciences*, vol. 105 (7), pp. 2266–2270, 2007.

[16] K. W. Y. Chan, M. T. McMahon, Y. Kato, G. Liu, J. W. M. Bulte, Z. M. Bhujwalla, D. Artemov, and P. C. M. van Zijl, "Natural d -glucose as a biodegradable MRI contrast agent for detecting cancer," *Magnetic Resonance in Medicine*, vol. 68, no. 6, pp. 1764–1773, Dec 2012. [Online]. Available: http://dx.doi.org/10.1002/mrm.24520

[17] S. Walker-Samuel, R. Ramasawmy, F. Torrealdea, M. Rega, V. Rajkumar, S. P. Johnson, S. Richardson, M. Gonçalves, H. G. Parkes, E. Årstad, D. L. Thomas, R. B. Pedley, M. F. Lythgoe, and X. Golay, "In vivo imaging of glucose uptake and metabolism in tumors," *Nature medicine*, vol. 19(8), pp. –, 2013.

[18] F. A. Nasrallah, G. Page, P. W. Kuchel, X. Golay, and K.-H. Chuang, "Imaging brain deoxyglucose uptake and metabolism by glucocest mri," *Journal of Cerebral Blood Flow & Metabolism*, vol. 33, p. 1270–1278, 2013.

[19] M. Rivlin, I. Tsarfaty, and G. Navon, "Functional molecular imaging of tumors by chemical exchange saturation transfer mri of 3-o-methyl-d-glucose," *Magnetic Resonance in Medicine*, vol. 72(4), pp. –, 2014.

[20] K. Cai, M. Haris, A. Singh, F. Kogan, J. H. Greenberg, H. Hariharan, J. A. Detre, and R. Reddy, "Magnetic resonance imaging of glutamate," *Nature Medicine*, vol. 18, no. 2, pp. 302–306, Jan 2012. [Online]. Available: http://dx.doi.org/10.1038/nm.2615

[21] F. Kogan, M. Haris, A. Singh, K. Cai, C. Debrosse, R. P. R. Nanga, H. Hariharan, and R. Reddy, "Method for high-resolution imaging of creatine in vivo using chemical exchange saturation transfer," *Magnetic Resonance in Medicine*, vol. 71, no. 1, pp. 164–172, Jan 2014. [Online]. Available: http://dx.doi.org/10.1002/mrm.24641

[22] M. Haris, A. Singh, K. Cai, F. Kogan, J. McGarvey, C. DeBrose, G. A. Zsido, W. R. T. Witschey, K. Koomalsingh, J. J. Pilla, J. A. Chirinos, V. A. Ferrari, J. H. Gorman, H. Hariharan, R. C. Gorman, and R. Reddy, "A technique for in-vivo mapping of myocardial creatine kinase metabolism," *Nature medicine*, vol. 20(2), pp. –, 2014.

[23] S. Aime, A. Barge, M. Botta, A. S. De Sousa, and D. Parker, "Direct nmr spectroscopic observation of a lanthanide-coordinated water molecule whose

exchange rate is dependent on the conformation of the complexes," *Angewandte Chemie, International Edition*, vol. 37 (19), p. 2673, 1998.

[24] M. Woods, D. E. Woessner, and A. D. Sherry, "Paramagnetic lanthanide complexes as paracest agents for medical imaging," *Chemical Society Reviews*, vol. 35, no. 6, p. 500, 2006. [Online]. Available: http://dx.doi.org/10.1039/b509907m

[25] A. D. Sherry and M. Woods, "Chemical exchange saturation transfer contrast agents for magnetic resonance imaging," *Annual Review of Biomedical Engineering*, vol. 10, no. 1, pp. 391–411, Aug 2008. [Online]. Available: http://dx.doi.org/10.1146/-annurev.bioeng.9.060906.151929

[26] S. Zhang, C. R. Malloy, and A. D. Sherry, "Mri thermometry based on paracest agents," *Journal of the American Chemical Society*, vol. 127, no. 50, pp. 17572–17573, Dec 2005. [Online]. Available: http://dx.doi.org/10.1021/ja053799t

[27] L. Schroder, T. J. Lowery, D. E. Wemmer, and A. Pines, "Molecular imaging using a targeted magnetic resonance hyperpolarized biosensor," *Science*, vol. 314, pp. 446–449, 2006.

[28] L. Schroder, L. Chavez, T. Meldrum, M. Smith, T. J. Lowery, D. E. Wemmer, and A. Pines, "Temperature-controlled molecular depolarization gates in nuclear magnetic resonance," *Angewandte Chemie, International Edition*, vol. 41, pp. 4316–4320, 2008.

[29] F. Schilling, L. Schroder, K. K. Palaniappan, S. Zapf, D. E. Wemmer, and A. Pines, "Mri thermometry based on encapsulated hyperpolarized xenon," *Chemical physics and physical chemistry*, vol. 11, pp. 3529–3533, 2010.

[30] G. Liu, X. Song, K. W. Y. Chan, and M. T. McMahon, "Nuts and bolts of chemical exchange saturation transfer MRI," *NMR in Biomedicine*, vol. 26, no. 7, pp. 810–828, Jul 2013. [Online]. Available: http://dx.doi.org/10.1002/nbm.2899

[31] F. Bloch, W. W. Hansen, and M. Packard, "Nuclear induction," *Physical review letters*, vol. 69, p. 127, 1946.

[32] E. M. Purcell, H. C. Torrey, and R. V. Pound, "Resonance absorption by nuclear magnetic moments in a solid," *Physical Review Letters*, vol. 69, p. 37, 1945.

[33] P. C. Lauterbur, "Image formation by induced local interactions: Examples employing nuclear magnetic resonance," *Nature*, vol. 242, p. 190:191, 1973.

[34] B. E. D., "A brief history of nuclear magnetic resonance," *American chemical society*, vol. 65, p. 295, 1993.

[35] A. C. Guyton, *Textbook of medical physiology*. W. B. Saunders company, 5th edition, 1976.

[36] V. A. Dubinskaya, L. Sun Eng, L. B. Rebrow, and V. A. Bykov, "Comparative study of the state of water in various human tissues," *Bulletin of Experimental Biology and Medicine*, vol. 144 (3), pp. 294–297, 2007.

[37] E. M. Haacke, R. B. Brown, M. R. Thompson, and R. Venkatesan, *Magnetic resonance imaging. Physical principles and sequence design*. Wiley Blackwell (John Wiley & Sons), 1999.

[38] P. T. Callaghan, *Principles of Nuclear Magnetic Resonance Spectroscopy*, P. T. Callaghan, Ed. Clarendon press, Oxford, 1991.

[39] R. A. De Graaf, *In-vivo NMR Spectroscopy. Principles and Technique*, R. A. De Graaf, Ed. John Willey & Sons, 2nd edition, 2007.

[40] G. Gornilescu and A. Bax, "Measurement of proton, nitrogen and carbonyl chemical shielding anisotropies in a protein dissolved in a dilute liquid crystalline phase," *Journal of the American chemical society*, vol. 122(41), pp. 10143–10154, 2000.

[41] M. J. Fluss and J. N. Mundy, *Solid State: Nuclear Methods*, J. N. Mundy, S. J. Rothman, M. J. Fluss, and L. C. Smedskjaer, Eds. Academic Press, INC, 1983.

[42] M. J. Winter, "Diffusion cartograms for the display of periodic table data," *Journal of Chemical Education*, vol. 88, no. 11, p. 1507:1510, Nov 2011. [Online]. Available: http://dx.doi.org/10.1021/ed1000203

[43] J. H. Simpson, *Organic Structure Determination Using 2-D NMR Spectroscopy: A Problem based approach*, J. H. Simpson, Ed. Elsevier, 2012.

[44] S. W. Englander, N. W. Downer, and H. Teitelbaum, "Hydrogen exchange," *Annual Review of Biochemistry*, vol. 41, pp. 903–924, 1972.

[45] P. C. M. van Zijl and N. N. Yadav, "Chemical exchange saturation transfer (cest): What is in a name and what isnt?" *Magnetic Resonance in Medicine*, vol. 65, no. 4, pp. 927–948, Apr 2011. [Online]. Available: http://dx.doi.org/10.1002/mrm.22761

[46] M. Haris, R. P. R. Nanga, A. Singh, K. Cai, F. Kogan, H. Hariharan, and R. Reddy, "Exchange rates of creatine kinase metabolites: feasibility of imaging creatine by chemical exchange saturation transfer MRI," *NMR Biomed.*, vol. 25, no. 11, pp. 1305–1309, Mar 2012. [Online]. Available: http://dx.doi.org/10.1002/nbm.2792

[47] T. Jin, P. Wang, X. Zong, and S.-G. Kim, "Magnetic resonance imaging of the amine-proton exchange (apex) dependent contrast," *NeuroImage*, vol. 59, no. 2, pp. 1218–1227, Jan 2012. [Online]. Available: http://dx.doi.org/10.1016/-j.neuroimage.2011.08.014

[48] A. Bar-Shir, G. Liu, Y. Liang, N. N. Yadav, M. T. McMahon, P. Walczak, S. Nimmagadda, M. G. Pomper, M. M. Tallman, P. C. M. Van Zijl, J. W. Bulte, and A. A. Gilad, "Transforming thymidine into a magnetic resonance imaging probe for monitoring gene expression," *Journal of American Chemical Society*, vol. 135 (4), pp. 1617–1624, 2013.

[49] R. M. Henkelman, X. Huang, Q.-S. Xiang, G. J. Stanisz, S. D. Swanson, and M. J. Bronskill, "Quantitative interpretation of magnetization transfer," *Magnetic Resonance in Medicine*, vol. 29(6), pp. 759–66, 1993.

[50] R. M. Henkelman, G. J. Stanisz, and S. J. Graham, "Magnetization transfer in MRI: a review," *NMR in Biomedicine*, vol. 14, no. 2, pp. 57–64, Apr 2001. [Online]. Available: http://dx.doi.org/10.1002/nbm.683

[51] B. Halle, "Cross-relaxation between macromolecular and solvent spins: The role of long-range dipole couplings," *Journal of chemical physics*, vol. 119(23), p. 12372:12385, 2003.

[52] J. Xu, N. N. Yadav, A. Bar-Shir, C. K. Jones, K. W. Y. Chan, J. Zhang, P. Walczak, M. T. McMahon, and P. C. M. van Zijl, "Variable delay multi-pulse train

for fast chemical exchange saturation transfer and relayed-nuclear overhauser enhancement MRI," *Magnetic Resonance in Medicine*, vol. 71, no. 5, pp. 1798–1812, Jun 2013. [Online]. Available: http://dx.doi.org/10.1002/mrm.24850

[53] G. J. Stanisz, "Relaxation mechanism in collagen rich tissues," in *Proceedings of International society of Magnetic Resonance in Medicine*, 2000(18).

[54] K. L. Desmond and G. J. Stanisz, "ph mapping based on the ratiometric amide and amine relation from endogenous cest," in *OctoberCEST: The third international workshop on chemical exchange saturation transfer imaging*, 2012.

[55] R. Wu, C. Liu, P. K. Liu, and P. Z. Sun, "Improved measurement of labile proton concentration-weighted chemical exchange rate with experimental factor-compensated t1-normalized quantitative chemical exchange saturation transfer (cest) mri," *Contranst media molecular imaging*, vol. 7(4), pp. 384–389, 2012.

[56] F. Torrealdea, M. Rega, M. F. Lythgoe, D. L. Thomas, S. Walker-Samuel, and X. Golay, "Investigation of cest effects in hexoses and pentoses of the glycolytic pathway," in *Proceedings of international society of magnetic resonance Imaging*, 2012 (20).

[57] R. G. Bryant, "The nmr time scale," *Journal of Chemical Education*, vol. 60 (11), pp. 933–935, 1983.

[58] M. L. Garcia-Martin, G. V. Martinez, N. Raghunand, A. D. Sherry, S. Zhang, and R. J. Gillies, "High resolution phe imaging of rat glioma using ph-dependent relaxivity," *Magnetic Resonance in Medicine*, vol. 55(2), pp. 309–315, 2006.

[59] N. McVicar, A. X. Li, D. F. Goncalves, M. Bellyou, S. O. Meakin, M. A. M. Prado, and R. Bartha, "Quantitative tissue ph measurement during cerebral ischemia using amine and amide concentration-independent detection (aacid) with mri," *Journal of Cerebral Blood Flow & Metabolism*, vol. -, pp. 1–9, 2014.

[60] K. L. Desmond, F. Moosvi, and G. J. Stanisz, "Mapping of amide, amine, and aliphatic peaks in the cest spectra of murine xenografts at 7 t," *Magnetic Resonance in Medicine*, vol. -, pp. –, May 2013. [Online]. Available: http://dx.doi.org/10.1002/-mrm.24822

[61] M. Rega, F. Torrealdea, A. Bainbridge, D. Price, M. Sokolska, K. Broad, G. Kawano, M. Ezatti, I. Fierrens, A. Oliver-Taylor, C. Uria-Avellanal, S. Walker-Samuel, D. L. Thomas, N. J. Robertson, and X. Golay, "Validation of apt as a measure of ph by 31p in a piglet model of hie," in *Proceedings of International society of Magnetic Resonance in Medicine*, 2014.

[62] J. Zhou and P. C. M. Van Zijl, "Chemical exchange saturation transfer imaging and spectroscopy," *Progress in Nuclear Magnetic Resonance Spectroscopy*, vol. 48 (2), pp. 109–136, 2006.

[63] M. Eigen, "Proton transfer, acid-base catalysis, and enzymatic hydrolysis," *Angewandte Chemie, International Edition*, vol. 3(1), pp. 1–72, 1964.

[64] E. Tuchsen and E. Woodward, "Mechanism of surface peptide proton exchange in bovine pancreatic trypsin inhibitor. salt effects and o-protonation," *Journal of Molecular Biology*, vol. 185, pp. 421–430, 1985.

[65] D. W. McRobbie, E. A. Moore, M. J. Graves, and M. R. Price, *MRI from picture to Proton*. Cambridge University Press, 2006.

[66] K. L. Desmond and G. J. Stanisz, "Understanding quantitative pulsed cest in the presence of mt," *Magnetic Resonance in Medicine*, vol. 67, no. 4, pp. 979–990, Apr 2012. [Online]. Available: http://dx.doi.org/10.1002/mrm.23074

[67] P. Z. Sun, P. C. van Zijl, and J. Zhou, "Optimization of the irradiation power in chemical exchange dependent saturation transfer experiments," *Journal of Magnetic Resonance*, vol. 175, no. 2, pp. 193–200, Aug 2005. [Online]. Available: http://-dx.doi.org/10.1016/j.jmr.2005.04.005

[68] P. Z. Sun, "Simplified and scalable numerical solution for describing multi-pool chemical exchange saturation transfer (cest) MRI contrast," *Journal of Magnetic Resonance*, vol. 205, no. 2, pp. 235–241, Aug 2010. [Online]. Available: http://-dx.doi.org/10.1016/j.jmr.2010.05.004

[69] M. Zaiss, J. Xu, S. Goerke, I. S. Khan, R. J. Singer, J. C. Gore, D. F. Gochberg, and P. Bachert, "Inverse z -spectrum analysis for spillover-, mt-, and t 1 -corrected steady-state pulsed cest-MRI - application to ph-weighted MRI of acute stroke," *NMR*

in Biomedicine, pp. n/a–n/a, Dec 2013. [Online]. Available: http://dx.doi.org/10.1002/-nbm.3054

[70] T. Jin, P. Wang, X. Zong, and S.-G. Kim, "Mr imaging of the amide-proton transfer efect and the ph-insensitive nuclear overhauser effect at 9.4t," *Magnetic Resonance in Medicine*, vol. 69, pp. 760–770, 2013.

[71] J. Närväinen, P. L. Hubbard, R. A. Kauppinen, and G. A. Morris, "Z-spectroscopy with alternating-phase irradiation," *Journal of Magnetic Resonance*, vol. 207, p. 242–250, 2010.

[72] A. N. Dula, S. A. Smith, and J. C. Gore, "Application of chemical exchange saturation transfer (cest) MRI for endogenous contrast at 7 tesla," *Journal of Neuroimaging*, vol. 23, no. 4, pp. 526–532, Oct 2013. [Online]. Available: http://-dx.doi.org/10.1111/j.1552-6569.2012.00751.x

[73] K. Snoussi, J. W. Bulte, M. Gueron, and P. C. M. Van Zijl, "Sensitive cest agents based on nucleic acid imino proton exchange: detection of poly(ru) and of a dendrimer-poly(ru) model for nucleic acid delivery and pharmacology," *Magnetic Resonance in Medicine*, vol. 49, pp. 998–1005, 2003.

[74] M. Zais and P. Bachert, "Chemical exchange saturation transfer (cest) and mr z-spectroscopy in-vivo: a review of theoretical approachs and methods," *Physics in Medicine and Biology*, vol. 58, pp. 221–269, 2013.

[75] M. A. Bernstein, K. F. King, and X. J. Zhou, *Handbook of MRI pulse sequences*, M. A. Bernstein, K. F. King, and X. J. Zhou, Eds. Elsevier, 2004.

[76] G. Liu, M. M. Ali, B. Yoo, M. A. Griswold, J. A. Tkach, and M. D. Pagel, "Paracest mri with improved temporal resolution," *Magnetic Resonance in Medicine*, vol. 61(2), pp. 399–408, 2009.

[77] P. Z. Sun, C. T. Farrar, and A. G. Sorensen, "Correction for artefacts induced by b0 and b1 field inhomogeneities in ph-sensitive chemical exchange saturation transfer (cest)," *Magnetic Resonance in Medicine*, vol. 58(6), pp. 1207–1215, 2007.

[78] A. N. Dulla, E. M. Asche, B. A. Landman, S. Welch, K. M.and Pawate, S. Sriram, J. C. Gore, and S. A. Smith, "Development of chemical exchange saturation transfer (cest) at 7t," *Magnetic Resonance in Medicine*, vol. 66(3), pp. 831–838, 2012.

[79] G. J. Stanisz, E. E. Odrobina, J. Pun, M. Escaravage, S. J. Graham, M. J. Bronskill, and R. M. Henkelman, "T1, t2 relaxation and magnetization transfer in tissue at 3t," *Magnetic Resonance in Medicine*, vol. 54, no. 3, pp. 507–512, Sep 2005. [Online]. Available: http://dx.doi.org/10.1002/mrm.20605

[80] M. Zais, B. Schmitt, and P. Bachert, "Quantitative separateration of cest effect from magnetization transfer and spillover-effects by lorentzian-line-fit analysis of z-spectra," *Journal of magnetic resonance*, vol. 211, p. 149:155, 2011.

[81] N. N. Yadav, K. W. Y. Chan, C. K. Jones, M. T. McMahon, and P. C. M. van Zijl, "Time domain removal of irrelevant magnetization in chemical exchange saturation transfer z-spectra," *Magnetic Resonance in Medicine*, vol. 70, no. 2, pp. 547–555, Aug 2013. [Online]. Available: http://dx.doi.org/10.1002/mrm.24812

[82] M. Zais, P. Kunz, S. Goerke, A. Radbruch, and P. Bachert, "Mr imaging of protein folding in vitro employing nuclear-overhauser-mediated saturation transfer," *NMR in Biomedicine*, vol. 26, pp. 1815–1822, 2013.

[83] W. M. Bump, "The normal curve takes many forms: A review of skewness and kurtosis," in *Southwest Educational Research Association, San Antonio*, 1991.

[84] P. J. Curran and S. G. West, "The robustness of test statistics to nonnormality and specification error in confirmatory factor analysis," *Physiological Methods*, vol. 1, pp. 16–39, 1996.

[85] A. A. Neath and J. E. Cavanaugh, "The bayesian information criterion: background, derivation and applications," *Wires Computational statistics*, vol. 4 (2), pp. 199–203, 2011.

[86] S. Walker-Samuel, S. P. Johnson, R. B. Pedley, M. F. Lythgoe, and X. Golay, "Extracranial measurement of amide proton transfer using exchange-modulated point-resolved spectroscopy (express)," *NMR in Biomedicine*, vol. 25 (6), p. 829:834, 2012.

[87] M. Bilgen, B. Al-Hafez, N. E. J. Berman, and B. Festoff, "Magnetic resonance imaging of mouse spinal cord," *Magnetic Resonance in Medicine*, vol. 54, pp. 1226–1231, 2005.

[88] A. J. Ninfa, D. P. Ballou, and M. Benore, *Fundamental Laboratory Approach for Biochemistry and Biotechnology*. John Willey & Sons, 2nd edition, 2009.

[89] M. Watanabe, M. Dykes-Hoberg, V. C. Culotta, D. L. Price, P. C. Wong, and J. D. Rothstein, "Histological evidence of protein aggregation in mutant sod1 transgenic mice and in amyotrophic lateral sclerosis neural tissues," *Neurobiology of Disease*, vol. 8, p. 933–941, 2001.

[90] C. A. Ross and M. A. Poirier, "Protein aggregation and neurodegenerative disease," *nature medicine*, vol. 10, p. 10:17, 2004.

[91] A. Radunovic and P. N. Leigh, "Alsodatabase: datadata of sod1 (and other) gene mutations in als on the internet. european fals group and alsod consortium," *Amyotrophic Lateral Sclerosis and Other Motor Neuron Disorders*, vol. 1, pp. 45–49, 1999.

[92] R. Wroe, A. W. L. Butler, P. M. Andersen, J. F. Powel, and A. Al-Chalabi, "Alsod: The amyotrophic lateral sclerosis online database," *Amyotrophic Lateral Sclerosis*, vol. 9 (4), pp. 249–250, 2008.

[93] R. Etzioni, N. Urban, S. Ramsey, M. McIntosh, S. Schwartz, B. Reid, J. Radich, G. Anderson, and L. Hartwell, "The case for early detection," *Nature reviews Cancer*, vol. 3, pp. 243–252, 2003.

[94] P. M. Andersen, "Amyotrophic lateral sclerosis associated with mutations cu/zn superoxide dismutase gene." *Current Neurology and Neuroscience Reports*, vol. 6, pp. 37–46, 2006.

[95] P. K. Andrus, T. J. Fleck, M. E. Gurney, and E. D. Hall, "Protein oxidative damage in a transgenic mouse model of familial amyotrophic lateral sclerosis," *Journal of Neurochemistry*, vol. 71, p. 2041:2048, 1998.

[96] M. C. Dal Canto and M. E. Gurney, "A low expexpress line of transfgenic mice carrying a mutant human cu,zn superoxide dismutase (sod1) gene develop

pathological changes that most closely resemble those in human amyotrophic lateral sclerosis," *Acta neuropathologica*, vol. 93 (6), pp. 537–550, 1997.

[97] M. E. Gurney, A. Y. Chiu, M. C. Dal Canto, C. Y. Polchow, D. D. Alexander, J. Caliendo, A. Hentati, Y. W. Kwon, and H. K. Deng, "Motor neuron degeneration in mice that express a human cu,zn superoxide dismutase mutation," *Science*, vol. 264 (5166), pp. 1772–1775, 1994.

[98] H. Niessen, F. Angenstein, K. Sander, W. Kunz, M. Teuchert, A. Ludolph, H. Heinze, H. Sceich, and S. Vielhaber, "In vivo quantification of spinal and bulbar motor neuron degeneration in the g93a-sod1 transgenic mouse model of als by t2 relaxation time and apparent diffusion coefficient," *Experimental Neurology*, vol. 201, no. 2, pp. 293–300, Oct 2006. [Online]. Available: http://dx.doi.org/10.1016/-j.expneurol.2006.04.007

[99] P. Weydt, S. Y. Hong, M. Kliot, and T. Moller, "Assessing disease onset and progression in the sod1 mouse model of als," *Neuroreport*, vol. 14(7), pp. –, 2003.

[100] L. I. Bruijn, M. W. Becher, M. K. Lee, K. L. Anderson, N. A. Jenjins, N. G. Copeland, S. S. Sisodia, J. D. Rothstein, D. R. Borchelta, D. L. Price, and D. W. Cleveland, "Als-linked sod1 mutant g85r mediates damage to astrocytes and promote rapidly progressive disease with sod1- containing inclusions," *Neuron*, vol. 18, p. 327:338, 1997.

[101] D. Kieran, I. Woods, A. Villunger, A. Strasser, and J. H. M. Prehn, "Deletion of the bh3-only protein puma protects motoneurons from er stress-induced apoptosis and delays motoneuron loss in als mice," *Proceedings of the National Academy of sciences*, vol. 104, p. 20606:20611, 2007.

[102] S. B. Prusiner, R. Tycko, J. Greenwald, S. K. Fritschi, C. Duran-Aniotz, and F. Clavaguera, *Proteopathic Seeds and Neurodegenerative Diseases*, M. Jucker and Y. Christen, Eds. Springer, 2013.

[103] S. Kumar and J. Walter, "Phosphorylation of amyloid beta (ab) peptides - a trigger for formation of toxic aggregates in alzheimer's disease," *Aging*, vol. 3 (8), pp. –, 2011.

[104] C. M. Karcha, M. Prudencioa, D. D. Winklerb, P. J. Hartb, and D. R. Borchelta, "Role of mutant sod1 disulphide oxidation and aggregation in the pathogenesis of familial als," *Proceedings of the National Academy of Sciences*, vol. 106 (19), p. 7774–7779, 2009.

[105] M. Dorival and A. M. English, "Sod1 oxidation and formation of soluble aggregates in yeast: Relevance to sporadic als development," *Radox Biology*, vol. 2, pp. 632–639, 2014.

[106] G. S. A. Wright, S. V. Antonyuk, N. M. Kershaw, R. W. Strange, and S. S. Hasnian, "Ligand binding and aggregation of pathogenic sod1," *Nature communications*, vol. 4, p. 1758, 2012.

[107] B. Kalmar, S. Novoselov, A. Gray, M. E. Cheetham, B. Margulis, and L. Greensmith, "Late stage treatment with arimoclomol delays disease progression and prevents protein aggregation in the sod1-g93a mouse model of als," *Journal of Neurochemistry*, vol. 107 (2), p. 339:350, 2008.

[108] L. G. Bilsland, J. R. T. Dick, G. Pryce, S. Petrosino, V. Di Marzo, D. Baker, and L. Greensmith, "Increasing cannabinoid levels by pharmacological and genetic manipulation delays disease progression in sod1 mice," *The FASEB Journal*, vol. 20 (7), p. 1003:1005, 2006.

[109] D. Liu, J. Zhou, R. Xue, Z. Zuo, J. An, and D. J. J. Wang, "Quantitative characterization of nuclear overhauser enhancement and amide proton transfer effects in the human brain at 7 tesla," *Magnetic Resonance in Medicine*, vol. 70, pp. 1070–1081, 2013.

[110] A. R. La Spada, "Spinal and bulbar muscular atrophy," Ph.D. dissertation, University of California, San Diego school of Medicine, 1999.

[111] B. Malik, N. Nirmalananthan, A. Gray, A. R. La Spada, M. G. Hanna, and L. Greensmith, "Co-induction of heat shock response ameliorates disease progression in a mouse model of human spinal and bulbar muscular atrophy: implication for the therapy," *Brain*, vol. 136, pp. 926–943, 2013.

[112] H. Banno, H. Adachi, M. Katsuno, K. Suzuki, N. Atsuta, H. Watanabe, F. Tanaka, M. Doyu, and G. Sobue, "Mutant androgen receptor accumulation in spinal and bulbar muscular atrophy scrotal skin: a pathogenic marker," *Annals of neurology*, vol. 59(3), p. 520:526, 2006.

[113] B. L. Sopher, P. S. Thomas, M. A. LaFevre-Bernit, C. B. Ware, L. Jun, R. T. Libby, L. M. Ellerby, and A. R. La Spada, "Androgen receptor yac trasngenic mice recapitulate sbma motor neuronopathy and implicate vegf164 in the motor neuron degeneration," *Neuron*, vol. 41, p. 687:699, 2004.

[114] H. T. Orr and H. Y. Zoghbi, "Trinucleotide repeat disorders," *Annual Review of Neuroscience*, vol. 30, pp. 575–621, 2007.

[115] H. Banno, M. Katsuno, K. Suzuki, Y. Takeuchi, M. Kawashima, N. Suga, M. Takamori, M. Ito, T. Nakamura, K. Matsuo, S. Tamada, Y. Oki, H. Adachi, M. Minamiyama, M. Waza, N. Atsuta, H. Watanabe, Y. Fujimoto, T. Nakashima, F. Tanaka, M. Doyu, and G. Sobue, "Phase 2 trial of leuprorelin in patients with spinal and bulbar muscular atrophy," *Annals of neurology*, vol. 65 (2), pp. 140–150, 2009.

[116] M. Katsuno, H. Adachi, M. Doyu, M. Minamiyama, C. Sang, Y. Kobayashi, A. Inukai, and G. Sobue, "Leuprorelin rescues polyglutamine-dependent phenotypes in a transgenic mouse model of spinal and bulbar muscular atrophy," *Nature medicine*, vol. 9 (6), pp. 768–773, 2003.

[117] M. Katsuno, H. Banno, K. Suzuki, Y. Takeuchi, M. Kawashima, I. Yabe, H. Sasaki, M. Aoki, M. Morita, I. Nakano, K. Kanai, M. Ito, K. Ishikawa, H. Mizusawa, T. Yamamoto, S. Tsuji, K. Haseqawa, T. Shimohata, M. Nishizawa, H. Miyalima, F. Kanda, H. Watanabe, T. Nakashima, A. Tsujino, T. Yamashita, M. Uchino, Y. Fujimoto, F. Tanaka, and G. Sobue, "Efficacy and safety of leuprorelin in patients with spinal and bulbar muscular atrophy (jasmitt study): a multicentre, randomised, double-blind, placebo-controlled trial," *Lancet Neurology*, vol. 9 (9), pp. 875–884, 2010.

[118] L. Fernández-Rhodes, A. D. Kokkinis, M. J. White, C. A. Watts, S. Auh, N. Jeffries, J. A. Shrader, T. J. Lehky, L. Li, J. E. Ryder, E. W. Levy, B. I. Solomon, M. O. Harris-Love, A. La Pean, A. B. Schindler, C. Chen, N. A. Di Prospero, and K. Fischbeck, "Efficacy and safety of dutasteride in patients with spinal and bulbar

muscular atrophy: a randomised placebo-controlled trial." *Lancet Neurology*, vol. 10 (2), pp. 140–147, 2011.

[119] T. Jochum, M. E. Ritz, C. Schuster, S. F. Funderburk, K. Jehle, K. Schmitz, F. Brinkmann, M. Hirtz, D. Moss, and A. C. Cato, "Toxic and non-toxic aggregates from the sbma and normal forms of androgen receptor have distinct oligomeric structures," *Biochimica et Biophysica Acta*, vol. 1822 (6), pp. 1070–1078, 2012.

[120] M. Cudkowicz, J. Shefner, E. Simpson, D. Grasso, H. Yu, H. Zhang, A. Shui, D. Schoenfeld, R. Brown, S. Wieland, and J. Barber, "Arimoclomol at dosages up to 300 mg/day is well tolerated and safe in amyotrophic lateral sclerosis," *Muscle Nerve*, vol. 38 (1), pp. 837–844, 2008.

[121] G. Anderson, "What are the age-related changes in the spine?" *Bailliere's Clinical Rheumatology*, vol. 12 (1), pp. 161–173, 1998.

[122] D. L. Dickstein, C. M. Weaver, J. I. Luebke, and P. R. Hof, "Dendritic spine changes associated with normal aging," *Neuroscience*, vol. 251, pp. 21–32, 2013.

[123] A. Comfort, *Natural aging and the effects of radiation (suppl. 1): 216-234*. Radiation Research Society, 1959.

[124] C. M. T. Robertson and M. Perlman, "Follow-up of the term infant after hypoxic-ischemic encephalopathy," *Paediatric Child Health*, vol. 11 (5), p. 278, 2006.

[125] J. J. Kurinczuk, M. White-Koning, and N. Badawi, "Epidemiology of neonatal encephalopathy and hypoxic-ischaemic encephalopathy," *Early Human Development*, vol. 86, no. 6, pp. 329–338, Jun 2010. [Online]. Available: http://dx.doi.org/10.1016/-j.earlhumdev.2010.05.010

[126] E. B. Cady, O. Iwata, A. Bainbridge, J. S. Wyatt, and N. J. Robertson, "Phosphorus magnetic resonance spectroscopy 2 h after perinatal cerebral hypoxia-ischemia prognosticates outcome in the newborn piglet," *Journal of Neurochemistry*, vol. 107, pp. 1027–1035, Oct 2008. [Online]. Available: http://dx.doi.org/10.1111/j.1471-4159.2008.05662.x

[127] M. Chesler, "Failure and function of intracellular ph regulation in acute hypoxic-ischemic injury of astrocytes," *Glia*, vol. 50, no. 4, pp. 398–406, 2005. [Online]. Available: http://dx.doi.org/10.1002/glia.20141

[128] M. Thoresen and A. Whitelaw, "Therapeutic hypothermia for hypoxic-ischemic encephalopathy in the newborn infant," *Current opinion in Neurology*, vol. 18, pp. 111–116, 2005.

[129] N. J. Robertson, S. Faulkner, B. Fleiss, A. Bainbridge, C. Andorka, D. Price, E. Powell, L. Lecky-Thompson, L. Thei, M. Chandrasekaran, and et al., "Melatonin augments hypothermic neuroprotection in a perinatal asphyxia model," *Brain*, vol. 136, no. 1, pp. 90–105, Nov 2012. [Online]. Available: http://dx.doi.org/10.1093/brain/-aws285

[130] R. C. Vannucci, "Current and potentially new management strategies for perinatal hypoxic-ischemic encephalopathy," *Pediatrics*, vol. 85, p. 961, 1990.

[131] N. J. Robertson, F. M. Cowan, I. J. Cox, , and A. D. Edwards, "Brain alkaline intracelular ph after neonatal encephalopathy," *Annals of Neurology*, vol. 52, pp. 732–742, 2002.

[132] A. Lorek, Y. Takei, E. B. Cady, J. S. Whatt, J. Penrice, A. D. Edwards, D. Peebles, M. Wylezinska, H. Owen-Reece, and V. Kirkbride, "Delayed ('secondary') celebral energy failure after acute hypoxia-ischemia in the newborn piglet: continuous 48-hour study by phosphorous magnetic resonance spectroscopy," *Pediatric research*, vol. 36(6), pp. 699–706, 1994.

[133] O. Iwata, J. S. Thornton, M. W. Sellwood, S. Iwata, Y. Sakata, M. A. Noone, F. E., A. Bainbridge, E. De Vita, G. Raivich, and et al., "Depth of delayed cooling alters neuroprotection pattern after hypoxia-ischemia," *Annals of Neurology*, vol. 58, no. 1, pp. 75–87, Jun 2005. [Online]. Available: http://dx.doi.org/10.1002/ana.20528

[134] S. E. Jacobs, C. J. Morley, T. E. Inder, M. J. Steward, K. R. Smith, P. J. McNamara, and I. M. R. e. a. Wright, "Whole-body hypothermia for term and near-term newborns with hypoxic-ischemic encephalopathy," *Archives of Pediatrics and*

Adolescent Medicine, vol. 165, no. 8, p. 692, Aug 2011. [Online]. Available: http://-dx.doi.org/10.1001/archpediatrics.2011.43

[135] M. M. Helmy, E. A. Tolner, S. Vanhatalo, J. Voipio, and K. Kaila, "Brain alkalosis causes birth asphyxia seizures, suggesting therapeutic strategy," *Annals of Neurology.*, vol. 69, no. 3, pp. 493–500, Feb 2011. [Online]. Available: http://dx.doi.org/-10.1002/ana.22223

[136] G. S. Kendall, N. J. Robertson, O. Iwata, D. Peebles, and G. Raivich, "N-methyl-isobutyl-amiloride ameliorates brain injury when commenced before hypoxia ischemia in neonatal mice," *Pediatric Research*, vol. 59, no. 2, pp. 227–231, Feb 2006. [Online]. Available: http://dx.doi.org/10.1203/01.pdr.0000196805.68082.22

[137] J. W. Pan, J. R. Hamm, D. L. Rothman, and R. G. Shulman, "Intracellular ph in human skeletal muscle by 1h and nmr," *Proceedings of the National Academy of sciences*, vol. 85, pp. 7836–7839, 1988.

[138] M. Curtis, A. Manfridi, and G. Biella, "Activity-dependent ph shifts and periodic recurrence and of and spontaneous interictal and spikes in a model and of focal and epileptogenesis," *The Journal of Neuroscience*, vol. 18(18), pp. 7543–7551, 1998.

[139] M. Martinez-Biarge, T. Bregant, C. J. Wusthoff, A. T. Chew, J. Diez-Sebastian, M. A. Rutherford, and F. M. Cowan, "White matter and cortical injury in hypoxic-ischemic encephalopathy: Antecedent factors and 2-year outcome," *The Journal of Pediatrics*, vol. 161, no. 5, pp. 799–807, Nov 2012. [Online]. Available: http://-dx.doi.org/10.1016/j.jpeds.2012.04.054

[140] J. Zhou, K. Yan, and H. Zhu, "A simple model for understanding the origin of the amide proton transfer mri signal in tissue," *Appl Magnetic Resonance*, vol. 4(2), pp. 393–402, 2012.

[141] A. Bainbridge, I. Tachtsidis, S. Faulkner, D. Price, T. Zhu, E. Baer, K. Broad, D. Thomas, E. Cady, N. Robertson, and et al., "Brain mitochondrial oxidative metabolism during and after cerebral hypoxia-ischemia studied by simultaneous phosphorus magnetic-resonance and broadband near-infrared spectroscopy,"

NeuroImage, vol. -, pp. –, Aug 2013. [Online]. Available: http://dx.doi.org/10.1016/-j.neuroimage.2013.08.016

[142] L. Vanhamme, A. Van Den Boogaart, and S. Van Huffel, "Improved method for accurate and efficient quantification of mrs data with use of prior knowledge," *Journal of Magnetic Resonance*, vol. 129 (1), pp. 35–43, 1997.

[143] A. Van Den Boogaart, "Quantitative data analysis of in-vivo mrs data sets," *Magnetic Resonance in Chemistry*, vol. 35, pp. s146–s152, 1997.

[144] P. Mandel and D. Edel-Harth, "Free nucleotides in the rat brain during post-natal development," *Journal of Neurochemistry*, vol. 13, pp. 591–595, 1966.

[145] M. A. Rutherford, *MRI of the Neonatal Brain*, M. A. Rutherford, Ed. Saunders Ltd, 2001.

[146] E. De Vita, A. Bainbridge, P. Cheong, A. Huertas-Ceballos, R. J. Ordidge, and N. J. Robertson, "Localized 4.7t proton magnetic resonance spectroscopy in neonatal encephalopathy: Implementation, safety and preliminary interpretation of results," *Imaging Decisions MRI*, vol. 9(4), pp. 31–41, 2005.

[147] P. Kinchesh and R. J. Ordidge, "Spin-echo mrs in human at high field: Laser localisation using foci pulses," *Journal of Magnetic Resonance*, vol. 175, pp. 30–43, 2005.

[148] M. Garwood and L. DelaBarre, "The return of the frequency sweep: Designing adiabatic pulses for contemporary nmr," *Journal of Magnetic Resonance*, vol. 153, pp. 155–177, 2001.

[149] I. Tkac, Z. Starcuk, I.-Y. Choi, and R. Gruetter, "In-vivo h nmr spectroscopy of rat brain at 1ms echo time," *Magnetic Resonance in Medicine*, vol. 41, pp. 649–656, 1999.

[150] S. Rehncrona, "Brain acidosis," *Annals of Emergency Medicine*, vol. 14 (8), pp. 770–793, 1985.

[151] S. Shah, M. Tracy, and J. Smyth, "Postnatal lactate as an early predictor of short-term outcome after intrapartum asphyxia," *Journal of Perinatology*, vol. 24, pp. 16–20, 2004.

[152] N. Wiberg, K. Kallen, A. Herbst, and P. Olofsson, "Relation between umbilical cord blood ph, base deficit, lactate, 5-minute apgar score and development of hypoxic ishemic encephalopathy," *Acta Obstetrica et Gynaecologica Scandinavia*, vol. 89(10), pp. 1263–1269, 2010.

[153] D. P. Agamanolis, D. J. Brat, E. J. Cochran, M. L. Cohen, D. Dolinak, R. D. Folkerth, K. A. Gyure, H. G. W. Kleinschmidt-DeMasters, B. K. Lidov, and J. D. Miles, *Neuropathology*, J. R. Goldblum, Ed. Elsevier, 2005.

[154] I. Krageloh-Mann, A. Helber, I. Mader, M. Staudt, M. Wolff, F. Groenendaal, and L. DeVries, "Bilateral lesions of thalamus and basal ganglia: origin and outcome," *Developmental Medicine and Child Neurology*, vol. 44, pp. 477–484, 2002.

[155] A. K. Goila and M. Pawar, "The diagnosis of brain death," *Indian Journal of Critical Care Medicine*, vol. 13(1), pp. 7–11, 2009.

[156] H. M. Bramlett and W. D. Dietrich, "Pathophysiology of cerebral ischemia and brain trauma: Similarities and differences," *Journal of cerebral blood flow and metabolism*, vol. 24, pp. 133–150, 2004.

[157] T. Miyazawa, P. Bonnekoh, R. Windmann, and K. A. Hossmann, "Heating of the brain to maintain normothermia during ischemia aggravates brain injury in the rat," *Acta Neuropathologica*, vol. 85(5), pp. 488–494, 1993.

[158] R. Busto, W. D. Dietrich, M. Y. Globus, I. Valdes, P. Scheinberg, and M. D. Ginsberg, "Small differences in intraischemic brain temperature critical determine the extent of ischemic neuronal injury," *Journal of Cerebral Blood Flow & Metabolism*, vol. 7(6), pp. 729–738, 1987.

[159] F. Colbourne, H. Li, and A. M. Buchan, "Indefatigable ca1 sector neuroprotection with mild hypothermia induced 6 hours after severe forebrain ischemia in rats," *Journal of Cerebral Blood Flow & Metabolism*, vol. 19, pp. 742–749, 1998.

[160] A. R. Laptook, L. Shalak, and R. J. Corbett, "Differences in brain temperature and cerebral blood flow during selective head versus whole-body cooling," *Pediatrics*, vol. 108(5), pp. 1103–1110, 2001.

[161] K. Haaland, P. A. Steen, and M. Thoresen, "Cerebral, tympanic and colonic thermometry in the piglet," *Peproduction, fertility and development*, vol. 8(1), pp. 125–128, 1996.

[162] O. Iwata, S. Iwata, M. Tamura, T. Nakamura, M. Suqiura, and Y. Oqiso, "Brain temperature in newborn piglets under selective head cooling with minimal systemic hypothermia," *Pediatric international*, vol. 45(2), pp. 163–168, 2003.

[163] A. Bainbridge, G. S. Kendall, E. D. Vita, C. Hagmann, A. Kapetanakis, E. B. Cady, and N. J. Robertson, "Regional neonatal brain absolute thermometry by 1 h mrs," *NMR Biomed.*, vol. 26, no. 4, pp. 416–423, Oct 2012. [Online]. Available: http://-dx.doi.org/10.1002/nbm.2879

[164] J. Soukup, A. Zauner, E. M. Doppenberg, M. Menzel, C. Gilman, H. F. Young, and R. Bullock, "The importance of brain temperature in patients after severe head injury: relation to intracranial pressure, cerebral perfusion pressure, cerebral blood flow and outcome," *Journal of Neurotrauma*, vol. 19(5), pp. 559–571, 2002.

[165] C. Childs, A. Vail, R. Protheroe, A. T. Kind, and P. M. Dart, "Differences between brain and rectal temperature during routine critical care of patients with severe traumatic brain injury," *Anaesthesia*, vol. 60(8), pp. 759–765, 2005.

[166] M. Pourcyrous, H. Parfenova, H. S. Bada, S. B. Korones, and C. W. Leffler, "Changes in cerebral cyclic nucleotides and cerebral blood flow during prolonged asphyxia and recovery in newborn pigs," *Pediatric research*, vol. 41, pp. 617–623, 1997.

[167] J. L. Pannier and I. Leusen, "Circulation to the brain of the rat during acute and prolonged respiratory changes in the acid-based balance," *European journal of physiology*, vol. 338(4), pp. 347–359, 1973.

[168] N. A. Lassen, "The luxury-perfusion syndrome and its possible relation to acute metabolic acidosis localised within the brain," *The Lancet*, vol. 2, p. 1113, 1966.

[169] B. R. Karlsson, B. Grogaard, B. Gerdin, and P. A. Steen, "The severity of postischemic hypoperfusion increases with duration of cerebral ischemia in rats," *Acta Anaesthesiologica Scandinavica*, vol. 38(3), pp. 248–253, 1994.

[170] K. A. Hossmann, "Reperfusion of the brain after global ischemia: hemodynamic disturbances," *Shock*, vol. 8(2), pp. 95–101, 1997.

[171] B. Peters, M. M. Walka, W. Friedmann, G. Stoltenburg-Didinger, and M. Obladen, "Hypoxic-ischemic encephalopathy with cystic brain stem necrosis and thalamic calcifications in a preterm twin," *Brain & Development*, vol. 22(4), pp. 265–271, 2000.

[172] F. M. Yatsu and S. A. Moss, "Brain lipid changes following hypoxia," *Stroke*, vol. 2, pp. 587–593, 1971.

[173] G. S. Kendall, M. Hristova, V. Zbarsky, A. Clements, D. M. Peebles, N. J. Robertson, and G. Raivich, "Distribution of ph changes in mouse neonatal hypoxic-ischaemic insult," *Developmental Neuroscience*, vol. 33(6), pp. 505–518, 2011.

[174] N. J. Robertson, J. Kuint, S. J. Counsell, M. A. Rutherford, G. A. Coutts, I. J. Cox, and D. Edwards, "Characterization of cerebral white matter damage in preterm infant using 1h and 31p magnetic resonance spectroscopy," *Journal of Cerebral Blood Flow & Metabolism*, vol. 20, pp. 1446–1456, 2000.

[175] W. Kakuda, M. G. Lansberg, V. N. Thijs, S. M. Kemp, R. Bammer, L. R. Wechsler, M. E. Moseley, M. P. Parks, and G. W. Albers, "Optimal definition for pwi/dwi mismatch in acute ischemic stroke patients," *Journal of Cerebral Blood Flow & Metabolism*, vol. 28, no. 5, pp. 887–891, Jan 2008. [Online]. Available: http://dx.doi.org/-10.1038/sj.jcbfm.9600604

[176] P. Z. Sun, J. S. Cheung, E. Wang, and E. H. Lo, "Association between ph-weighted endogenous amide proton chemical exchange saturation transfer MRI and tissue lactic acidosis during acute ischemic stroke," *Journal of Cerebral Blood Flow & Metabolism*, vol. 31, no. 8, pp. 1743–1750, Mar 2011. [Online]. Available: http://-dx.doi.org/10.1038/jcbfm.2011.23

[177] Y. K. Tee, G. W. J. Harston, N. Blockley, W. Okell, J. Levman, F. Sheerin, M. Cellerini, P. Jezzard, J. Kennedy, S. J. Payne, and M. A. Chappell, "Comparing different analysis methods for quantifying the mri amide proton transfer (apt) effect in hyperacute stroke patients," *NMR in Biomedicine*, vol. 27, pp. 1019–1029, 2013.

[178] P. Z. Sun, T. Benner, W. A. Copen, and A. G. Sorensen, "Early experience of translating ph-weighted mri to image human subjects at 3 tesla," *Stroke*, vol. 41, pp. 147–151, 2010.

[179] C. M. Cotten and S. Shankaran, "Hypothermia for hypoxic-ischemic encephalopathy," *Expert Review of Obstetrics and gynecology*, vol. 5(2), pp. 227–239, 2010.

[180] R. J. Corbett, A. R. Laptook, G. Tollefsbol, S. Silmon, and D. Garcia, "Maturational changes in cerebral lactate and acid clearance following ischemia measure in vivo using magnetic resonance spectroscopy and microdialysis," *Brain research. Developmental brain research*, vol. 113(1-2), pp. 37–46, 1999.

List of publications

1. *'Imaging glucose in tumours'*. S. Walker-Samuel, R. Ramasawmy, F. Torrealdea, **M. Rega**, S. P. Johnson, V. Rajkumar, M. Goncalves, E. Arstad, D. Thomas, R. B. Pedley, M. F. Lythgoe, X. Golay. *Nature Medicine , 2013*
2. *'In vivo Imaging of Tau pathology using Multi-Parametric Quantitative MRI'*, JA Wells, JM O'Callaghan, HE Holmes, NM Powel, RA Johnson, S Siow, F Torrealdea, O Ismail, S Walker-Samuel, X Golay, **M Rega**, S Richardson, N Fox, AJ Schwarz, Z Ahmed, TK Murray, MJ O'Neill, EC Collins, N Colgan, MF Lythgoe. *Neuroimage, 2015*

List of abstracts presented in scientific meetings

1. *'Can Amide Proton Transfer MRI give additional information about Huntington's Disease?'* **M. Rega**, J. Fairney, F. Torrealdea, B. Leavitt, R. I. Scahill, R.A.C. Roos, B. Landwehmeyer, B. Borowsky, S. J. Tabrizi, X. Golay and TRACK-ON Investigators *(Submitted for Brain, Vancouver 2015).*
2. *'Chemical Exchange Saturation Transfer on a prototype model of neurodegeneration'*. E. Demetriou, A. Silva, **M. Rega**, F. Torrealdea, J. Fairney, M. Tachrount, M. Farrow, X. Golay *(Submitted for ISMRM, Toronto 2015).*
3. *'Validation of Amide Proton Transfer as a measure of pH by 31P MRS in a piglet model of HIE'*. **M. Rega**, F. Torrealdea, A. Bainbridge, D. Price, K. Broad, I. Fiernes, M. Ezzati, A. Oliver-Taylor, R. Burnett, C. Uria, N. Robertson, S. Walker-Samuel, D. Thomas, X. Golay *(Presented: ISMRM, Milan 2014 & , & CEST workshop Turin, 2014).*
4. *'Bicarbonate as a theragnostic CEST agent for glioma models'*. F. Torrealdea, **M. Rega,** J. Lau, S. Brandner, S. Walker-Samuel, D. L. Thomas, X. Golay Golay *(Presented: ISMRM, Milan 2014 & , & CEST workshop Turin, 2014).*
5. *'In-vivo Imaging of Tau Pathology using Multi-Parametric Quantitative MRI'*. JA Wells, JM O'Callaghan, HE Holmes, NM Powel, RA Johnson, S Siow, F Torrealdea, O Ismail, S Walker-Samuel, X Golay, **M Rega**, S Richardson, N Fox, AJ Schwarz, Z Ahmed, TK Murray, MJ O'Neill, EC Collins, N Colgan, MF Lythgoe. *(Presented: ISMRM, Milan 2014).*
6. *'Imaging pH changes in the piglet brain after acute hypoxia-ischemia using amide proton transfer MRI'*. **M. Rega**, F. Torrealdea, A. Bainbridge, D. Price, K. Broad, I. Fiernes, M. Ezzati, A. Oliver-Taylor, R. Burnett, C. Uria, N. Robertson, S. Walker-Samuel, D. Thomas, X. Golay *(Presented: ESMRMB, Toulouse 2013 & ESPR, Porto 2013)*
7. *'Detection of protein accumulation by amide proton transfer in the spinal cord of SOD1 mice using exchange-modulated Laser sequence (EX-L)'*. **M. Rega**, F. Torrealdea, A. Gray, J. Dick, P. Smethurst, L. Greensmith, K. Sidle, S. Walker-Samuel, D. Thomas, X. Golay *(Presented: ESMRMB, Lisbon 2012 & ISMRM, Salt lake city USA, 2013)*

8. *'GlucoCEST for the detection of human xenograft glioblastoma at early stage'*. F. Torrealdea, **M. Rega**, A. Richard-Loendt, S. Brandner, D. Thomas, S. Walker-Samuel, X. Golay *(Presented: ISMRM, Salt lake city USA, 2013).*
9. *'Investigation of CEST effects in hexoses and pentoses of the glycolytic pathway'*. F. Torrealdea, **M. Rega**, M. Lythgoe, D. Thomas, S. Walker-Samuel, X. Golay *(Presented: ISMRM, Melbourne, 2012)*
10. *'Comparison of glucoCEST enhancement with 18-F FDG autoradiography'*. S. Walker-Samuel, R. Ramasawmy, F. Torrealdea, **M. Rega**, S. P. Johnson, V. Rajkumar, M. Goncalves, D. Thomas, R. B. Pedley, M. F. Lythgoe, X. Golay *(Presented: ISMRM, Melbourne, 2012)*
11. *'Dynamic glucose- enhanced (DCE) MRI: A proof of principle study'*. S. Walker-Samuel, R. Ramasawmy, F. Torrealdea, **M. Rega**, S. P. Johnson, V. Rajkumar, D. Thomas, R. B. Pedley, M. F. Lythgoe, X. Golay *(Presented: ISMRM, Melbourne, 2012)*
12. *'Assessment of tumour glucose uptake using glucoCEST'*. S. Walker-Samuel, S. P. Johnson, F. Torrealdea, **M. Rega**, S. Richardson, R. Ramasawmy, D. Thomas, R. B. Pedley, M. F. Lythgoe, X. Golay *(Presented: ISMRM, Montreal, 2011)*